# ASSESSING FIELD-FLOW FRACTIONATION AND LIGHT SCATTERING FOR THE CHARACTERIZATION OF EXTRACELLULAR VESICLES AND POLYMER COLLOIDS

by

Christine Lynn Plavchak

A thesis submitted to the Faculty and the Board of Trustees of the Colorado School of Mines in partial fulfillment of the requirements for the degree of Doctor of Philosophy (Applied Chemistry).

Golden, Colorado

Date ______________________

Signed: ________________________

Christine L. Plavchak

Signed: ________________________

Dr. Kim R. Williams
Thesis Advisor

Golden, Colorado

Date______________________

Signed: ________________________

Dr. Tom Gennett
Professor and Head
Department of Chemistry

ABSTRACT

Nanoparticle characterization is centered around understanding how properties such as size and composition as well as count correlate with synthetic methodologies, observed behaviors, and end product performances. Current ensemble methods that examine these properties (light scattering, electron microscopy, nanoparticle tracking analysis (NTA), zeta potential, etc.) provide *average* values and cannot provide important information regarding distributions within the sample. These techniques are also compromised by sample polydispersity and may not be sensitive enough to examine particles that span the range of 1 nm to 1 µm in diameter. To overcome this, samples can be separated to create more monodisperse subpopulations, yet only a few ensemble methods have been readily coupled to separation techniques like field-flow fractionation (FFF).

FFF is a family of analytical techniques that has been used to separate and characterize macromolecules and particles since the mid-1960s. Improvements to FFF instrumentation and theory along with the coupling to multiple detectors such as light scattering, differential refractive index, spectrophotometry, and mass spectrometry has enhanced FFF's capabilities for particle characterization. More recent advancements include nanoparticle tracking analysis (NTA) and on-line Raman spectroscopy for determining the and number/size of nanoparticles as well as composition of polymeric particles, respectively. Together, they represent critical challenges and frontiers for nanoparticle analysis. The work in this thesis takes a different approach by first critically assessing multiangle light scattering (MALS) as a particle counting technique and then exploring the sensitivity of thermal field-flow fractionation (ThFFF) for compositional analyses.

The former is particularly relevant as the FFF-MALS platform is now commonly used across disciplines and products. This, in combination with particle counting component of the European Union's definition of a nanomaterial will undoubtedly lead to an increase in particle counting using MALS for particle counting. However, there has been no work published to date that critically assesses the impact of the uncertainty in nanoparticle refractive indices (a difficult to obtain value for core-shell type structures) and light scattering models used in data analysis to calculate the number of nanoparticles. This work seeks to address this gap in knowledge particularly for complex bioparticles such as outer membrane vesicles (OMVs). The thermal FFF work builds on previously published studies but differs in that the compositional sensitivity of this technique and the use of additives to improve retention and sample recovery are explored.

Asymmetrical flow FFF (AF4), coupled to multiangle light scattering (MALS), has recently gained attention for the characterization of bacterial OMVs for nanomedicine and renewable energy applications. A major analytical challenge of OMVs is understanding how particle size and count impact their biogenesis and the cargo sorting proteins in different-sized vesicles. AF4-MALS can be used as an initial separation and enumeration step prior to further analyses with techniques tandem mass spectrometry (i.e., proteomics). While MALS has been used to count biological particles and has shown similar counts to offline methods like NTA, the influence of analyte-dependent parameters (e.g., refractive index (RI) and particle shape/model) with MALS has not been examined. Polystyrene latex standards (known RI and shape) and complex OMVs (unknown RI and shape) were chosen as the model and sample systems. Particle counts from PSL differ upwards of 13 % between sphere or Lorenz-Mie models while OMV particle counts can vary up to 200% depending on the model and refractive index used. Additionally, signal-to-noise in the light scattering signal intensity can lead to erroneous particle counts (i.e., > $10^{18}$ particles/mL), which was observed when using the coated sphere model for OMVs. While a promising enumeration technique, the need of particle count standards and accurate RI values impede the determination of absolute particle counts.

Thermal FFF (ThFFF) is another technique under the FFF umbrella that can yield particle size as well as composition. The latter differentiates ThFFF from its better-known sibling, AF4. The driving force for ThFFF is imparted by a temperature gradient that is applied perpendicular to the separation axis. Analyte retention is dependent on the Soret coefficient ($S_T$), a ratio of the analytes thermal diffusion coefficient ($D_T$) to its translational diffusion coefficient ($D$). While ThFFF is mainly done in organic solvents, there is an interest in moving towards aqueous solvents (AqThFFF) in order to characterize aqueous based (biological or synthetic) materials. Two major challenges in performing AqThFFF experiments are the need to use additives (i.e., salts or surfactants) to improve analyte retention and understanding how these additives influence particle thermophoresis. Additionally, little work has been done to assess the compositional sensitivity of ThFFF. To investigate the impact of additives and compositional sensitivity, a model set of butylacrylate: methyl methacrylate: acrylic acid (BA:MMA:AA) particles with subtle differences in acidic comonomer (0-3 %) were examined. A key component of this work was examining the impact of commonly used additives such as tetrabutylammonium perchlorate (TBAP) and FL-70 detergent on analyte retention and recovery. TBAP governed retention of the colloids while the incorporation of FL-70 increased sample recovery. An incremental component of calculating $D_T$ values is utilizing accurate $D$ values. Examining $D$ values through DLS (online and offline), via AF4 theory, and transformations from radius of gyration ($R_g$) data show that flow rates as low as 0.3 mL/min during FFF separations can cause $D$ values to be larger than anticipated. While these changes in D do not impact overall trends across latex samples, they change the overall magnitude of $D_T$. AqThFFF can distinguish between 1 % of acidic comonomer between samples, based on significant differences in $D_T$ values and demonstrates a higher sensitivity than the ~9% previously reported in literature.

Overall, the work presented in this thesis provides insight into the importance of refractive index on particle counting analyses by MALS as well as subtle nuances and considerations in the data analysis for MALS particle counting. Additives that enhance retention and sample recovery in AqThFFF provide a useful foundation for future advancements and applications. This thesis serves as a platform for future work with biological particles and insight into particle thermophoresis.

TABLE OF CONTENTS

LIST OF FIGURES

LIST OF TABLES

# ACKNOWLEDGMENTS

The time I spent in graduate school has been everything yet nothing like I expected it to be. I would first like to thank the 2018 cohort of the Chemistry Department. Our bond through the highs and lows has been unique and one I will always cherish. Thank you to Dr. Kim Williams for pushing me to reach enough 'depth' on all aspects of this thesis. To my committee, Dr. Joseph Samaniuk, Dr. Wei Gao, Dr. Dylan Domaille, and Dr. Brian G. Trewyn thank you for your feedback and for your help moving things along. Additional thank you to Dr. Trewyn for caring for graduate students as the people they are and always being there.

To the past and present members of the Williams group: Dr. Carmen Bria, Dr. Billy Smith, Elizabeth Betz, Luca Baiamonte, Kaitlin Lesco and Michael Toney- thank you for paving the way, listening to me explain math concepts in group meetings, constructive discussions, support, and always being willing to try my baked goods. It is sad to see the Williams' group seminar snack reputation come to an end. Ed Dempsey, thank you for keeping our lab running and always reassuring us there is a solution to our problem. My deepest gratitude to a man that wears several important hats, Dr. Tom Gennett. I did not expect to have the relationship with the department head like I do, but I am forever grateful and appreciate your drive to constantly make sure the students are taken care of.

Thank you to my collaborators at the National Renewable Energy Laboratory:  Dr. Gregg Beckham, Dr. Davinia Salvachúa and special thanks to Dr. Allison Werner. Your explanations on the biology side of our collaboration, your support, and your interest in the analytical portion of our work is greatly appreciated. To the folks at Dow Chemical, thank you for your feedback and direction over the past few years. Drs. Nicole-Kruh Garcia and Joan M. Ryan, thank you for giving me an opportunity to apply my FFF knowledge to a different biological system.

Many special thanks to my friends, family, and de facto family all across the country for your unwavering support through this process and helping me keep my spirits high. Finally, to Glory Russell-Parks, Rylan Malarney, Yogi, and Karl: the tight knit friendship we have developed over the last five years has made this experience much more meaningful than I could have ever imagined- ‘fanks’.

To my mom, dad, Nick, Marissa, and Will

Mission Complete.

CHAPTER 1

# INTRODUCTION

## 1.1 Motivation

Advances and commercialization of nanotechnology has led to new intellectual property and great increases in revenue across the world in the last decade. As of 2018, the nanotechnology industry generated gross revenues upwards of $903 and $941 million in the US and Europe, respectively.[1] Nanomaterials have previously centered around organic and inorganic materials but the recent interest in renewable resources[2] and nanomedicines[3,4] has led to an increased focus on biological colloids (1-1000 nm). While the synthesis and use of these 3D nanomaterials (nanoparticles, nanoliposomes, etc., 1-100 nm) have dominated the nano landscape, innovation and progress in analytical methods suitable for this size scale have lagged.

Synthetically produced and naturally occurring nanoparticles often exhibit *distributions* in properties such as size, composition, and surface charge. This consequently increases the difficulty of identifying the specific components responsible for (un)desired performance and behavior; particularly since commonly used analytical techniques such as light scattering and zeta potential measure the entire sample and report only *average* values. However, when bulk techniques are coupled with a separation method, such as size exclusion chromatography (SEC) or field-flow fractionation (FFF), the properties of individual components can be measured as they elute from the column or channel. The resulting distributions provide detailed images of subpopulations within the sample, facilitates the identification of critical components, and can confirm the success of synthesis procedures. Adding to this already complex backdrop is the challenge of determining the number of particles of a specific size, composition, charge, etc. This quantitative capability represents a new analysis frontier and can yield useful insights that guide synthesis and product formulation, promotes understanding of behaviors associated with protein/lipid composition per biological particle, and infer potential biogenesis mechanisms to name a few.

### 1.2 Particle Characterization Techniques

Particle analysis techniques can generally be categorized as those that measure the entire sample (also known as ensemble methods) and generate average values and those that measure individual components and thus generate distributions. Each category of techniques is useful and appropriate in different scenarios and it is important to understand when one is preferred as well as the main benefits and limitations of each group of methods.

Ensemble methods for determining nanoparticle size, charge, and counts are and their applicable size ranges are shown in Figure 1.1. Dynamic light scattering (DLS) is used for obtaining hydrodynamic size and diffusion coefficients and surface charges are typically examined via zeta potential. While experiment times are fast in DLS, average sizes are skewed towards larger analytes within a solution.[5] Zeta potential is used to help assess potential agglomeration, sedimentation, and inter-/intraparticle interactions in colloidal systems yet the formation of coronas or complex media around particles makes determining accurate surface charges challenging.[6] Fluorescence, inductively coupled plasma mass spectrometry (ICP-MS), and flow cytometry (FC) are often used to count particles that span biological to inorganic compositions. Fluorescence and FC are not sensitive enough to measure sub-100nm particles, yet their high throughput and robustness make them widely used for bioparticle characterization.[7,8] ICP-MS overcomes this size limitation yet the matrix of biological samples can make sample preparation challenging and the lack of particle count standards prohibits accurate measurements hindering method development.[9]

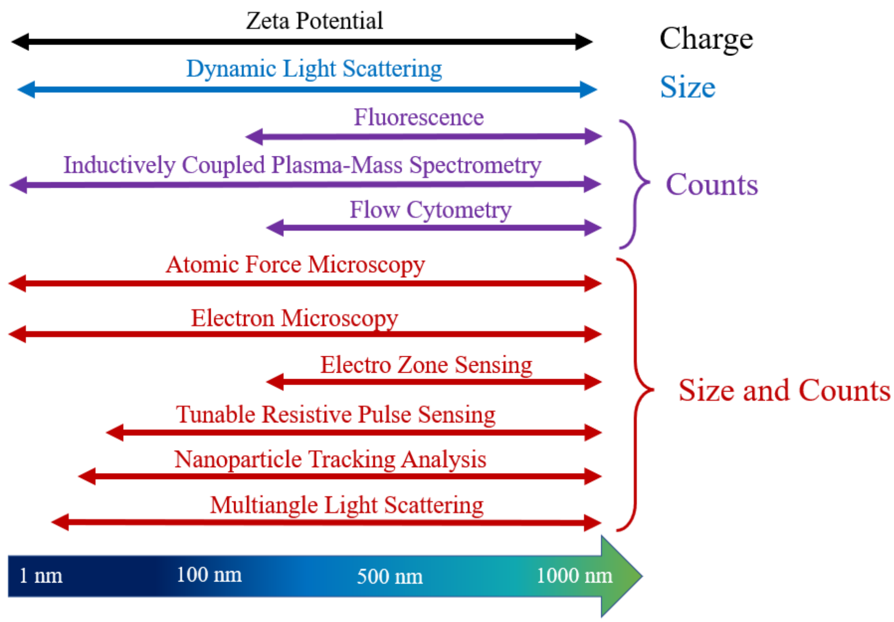


Figure 1.1 Analytical ensemble methods that are used in determining charge, size, and particle counts. Select techniques shown in red have the capabilities of providing average particle sizes and counts.

Particle sizing and counting techniques include atomic force microscopy (AFM)[10], electron microscopy (EM)[11], Coulter counter (CC) or electro zone sensing[12], tunable resistive pulse sensing (TRPS)[13], nanoparticle tracking analysis (NTA)[14], and multiangle light scattering (MALS).[15,16] The use of AFM and EM methods are highly advantageous because of their ability to visualize analytes and understand shape, size, and quantity. However, these methods often require additional sample preparation, require samples to be in a dried state, and examining large quantities of analytes is time-intensive. CC and TRPS are beneficial sizing and counting methods because of their high throughput (~1000 counts/second). Disruptions in electrical current as analytes travel through an aperture or tunable pore allows for a direct particle count to be measured. Despite this, CC instruments are not quite sensitive to examine smaller colloids (< 200 nm), require larger sample volumes (~4 mL), and multiple apertures are needed for polydisperse samples.[17] While TRPS can work with smaller sample volumes (~ 40 µL) the tunable pores often experience stretching or build-up of particles around the pores leading to tailing effects and influencing particle counts.[18,19] NTA, similar to EM and AFM, has the advantage of visually tracking particles in solution within a given field of view and requires less time than those methods to count a large number of particles. While this technique can provide distributions in size and count over an experiment, results are heavily skewed by instrumental parameters (i.e., camera level, shutter, gain, minimum track length, etc.). Polydisperse analytes often require sacrificing sample focusing to try and visualize all particles in the field of view leading to smaller analytes being missed or overshadowed by the scattered light from larger particles.[20–22] The use of MALS as a particle counting technique has gained traction over the last decade yet still remains in its juvenile stage. A main draw towards using this technique is its capability to be readily coupled to separation techniques yet knowledge of the impact of sample dependent parameters (i.e., refractive index and shape) on particle counts is poorly understood. Efforts to overcome this will be discussed in more detail in Chapter 4. Across all of the aforementioned ensemble methods, the use of these techniques is beneficial when rapid analyses are needed. While differences in sample size or polydispersity can induce bias for average measurements, these methods can be useful when the threshold or impact of these variations in analyte properties is high and have minimal impact on product performance.

The second category of nanoparticle characterization techniques usually involves a separation technique that is coupled to an ensemble technique. As separated components elute from a column or channel, their properties can be measured and the results are compiled into distributions. If coupling an ensemble technique is not possible, an initial separation step can be completed to collect monodisperse subpopulations for further offline analyses. Current separation techniques include electrophoresis (capillary[23–25] and gel[26,27]), ultracentrifugation

(UC)[28,29], hydrodynamic (HDC)[30] and size exclusion chromatography (SEC)[31], and FFF.[32] Electrophoretic methods can provide nanoparticle electrophoretic mobilities but the separation mechanism(s) and electrokinetic behavior are not well understood.[33,34] UC tends to be a time-intensive process and often induce aggregation of analytes. Despite the drawbacks of UC, it can still achieve high separation efficiency of particles based on small differences in mass and density, and remains a mainstream method for characterizing biological macromolecules and complexes.[35] HDC, SEC, and FFF are three methods that provide a size-based separation and are often compared to one another in the characterization of macromolecules. HDC and SEC separations, which occur within a packed column, are often utilized due to their ability to separate large molecular weight samples ($>10^6$ Da, HDC) or high resolution for smaller analytes $< 10^4$ Da (SEC).[36–39] The information obtained from SEC has extended beyond traditional size separations to examine other polymeric properties such as branching and fractal dimension, to colloidal core, corona and total sizes of nanoparticles using additional online detection.[40] Analytes, however, may experience undesirable interactions with the stationary phase resulting in unexpected retention times (SEC) and sample loss in both HDC and SEC. FFF methods may also suffer sample loss but in lower quantities because of the significantly reduced surface area of a channel that lacks packing material. Despite this, there are several advantages to using FFF methods for polymer and colloid characterization that will be discussed further in Chapters 2 and 3.

Considering the techniques that can provide us size, charge, counts and both size and counts along with the separation methods described above, those that can be coupled on-line with separation methods are few and far between. Currently, DLS, ICP-MS, NTA, and MALS are the only techniques that have been readily coupled to techniques like FFF and SEC. The use of online DLS provides size distributions across the sample yet more challenges arise when considering the influence of flow rate on analyte diffusion.[41] ICP-MS coupled to FFF has helped overcome detection limits and resolution with conventional concentration techniques like UV-Vis and can help examine metallic particles within biological matrices.[42] While helpful, the dilution and sample loss from the FFF separation in conjunction with larger experiment times can hinder the overall quantification of metal species.[43] NTA and MALS have recently been shown to provide particle counts when coupled to SEC or FFF and the magnitude of particle counts across these methods are often compared.[16,44–47] Thus far, the robustness of these methods and accuracy of particle counts have not been addressed. The ability to accurately enumerate particles as a function of size, composition, etc., will undoubtedly increase in importance as the European Union continues to modify their definition of a nanomaterial.[48] In addition to regulatory guidelines, the need to understand composition/particle increases will continue to grow in fields spanning nanomedicine to renewable energy applications.[49] Previous work using FFF to investigate compositional heterogeneity and particle count laid the foundation for this current work with biological and polymer colloids.[50,51]

### 1.3 Chapter Synopsis

The research described in this thesis focuses on the assessment of field flow fractionation and light scattering methods for the characterization of either biological or polymer colloids. Extensive background on general FFF, AF4 and ThFFF theory along with theory behind techniques that can be coupled to FFF techniques (NTA, MALS, and DLS) are discussed in Chapter 2. The work highlighted in Chapter 3 examines the new advances and applications within the FFF community over the past decade. Chapter 4 showcases the use of MALS as a particle counting technique and assesses the impacts of analyte-dependent parameters on overall particle counts for both standard latex particles and bacterial outer membrane vesicles (OMVs). This work led to examining how a pre-fractionation step of biological particles can impact further proteomic studies and is the first account of utilizing AF4-MALS as a separation and enumeration method of OMVs from a Gram-negative bacterium, *Pseudomonas putida*. This work also laid the groundwork for separations of vesicles from a Gram-positive bacterium, *mycobacterium tuberculosis*, which is summarized in Appendix A.[52]

The second part of this thesis (Chapter 5) examines the compositional sensitivity of ThFFF using aqueous carrier fluids. By incorporating salts and surfactants into the aqueous carrier fluid and sample preparation step, it was possible to identify small differences in particle composition (0-3 % acrylic acid) and determine particle thermal diffusion coefficients. This in conjunction with assessing the impact of accurate translational diffusion coefficients on $D_T$ has shed light on how compositionally sensitive ThFFF can be and revives aqueous ThFFF after a dormancy over the last decade. Thermal diffusion coefficient values are calculated from ThFFF retention times and translational diffusion coefficients $D$. The latter can be measured using AF4 or via batch-mode or online dynamic light scattering (DLS). Understanding the influence of fluid flow for on-line DLS measurements is applicable to work discussed in Chapter 5 and is relevant to separation methods that employ online DLS.

### 1.4 References

(1) Talebian, S.; Rodrigues, T.; Sarmento, B.; Langer, R. Facts and Figures on Materials Science and Nanotechnology Progress and Investment. *ACS Nano* **2021**, *15*, 15940–15952. https://doi.org/10.1021/acsnano.1c03992.

(2) Linger, J. G.; Vardon, D. R.; Guarnieri, M. T.; Karp, E. M.; Hunsinger, G. B.; Franden, M. A.; Johnson, C. W.; Chupka, G.; Strathmann, T. J.; Pienkos, P. T.; Beckham, G. T. Lignin Valorization through Integrated Biological Funneling and Chemical Catalysis. https://doi.org/10.1073/pnas.1410657111.

(3) Marques, M. R. C.; Choo, Q.; Ashtikar, M.; Correa, T.; Bremer-hoffmann, S.; Wacker, M. G. Nanomedicines - Tiny Particles and Big Challenges. *Adv Drug Deliv Rev* **2019**, *151–152*, 23–43. https://doi.org/10.1016/j.addr.2019.06.003.

(4) Guerrini, G.; Magrì, D.; Gioria, S.; Medaglini, D.; Calzolai, L. Characterization of Nanoparticles-Based Vaccines for COVID-19. *Nat Nanotechnol* **2022**, *17* (June), 570–576. https://doi.org/10.1038/s41565-022-01129-w.

(5) Babick, F. Dynamic Light Scattering (DLS). In *Characterization of Nanoparticles: Measurement Processes for Nanoparticles*; Elsevier, 2019; pp 137–172. https://doi.org/10.1016/B978-0-12-814182-3.00010-9.

(6) Skoglund, S.; Hedberg, J.; Yunda, E.; Godymchuk, A.; Blomberg, E.; Odnevall Wallinder, I. Difficulties and Flaws in Performing Accurate Determinations of Zeta Potentials of Metal Nanoparticles in Complex Solutions - Four Case Studies. *PLoS One* **2017**, *12* (7). https://doi.org/10.1371/journal.pone.0181735.

(7) Hedde, P. N.; Abram, T.; Vu, T.; Zhao, W.; Gratton, E. Fluorescence Lifetime Detection with Particle Counting Devices. *Biomed Opt Express* **2019**, *10* (3), 1223. https://doi.org/10.1364/boe.10.001223.

(8) Gross-rother, J.; Blech, M.; Preis, E.; Bakowsky, U.; Garidel, P. Particle Detection and Characterization for Biopharmaceutical Applications : Current Principles of Established and Alternative Techniques. **2020**.

(9) Montaño, M. D.; Olesik, J. W.; Barber, A. G.; Challis, K.; Ranville, J. F. Single Particle ICP-MS: Advances toward Routine Analysis of Nanomaterials. *Analytical and Bioanalytical Chemistry*. Springer Verlag July 1, 2016, pp 5053–5074. https://doi.org/10.1007/s00216-016-9676-8.

(10) Sebaihi, N.; De Boeck, B.; Yuana, Y.; Nieuwland, R.; Pétry, J. Dimensional Characterization of Extracellular Vesicles Using Atomic Force Microscopy. *Meas Sci Technol* **2017**, *28* (3). https://doi.org/10.1088/1361-6501/28/3/034006.

(11) Mayhew, T. M.; Mu, C.; Vanhecke, D.; Ochs, M. A Review of Recent Methods for Efficiently Quantifying Immunogold and Other Nanoparticles Using TEM Sections through Cells , Tissues and Organs. *Annals of Anatomy* **2009**, *191*, 153–170. https://doi.org/10.1016/j.aanat.2008.11.001.

(12) Graham, M. D. The Coulter Principle: Foundation of an Industry. **2003**. https://doi.org/10.1016/S1535-5535(03)00023-6.

(13) Vogel, R.; Vella, G.; Savage, J.; Law, A.; Muzard, J.; Marchioni, M.; Calzolai, L.; Camera, G. Della; Mehn, D.; Caputo, F.; Geiss, O.; Peacock, B.; Aubert, D.; Prina-mello, A. Measuring Particle Concentration of Multimodal Synthetic Reference Materials and Extracellular Vesicles with Orthogonal Techniques : Who Is up to the Challenge ? **2021**, No. May 2020. https://doi.org/10.1002/jev2.12052.

(14) Kestens, V.; Bozatzidis, V.; De Temmerman, P. J.; Ramaye, Y.; Roebben, G. Validation of a Particle Tracking Analysis Method for the Size Determination of Nano- and

Microparticles. *Journal of Nanoparticle Research* **2017**, *19* (8). https://doi.org/10.1007/s11051-017-3966-8.

(15) Hartjes, T. A.; Mytnyk, S.; Jenster, G. W.; van Steijn, V.; van Royen, M. E. Extracellular Vesicle Quantification and Characterization: Common Methods and Emerging Approaches. *Bioengineering* **2019**, *6* (1). https://doi.org/10.3390/bioengineering6010007.

(16) Sitar, S.; Kejž, A.; Pahovnik, D.; Kogej, K.; Tušek-Znidarič, M.; Lenassi, M.; Zagar, E. Size Characterization and Quantification of Exosomes by Asymmetrical-Flow Field-Flow Fractionation. *Anal Chem* **2015**, *87*, 9225–9233. https://doi.org/10.1021/acs.analchem.5b01636.

(17) Figueiredo, M. M. Electrozone Sensing in Particle Size Analysis. *Encyclopedia of Analytical Chemistry* **2006**, 1–15. https://doi.org/10.1002/9780470027318.a1504.

(18) Willmott, G. R. Tunable Resistive Pulse Sensing: Better Size and Charge Measurements for Submicrometer Colloids. **2014**. https://doi.org/10.1021/acs.analchem.7b05106.

(19) Vaclavek, T.; Prikryl, J.; Foret, F. Resistive Pulse Sensing as Particle Counting and Sizing Method in Microfluidic Systems: Designs and Applications Review. *Journal of Separation Science*. Wiley-VCH Verlag January 1, 2019, pp 445–457. https://doi.org/10.1002/jssc.201800978.

(20) Filipe, V.; Hawe, A.; Jiskoot, W. Critical Evaluation of Nanoparticle Tracking Analysis (NTA) by NanoSight for the Measurement of Nanoparticles and Protein Aggregates. *Pharm Res* **2010**, *27* (5), 796–810. https://doi.org/10.1007/s11095-010-0073-2.

(21) Hole, P. Particle Tracking Analysis (PTA). In *Characterization of Nanoparticles-Measurement Processes for Nanoparticles*; Elsevier, 2020; pp 79–96. https://doi.org/10.1016/b978-0-12-814182-3.00007-9.

(22) Gruia, F.; Parupudi, A.; Polozova, A.; Vorauer-Uhl, K.; Wagner, A.; Borth, N.; Katinger, H. Practical Considerations for Detection and Characterization of Sub-Micron Particles in Protein Solutions by Nanoparticle Tracking Analysis. *Cytometry* **2015**, *39* (3), 166–171. https://doi.org/10.1002/(SICI)1097-0320(20000201)39:2<166::AID-CYTO10>3.0.CO;2-M.

(23) Oszwaldowski, S.; Zawistowska, K.; Robers, K. P. Capillary Electrophoretic Separation of Nanoparticles. *Anal Bioanal Chem* **2011**, *399*, 2831–2842. https://doi.org/10.1007/s00216-011-4650-y.

(24) Chetwynd, A. J.; Guggenheim, E. J.; Briffa, S. M.; Thorn, J. A.; Lynch, I.; Valsami-jones, E. Current Application of Capillary Electrophoresis in Nanomaterial Characterisation and Its Potential to Characterise the Protein and Small Molecule Corona. *Nanomaterials* **2018**, *8* (99), 1–29. https://doi.org/10.3390/nano8020099.

(25) Mozhayeva, D.; Engelhard, C. Separation of Silver Nanoparticles with Different Coatings by Capillary Electrophoresis Coupled to ICP-MS in Single Particle Mode. *Anal Chem* **2017**, *89*, 9767–9774. https://doi.org/10.1021/acs.analchem.7b01626.

(26) Zheng, Y.; Hong, Y.; Wu, W.; Sun, D.; Wang, Y.; Huang, J.; Li, Q. Separation of Different Shape Biosynthesized Gold Nanoparticles via Agarose Gel Electrophoresis. *Sep Purif Technol* **2015**, *151*, 332–337. https://doi.org/10.1016/j.seppur.2015.07.045.

(27) Hanauer, M.; Pierrat, S.; Zins, I.; Lotz, A. Separation of Nanoparticles by Gel Electrophoresis According to Size and Shape. *Nano Lett* **2007**, *7* (9), 2881–2885. https://doi.org/https://doi.org/10.1021/nl071615y.

(28) Xu, X.; Colfen, H. Ultracentrifugation Techniques for the Ordering of Nanoparticles. *Nanomaterials* **2021**, *11* (333), 1–27. https://doi.org/https://doi.org/10.3390/nano11020333.

(29) Akbulut, O.; Mace, C. R.; Martinez, R. V; Kumar, A. A.; Nie, Z.; Patton, M. R.; Whitesides, G. M. Separation of Nanoparticles in Aqueous Multiphase Systems through Centrifugation. *Nano Lett* **2012**, *12* (8), 4060–4064. https://doi.org/10.1021/nl301452x.

(30) Blom, M. T.; Chmela, E.; Oosterbroek, R. E.; Tijssen, R. On-Chip Hydrodynamic Chromatography Separation and Detection of Nanoparticles and Biomolecules. *Anal Chem* **2003**, *75* (24), 6761–6768. https://doi.org/https://doi.org/10.1021/ac034663l.

(31) Peukert, W.; Kaspereit, M.; Hofe, T.; Gromotka, L. Size Exclusion Chromatography (SEC). In *Particle Separation Techiques*; Contado, C., Ed.; Elsevier, 2022; pp 409–447. https://doi.org/10.1016/B978-0-323-85486-3.00003-2.

(32) Gigault, J.; Pettibone, J. M.; Schmitt, C.; Hackley, V. A. Rational Strategy for Characterization of Nanoscale Particles by Asymmetric-Flow Field Flow Fractionation: A Tutorial. *Anal Chim Acta* **2014**, *809*, 9–24. https://doi.org/10.1016/j.aca.2013.11.021.

(33) Mozafari, M.; Nachbar, M.; Deeb, S. El. Precise Small Volume Sample Handling for Capillary Electrophoresis. *Electrophoresis* **2015**, *36*, 2665–2669. https://doi.org/10.1002/elps.201500309.

(34) Rodriguez, M. A.; Armstrong, D. W. Separation and Analysis of Colloidal / Nano-Particles Including Microorganisms by Capillary Electrophoresis : A Fundamental Review. *Journal of Chromatography B* **2004**, *800*, 7–25. https://doi.org/10.1016/j.jchromb.2003.09.060.

(35) Edwards, G. B.; Muthurajan, U. M.; Bowerman, S.; Luger, K. Analytical Ultracentrifugation (AUC): An Overview of the Application of Fluorescence and Absorbance AUC to the Study of Biological Macromolecules. *Curr Protoc Mol Biol* **2020**, *133* (1). https://doi.org/10.1002/cpmb.131.

(36) Brewer, A. K. Hydrodynamic Chromatography: The Underutilized Size-Based Separation Technique. *Chromatographia* **2021**, *84* (9), 807–811. https://doi.org/10.1007/s10337-021-04065-4.

(37) Striegel, A. M. Multi-Detector Hydrodynamic Chromatography of Colloids: Following in Hamish Small's Footsteps. *Heliyon* **2021**, *7* (4), e06691. https://doi.org/10.1016/j.heliyon.2021.e06691.

(38) Isenberg, S. L.; Brewer, A. K.; Côté, G. L.; Striegel, A. M. Hydrodynamic versus Size Exclusion Chromatography Characterization of Alternan and Comparison to Off-Line

MALS. *Biomacromolecules* **2010**, *11* (9), 2505–2511. https://doi.org/10.1021/bm100687b.

(39) Podzimek, S.; Johann, C. Asymmetric Flow Field-Flow Fractionation: Current Status, Possibilities, Analytical Limitations and Future Trends. *Chromatographia* **2021**, *84* (6), 531–534. https://doi.org/10.1007/s10337-021-04035-w.

(40) Striegel, A. M. Size-Exclusion Chromatography: A Twenty-First Century Perspective. *Chromatographia* **2022**, *85* (4), 307–313. https://doi.org/10.1007/s10337-022-04143-1.

(41) Sitar, S.; Vezoč, V.; Mač, P.; Kogej, K.; Pahovnik, D.; Agar, E. Z.ˇ. Pitfalls in Size Characterization of Soft Particles by Dynamic Light Scattering Online Coupled to Asymmetrical Flow Field-Flow Fractionation. *Anal. Chem* **2017**, *89*, 38. https://doi.org/10.1021/acs.analchem.7b03251.

(42) Nischwitz, V.; Gottselig, N.; Missong, A.; Meyn, T.; Klumpp, E. Field Flow Fractionation Online with ICP-MS as Novel Approach for the Quantification of Fine Particulate Carbon in Stream Water Samples and Soil Extracts. *J Anal At Spectrom* **2016**, *31* (9), 1858–1868. https://doi.org/10.1039/c6ja00027d.

(43) Bocca, B.; Battistini, B.; Petrucci, F. Silver and Gold Nanoparticles Characterization by SP-ICP-MS and AF4-FFF-MALS-UV-ICP-MS in Human Samples Used for Biomonitoring. *Talanta* **2020**, *220*. https://doi.org/10.1016/j.talanta.2020.121404.

(44) Steppert, P.; Burgstaller, D.; Klausberger, M.; Tover, A.; Berger, E.; Jungbauer, A. Quantification and Characterization of Virus-like Particles by Size-Exclusion Chromatography and Nanoparticle Tracking Analysis. *J Chromatogr A* **2017**, *1487*, 89–99. https://doi.org/10.1016/j.chroma.2016.12.085.

(45) Vogel, R.; Savage, J.; Muzard, J.; Camera, G. Della; Vella, G.; Law, A.; Marchioni, M.; Mehn, D.; Geiss, O.; Peacock, B.; Aubert, D.; Calzolai, L.; Caputo, F.; Prina-Mello, A. Measuring Particle Concentration of Multimodal Synthetic Reference Materials and Extracellular Vesicles with Orthogonal Techniques: Who Is up to the Challenge? *J Extracell Vesicles* **2021**, *10* (3). https://doi.org/10.1002/jev2.12052.

(46) Mildner, R.; Hak, S.; Parot, J.; Hyldbakk, A.; Borgos, S. E.; Some, D.; Johann, C.; Caputo, F. Improved Multidetector Asymmetrical-Flow Field-Flow Fractionation Method for Particle Sizing and Concentration Measurements of Lipid-Based Nanocarriers for RNA Delivery. *European Journal of Pharmaceutics and Biopharmaceutics* **2021**, *163*, 252–265. https://doi.org/10.1016/j.ejpb.2021.03.004.

(47) van der Put, R. M. F.; Spies, A.; Metz, B.; Some, D.; Scherrers, R.; Pieters, R.; Danial, M. Validation of an FFF-MALS Method to Characterize the Production and Functionalization of Outer-Membrane Vesicles for Conjugate Vaccines. *Anal Chem* **2022**, *94*, 12033–12041. https://doi.org/10.1021/acs.analchem.2c01590.

(48) European Commission. Commission Recommendation on the Definition of Nanomaterial. *Official Journal of the European Union* **2022**, 1–5. https://doi.org/10.2788/36237.

(49) Shang, J.; Gao, X. Nanoparticle Counting: Towards Accurate Determination of the Molar Concentration. *Chem Soc Rev* **2014**, *43* (21), 7267–7278. https://doi.org/10.1039/c4cs00128a.Nanoparticle.

(50) Zhang, H.; Freitas, D.; Kim, H. S.; Fabijanic, K.; Li, Z.; Chen, H.; Mark, M. T.; Molina, H.; Martin, A. B.; Bojmar, L.; Fang, J.; Rampersaud, S.; Hoshino, A.; Matei, I.; Kenific, C. M.; Nakajima, M.; Mutvei, A. P.; Sansone, P.; Buehring, W.; Wang, H.; Jimenez, J. P.; Cohen-Gould, L.; Paknejad, N.; Brendel, M.; Manova-Todorova, K.; Magalhães, A.; Ferreira, J. A.; Osório, H.; Silva, A. M.; Massey, A.; Cubillos-Ruiz, J. R.; Galletti, G.; Giannakakou, P.; Cuervo, A. M.; Blenis, J.; Schwartz, R.; Brady, M. S.; Peinado, H.; Bromberg, J.; Matsui, H.; Reis, C. A.; Lyden, D. Identification of Distinct Nanoparticles and Subsets of Extracellular Vesicles by Asymmetric Flow Field-Flow Fractionation. *Nat Cell Biol* **2018**, *20* (3), 332–343. https://doi.org/10.1038/s41556-018-0040-4.

(51) Wei, Z.; McEvoy, M.; Razinkov, V.; Polozova, A.; Li, E.; Casas-Finet, J.; Tous, G. I.; Balu, P.; Pan, A. A.; Mehta, H.; Schenerman, M. A. Biophysical Characterization of Influenza Virus Subpopulations Using Field Flow Fractionation and Multiangle Light Scattering: Correlation of Particle Counts, Size Distribution and Infectivity. *J Virol Methods* **2007**, *144* (1–2), 122–132. https://doi.org/10.1016/j.jviromet.2007.04.008.

(52) Ryan, J. M. ENRICHMENT AND SEPARATION OF MYCOBACTERIUM TUBERCULOSIS EXTRACELLULAR VESICLES WITH A SIDE OF BIOSAFETY AND BIOSECURITY, Colorado State University, Fort Collins, 2022.

# CHAPTER 2

# THEORY OF FIELD-FLOW FRACTIONATION AND COUPLED SIZING TECHNIQUES

## 2.1 Field-Flow Fractionation

### 2.1.1 Basic Theory of Retention

FFF is a chromatography-like separation method that was originally developed in 1966 by the late J. Calvin Giddings.[1] Widely used to separate macromolecules and colloids, the operating ranges of FFF span a few hundred to $10^{18}$ Da[2–5] or 1 nm to 100 µm in diameter[6–8], respectively. Unlike a packed column used in other conventional chromatography methods, FFF separations are employed in a thin, ribbon-like open channel. Across the channel thickness (*w*), which can range from 76-600 µm, a parabolic flow profile is formed along the separation axis where the highest flow velocities are towards the center of the channel and the slowest velocities are found towards the two channel walls. The respective field used in all FFF techniques is applied perpendicularly to the channels axial flow pushing analytes to the channel accumulation wall.[2] Analytes become displaced with a velocity $U$ while analyte motion towards the accumulation wall produces a field-induced flux $U_c$ (number of particles per unit cross-sectional area per unit time). To counteract this field-induced displacement, a diffusive flux proportional to the concentration gradient ($dc/dx$) which is equivalent to the analytes diffusion coefficient ($D$) is directed in the opposite direction. The net flux ($J$) due to the mass transport across the channel can be shown as:

$$J_x = U_c - D\frac{dc}{dx} \tag{2.1}$$

When the concentration gradient across the channel thickness reaches a steady state, or when the diffusive and field-induced fluxes reach equilibrium, the net flux is equal to zero.

Equation 2.1 can then be integrated assuming $U$ and $D$ remain constant giving rise to Equation 2.2 where $c_o$ is the concentration at the accumulation wall and $x$ is the distance from the wall.

$$\frac{c(x)}{c_o} = \exp\left(-\frac{|U|}{D}x\right) \tag{2.2}$$

From here it is observed that the concentration decreases exponentially from the accumulation wall, and the distribution of the analyte behaves similar to a thin sample layer positioned at a height $\ell$ or mean layered thickness. This $\ell$ term can also be defined as the ratio of thermal energy to the applied force where $\ell = kT/F$ where $k$ is the Boltzmann constant, $T$ is temperature, and $F$ is the applied force field.[7] Equation 2.2 can then be rewritten to account for $\ell$ giving Equation 2.3.

$$\frac{c(x)}{c_o} = \exp\left(-\frac{x}{\ell}\right) \tag{2.3}$$

$$\ell = \frac{D}{|U|} \tag{2.4}$$

Equation 2.4 demonstrates the dependence on analyte diffusion on opposing the effects of the field that compresses the analyte. This relationship is also related to the retention parameter in FFF equations ($\lambda$) and the channel thickness shown in Equation 2.5. This dimensionless parameter directly relates the analyte's physicochemical properties, the strength of the field, and the average location and velocity of the analyte within the parabolic flow profile.

$$\lambda = \frac{D}{|U|w} = \frac{\ell}{w} \tag{2.5}$$

Another metric for understanding retention in FFF is related to the use of the dimensionless retention ratio ($R$) which is a ratio of the mean fluid velocity ( $< v >$) and analyte migration velocity ($v_p$). This can also be described as a ratio of the void time ($t^0$), which is the amount of time it takes solvent to flow through one channel volume at a given flow rate, to the retention time ($t_r$) of an analyte, which is dependent on the analyte's interaction with the applied perpendicular field and the flow rate (Equation 2.6).

$$R = \frac{v_p}{\langle v \rangle} = \frac{t^0}{t_r} \tag{2.6}$$

To relate R and λ together, one can consider the concentration profile expressed as Eq. 2.3 and substituting in a parabolic function for the velocity ($v$), to achieve the fundamental and exact form of the retention equation for all FFF techniques:

$$R = 6\lambda\left(\coth\frac{1}{2\lambda} - 2\lambda\right) \tag{2.7}$$

Various approximations of Eq. 2.7 have been used, the most common being $R = 6\lambda$. Deviations of these approximations from the exact expression can be seen in Fig 2.1. When $\lambda < 0.02$, the linear approximation can be used to calculate R with ~ 5 % error and begins to deviate significantly thereafter. The quadratic and cubic approximations are more accurate up to $R < 0.2$ and then begin to deviate more significantly.

The work showcased in this thesis focuses on two FFF techniques, AF4 and ThFFF, that have been heavily utilized for colloidal separation and characterization. While both techniques follow the basic retention theory described above, they are sensitive to different physicochemical properties of analytes.

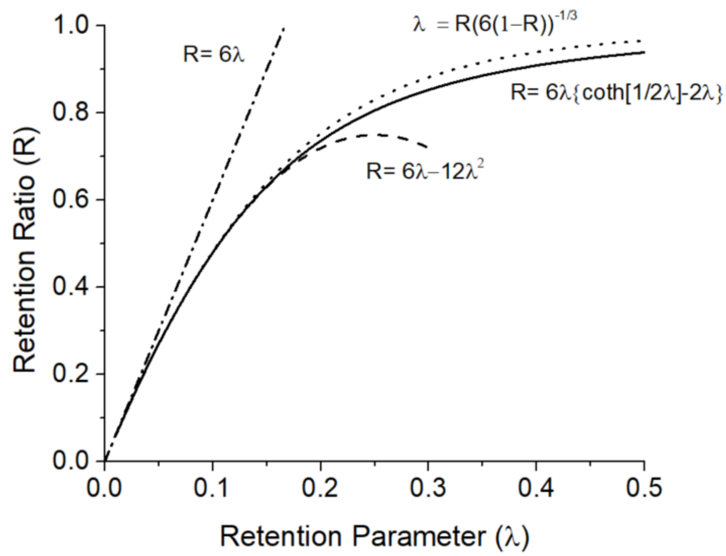


Figure 2.1 Linear, quadratic, and cubic approximations of the exact retention expression relating the retention ratio (R) to the retention parameter (λ) for all FFF techniques.

### 2.1.2 Asymmetrical Flow Field-Flow Fractionation

Asymmetrical flow field-flow fractionation or AF4 is one of the most widely used FFF techniques and solely separates particles based on their diffusion coefficient or size.[9,10] A similar technique to flow-FFF (FlFFF), AF4 was introduced in 1987 by Wahlund and Giddings where the channel design consisted of only one semi-permeable wall. Conventional FlFFF channels consisted of two permeable walls to that allows for uniform field strengths and constant flow velocities. This allowed for the general theory of FFF to be achieved. In addition to replacing the top permeable wall with a glass or polycarbonate block, changing the spacer design from rectangular to a trapezoidal channel where the outlet is tapered at one end was described by Litzén and Wahlund (Figure 2.2).[11] The changes in the channel shape improved the field velocities along the longitudinal axes, keeping them constant compared to the rectangular design.[12,13]

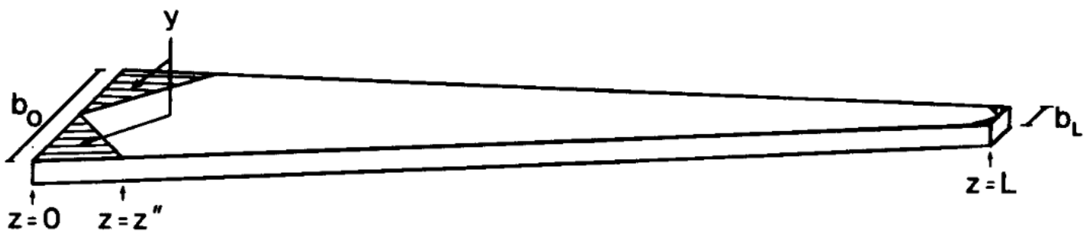


Figure 2.2 Geometry of trapezoidal channel for AF4. Reprinted from A. Litzén and K-G. Wahlund, Effects of temperature, carrier composition and sample load in asymmetrical flow field-flow fractionation. J. Chromatogra. (1991), 548, 393-406. Copyright 1991, with permission from Elsevier Science.

As described earlier, the retention ratio ($R$) is calculated from the ratio of the void time ($t^0$) and analyte retention time ($t_r$). Based on the trapezoidal design of an AF4 channel, $t^0$ is calculated using Eq. 2.8 where $V_o$ is the void volume, $V_c$ is the crossflow rate, $V_{out}$ is the channel outlet flow rate, $z'$ is the distance from the inlet to the focusing point, $L$ is the length of the channel, $b_L$ and $b_o$ are breadths of the channel of the inlet and outlet, $w$ is the channel thickness, and $y$ is the area cut off from the tapered inlet.

$$t_o = \left[\frac{V_o}{V_c}\right] * ln\left\{1 + \frac{V_c}{V_{out}}\left(1 - \left[\frac{w\left[b_o z' - \left(\frac{b_o - b_L}{2L}\right) * z'^2 - y\right]}{V_o}\right]\right)\right\} \tag{2.8}$$

To relate $R$ values to the retention parameter λ, again the approximation $R = 6\lambda$ may be used at high retention levels (R< 0.02) but it is suggested to use the exact form shown in Eq. 2.7. When using isocratic fields throughout an AF4 experiment, one can calculate the analytes diffusion coefficient using the determined λ value through

$$D = \frac{\lambda V_c w^2}{V_o} \tag{2.9}$$

If the overall experimental conditions and analyte diffusion coefficient are known, $t_r$ values may also be predicted using Eq. 2.10. Based on the diffusion coefficient of the analyte, a hydrodynamic radius may be determined through the use of Stokes-Einstein equation. (Eq. 2.11) where $k_B$ is Boltzmann's constant, $T$ is temperature, and $\eta$ is the viscosity of the suspending medium.

$$t_r = \frac{t^0 V_c w^2}{6 D V_o} \tag{2.10}$$

$$D = \frac{k_B T}{6 \pi \eta R_h} \tag{2.11}$$

Quite often the use of isocratic crossflow rates leads to band broadening and analyte polydispersity can cause increased experiment times.[14] To mitigate this, crossflow programming, where one has a gradient elution profile (linear or exponential) may be used.[15,16] This allows for higher flow rates to be used to retain smaller analytes and then decays to slower crossflow rates are used to increase the rate of elution of larger particles improving resolution. A drawback to field programming is the inability to utilize Eq. 2.10 to predict retention times from AF4 theory. A way to overcome this is to use a mixture of particle, polymer, or protein standards of different sizes or molecular weights to determine estimated retention times and resolution.

### 2.1.3 Thermal Field-Flow Fractionation

Unlike the standard set-up of FlFFF and AF4 systems, ThFFF channels are typically formed by clamping an FFF channel (made from either a polyimide or Mylar sheet) between two copper blocks. The copper blocks contain highly polished nickel, chromium, or nickel-chromium alloy surfaces.[2,17] The thermal gradient applied to the channel is formed from electrical heating rods that are placed within the top copper block. These heating elements may be placed longitudinally or horizontally across to establish a consistent thermal gradient ($\Delta T$ = 20-100 K) while cold water is flowed through the bottom block using a recirculating chiller, maintaining a constant cold wall temperature. A consistent and low cold wall temperature is important for using larger field strengths or when thermal diffusion coefficients need to be determined. Changes in the cold wall temperature have also been shown to shift retention of analytes to a lower retention time due to changes in fluid viscosity thus ultimately impact $D_T$ calculations.

Analyte retention in ThFFF is dominated by the Soret coefficient ($S_T$) which is a ratio of an analytes thermal diffusion ($D_T$) to its translational diffusion ($D$) giving the relationship $S_T = {D_T}/{D}$.[18,19] This ratio gives rise to not only a size-based separation, but also provides insight into particle-solvent interactions and thus has a compositional sensitivity (analytes $D_T$).[20–22] While the relationship of FFF elution and analyte $D$ is well understood, particle thermal diffusion continues to be poorly understood. The retention parameter (λ) in ThFFF assumes a linear temperature gradient across the thickness of the channel giving rise to Equation 2.12.

$$\lambda = \frac{1}{S_T \Delta T} = \frac{D}{D_T \Delta T} \tag{2.12}$$

A correction to the exact retention ratio equation ($R$) for ThFFF is also needed due to the distortion of the parabolic flow profile due to the temperature gradient (2.13).[23,24] This correction ($v$) is related to the physical properties of the solvent such as thermal conductivity, thermal expansion, temperature-viscosity relationship, etc. While values for $v$ of different solvents can be found in literature[25] , solvents with an unknown $v$ value can be estimated and compared to existing nonparabolicity data to a solvent's Andrade scaling factor ($B$).[17] This scaling factor can be solved through knowledge of the solvent viscosity and temperature at the cold wall, ($\eta(T)$) and $T_c$ respectively (Eq. 2.14).

$$\lambda = 6\lambda\big(\nu + (1 - 6\lambda)\big)\left[\coth\frac{1}{2\lambda} - 2\lambda\right] \tag{2.13}$$

$$\eta(T) = \eta_n e^{\left[B\left(\frac{1}{T}-\frac{1}{T_c}\right)\right]} \tag{2.14}$$

While efforts have been made to improve the solvent selection for polymers in ThFFF analysis through predictive models, solvent selection for particle analysis remains a trial-and-error process.[26] In addition to solvent selection, there still lacks a unified particle thermophoresis theory which makes understanding overall trends in particle thermal diffusion unclear.[27–32] These trends could also be due to changes in particle size (swelling/shrinking behavior) and or be solvent-dependent.[33,34] In the case of particle retention in both organic and aqueous ThFFF, the use of additives has also shown to greatly impact retention albeit mechanisms as to why additives contribute to particle retention are also poorly understood.[35–38]

## 2.2 Sizing and Counting Techniques Coupled to FFF

### 2.2.1 Nanoparticle Tracking Analysis

Nanoparticle tracking analysis (NTA) or particle tracking analysis (PTA) is an optical technique that is used to determine size and count distributions of spherical particles ranging. The current operating range for NTA spans particles 10-1000 nm in diameter and is often instrument and sample dependent.[39] Scattered light from particles within the illumination path are monitored through a CCD or CMOS camera. The Brownian motion of individual particles in solution leads to determination of a diffusion coefficient ($D$) of each particle which can then be related to a hydrodynamic diameter ($d_h$). As video of particle motions are recorded, algorithms are then used to track particles from different frames of the video. The square of the distance a particle travels between adjacent frames of the video over all frames is averaged ($\overline{(x,y)^2}$) and considering the time period between the start of each frame ($t$), the diffusion coefficient of a particle can be determined by Eq. 2.15. To determine the hydrodynamic diameter of the particle measured by NTA, the Stokes Einstein equation can then be derived as Eq. 2.16. Rearrangement of Eq. 2.16 will provide the hydrodynamic diameter.[39,40] To obtain particle count or concentration, the volume that can be observed with the microscope can be used to divide the total number of particles by the volume within the field of view. It is important to note that while spherical particles are scattering light from the laser source, the tracking of particles and thus size determination is taken from the center of a particle.

$$D = \frac{\overline{(x,y)^2}}{4t} \tag{2.15}$$

$$\overline{(x,y)^2} = \frac{4Tk_B t}{3\pi\eta d} \tag{2.16}$$

In contrast to other optical methods like dynamic light scattering (DLS), NTA provides better resolution for size and allows for the operator to visibly see particles moving though the field of view. On top of being a more visual technique, being able to examine analyte fluorescence and zeta potential showcases highlights some of the other benefits of utilizing NTA. Additional benefits include low experiment time, it is a nondestructive technique, and the only sample preparation needed is sample dilution.

While NTA is currently a mainstream method to determine particle size and count, several drawbacks still remain with this technique. One of the major disadvantages of NTA is that results are largely influenced by operator parameters. Setting camera levels (shutter, gain, etc), sample focusing, minimum track length (MTL), sample concentration can all influence the sizes and counts measured. The ideal number of particles per frame is estimated to be ~30-100 particles per frame where a relatively narrow concentration range of 1-2 orders of magnitude is needed.[41–44] Efforts have been made to improve the accuracy of particle size distributions through simulations and adaptations to mathematical algorithms, yet some require additional data analysis from the instrument operator.[45–47] Polydispersity of samples for NTA analysis can often contribute to erroneous scattering of particles impacting the tracking of the particles in solution. Another issue with polydisperse samples resides in the inability to accurately focus small and larger particles in solution. Focusing the camera on larger particles may cause smaller particles to be out of the camera field of view and impacting whether or not the smaller population is tracked within the experiment.

To mitigate some of these drawbacks, works have examined size distributions determined from FFF- or SEC- DLS and compared those to NTA distributions while others performed initial separations via FFF and SEC, collected fractions, and then performed offline NTA. [48–50] The latter helps mitigate the size polydispersity bias in NTA yet is more time-intensive. Coupling NTA to a separation technique like FFF is ideal and has only recently come to fruition. One successful account of coupling NTA to FFF incorporated both developing NTA settings to account for the changes in camera levels needed to look at particles ranging from 50-200 nm ($d_h$) while incorporating a split flow set-up to accommodate the smaller volumes needed for NTA analysis.[51] Future work with FFF-NTA could lead to future implementation of the technique within FFF commercial systems and allow for a more robust comparison of particle counting using NTA and MALS.

### 2.2.2 Multiangle Light Scattering

The theory of multiangle light scattering (MALS) stems from the fundamental equations defined by James Maxwell in 1865 where he described light and how it interacts with matter.[52] In 1871 John William Strutt (Lord Rayleigh) later simplified Maxwell's equations for the case of particles with a radius less than 1/10$^{th}$ the wavelength of the radiation. Extensions of Rayleigh scattering to understand the scattering of light for larger macromolecules has led to the Rayleigh-

Gans-Debye (RGD) approximation.[53–57] To account for all ratios of particle radius to wavelength, Gustav Mie developed the mathematical theory to understand the scattering of electromagnetic waves for spherical particles in 1908.[58] In contrast to the RGD approximation, Mie theory relies on the exact solutions to Maxwell's equations for a spherical particle interacting with polarized light. It is important to know the differences between the two theories and more detail behind the theories can be found the works of Kerker and van de Hulst.[59,60]

MALS is predominantly used for determining molecular weight ($M_w$) and radius of gyration ($R_g$) for macromolecules yet has expanded into providing particle counts and protein conjugate analyses of complex nanoparticles. The typical set-up of a MALS instrument consists of a flow cell surrounded by 3 or 18 photodiodes at preset angles, with the total volume viewed by the detectors is ~ 0.02 µL. The mathematical relationship between the amount of light scattered from an analyte to the determination of its $M_w$ and $R_g$ is dependent on whether the analyte solution is in a dilute (0.1-1.0 mg/mL) or semi-dilute (> 1 mg/mL) regime. It should be noted that these concentrations are sample and solution dependent in case there are long-range interactions with polyelectrolytes in solutions. Within a dilute regime, distances between particles or macromolecules are large enough that some intermolecular interactions can be ignored. The relationship with molar mass, concentration, and light intensity in a dilute regime is seen in Eq. 2.17 where $R_\theta$is the excess Rayleigh ratio, $M$ is the weight average molar mass, $c$ is the mass concentration of the solution, and $P(\theta)$ is a form factor which provides some information on the analytes size, shape, and structure. $K^*$ contains various components of the system that includes the refractive index of the solvent ($n_o$), the change in solute refractive index with respect to concentration ($^{dn}/_{dc}$), and the wavelength of light in vacuum ($\lambda_o$). [61]

$$I(\theta)_{scattered} \propto \frac{R_\theta}{K^*} = McP(\theta) \tag{2.17}$$

$$K^* = \frac{4\pi^2 n_0^2 \left({dn}/{dc}\right)^2}{\lambda_o^4 N_A} \tag{2.18}$$

When analytes are used in higher concentrations, intermolecular interactions begin to have an effect on the light scattering intensity. Again, while sample and solvent dependent, Eq. 2.17 is modified to account for a first-order virial expansion so that one obtains Eq. 2.19. $A_2$ is termed the second virial coefficient and is used to help correct for intermolecular interactions which is due to coherent intermolecular scattering.

$$\frac{K^* c}{R_\theta} = \frac{1}{MP(\theta)} + 2A_2 c \tag{2.19}$$

In addition to the solute concentration, the size of the analyte leads to changes in scattering intensity. For analytes that are much smaller than the incident light, (~10 nm = diameter), the intensity of scattered light off of these analytes scatters isotropically, meaning there is no angular dependence. For larger macromolecules, light will scatter differently from various parts of the analyte (light scattering more in forward direction) causing the scattered light to be in different phases as it reaches a detector. This ultimately causes destructive or constructive interference.

The measurement of $M_w$ and $R_g$ relies on different formalisms that are adaptations of Eq. 2.19 and depend on analyte properties (Table 2.1). The three main formalisms are the Zimm, Berry, and Debye and if the absolute shape is known for the analyte of interest, there are different shape-dependent models that use an analytical expression for the form factor or

$P(\theta)$.[61–63] A seminal paper that describes the error with these models is highly valued and recommended to appropriately determine the formalism and polynomial fit.

For sphere-like structures, the use of the shape-dependent models has become widely used and as more nanoparticles with complex shapes are synthesized, it is important to understand how light scattering and the use of $P(\theta)$ impacts MALS measurements. Within the past decade, the field has begun to assess how to modify current $P(\theta)$ equations and also account for aggregates of two to five homogeneous sphere.[63] This ultimately impacts the use of MALS for those more advanced characterization methodologies mentioned earlier. In case of using MALS as a particle counting technique, there is extensive theory that will be explained in Chapter 4.

Table 2.1 Different MALS formalisms for determining $M_w$ and $R_g$ adapted from Wyatt Technology Corporation

| Formalism | Y-axis | Radius Ranges | Notes |
|---|---|---|---|
| Zimm | $\frac{K^*c}{R(\theta)}$ | < 50 nm | Most linear formalism |
| Berry | $\sqrt{\frac{K^*c}{R(\theta)}}$ | > 50 nm | Random coils or elongated conformation |
| Debye | $\frac{R(\theta)}{K^*c}$ | Wide size range | Compact/sphere-like conformations |
| Shape-dependent | $\frac{R(\theta)}{K^*c}$ | Wide size range | Analytical expression for $P(\theta)$ based on random coil, sphere, coated sphere, or rod |

### 2.2.3 Dynamic Light Scattering

DLS, otherwise known as photon correlation spectroscopy (PCS) or quasi-elastic light scattering (QELS), is a commonly used technique for measuring the Brownian motion of nanoparticles and other macromolecules in solution. Having an operating range of 0.3 nm to 10 µm in diameter, this technique is often used to obtain average diffusion information and thus an average hydrodynamic size of the analyte. While it has a wide operating range, it has low resolution that often needs particles to differ in size by at least a factor of three to be resolved and the average size is often skewed towards the larger size population.[64] Knowledge of the solvent viscosity and temperature are essential in measurements as viscosity is related to temperature and elevated temperatures can impact the Brownian motion of particles. Smaller particles move or diffuse faster than larger particles as the collision with the solvent molecules are the same, yet larger particles encounter a larger retarding force or friction from the surrounding solvent molecules (Eq. 2.20) where $\eta$ is the solvent viscosity and $R_h$ is the hydrodynamic radius of the particle.

$$F_{friction} = 6\pi\eta R_h \tag{2.20}$$

As particles move through the solution during an experiment, light is scattered from the particles in all directions, and light intensity fluctuations are measured over small timeframes at one detector. These light intensity fluctuations are due to the changes in constructive and destructive interference of the scattered light from the particles.[65–67] In order to determine a diffusion coefficient for an analyte, the light fluctuations are used to calculate an autocorrelation function or second-order correlation function ($G_2(\tau)$) where $\tau$ is the lag time between two time-points. This intensity correlation function can be expressed as an integral over a time, $t$, and delayed time $(t + \tau)$ giving rise to Eq. 2.21. This equation can then be normalized giving rise to Eq. 2.22. The brackets across both equations represent the averaging of properties over the duration of the experiment time $(t)$.

$$G_2(\tau) = \langle I(t)I(t+\tau)\rangle \tag{2.21}$$

$$g_2(\tau) = \frac{\langle I(t)I(t+\tau)\rangle}{\langle I(t)\rangle^2} \tag{2.22}$$

While $(G_2(\tau))$ provides information regarding the intensity fluctuation of the macromolecule in solution, it is not possible to know exactly where each particle is within the solution. Thus, the motion of particles relative to each other is correlated to the first-order correlation function $G_1(\tau))$ otherwise known as the electric field correlation function. Similar to Eq. 2.22**,** this correlation function may also be normalized where $E(t)$ and $E(t+\tau)$ represent scattered electric fields at time and delayed time (Eq. 2.23)**.**

$$g_1(\tau)) = \frac{\langle E(t)E(t+\tau)\rangle}{\langle E(t)\rangle^2} \tag{2.23}$$

The two normalized equations may be coupled to one another based on the approximations that the detector only detects scattered light and that the photon counting is a random but Gaussian process. This relationship is seen with Eq. 2.24 where $B$ is the baseline and $\beta$ is a coherence factor that depends on properties of the detector (i.e. detector area, optical alignment, etc.).

$$g_2(\tau) = B + \beta|g_1(\tau)|^2 \tag{2.24}$$

There are important considerations for both monodisperse and polydisperse analytes, but in both scenarios $g_1(\tau))$ decays exponentially. For the former, the exponential decay is dependent on a decay constant ($\Gamma$) (Eqs. 2.25 and 2.26).

$$g_1(\tau)) = e^{-\Gamma\tau} \tag{2.25}$$

$$g_2(\tau) = 1 + \beta e^{-2\Gamma\tau} \tag{2.26}$$

The latter requires an intensity-weighted integral over a distribution of decay rates $G(\Gamma)$ (Eq. 2.27). The use of the delay constant is related to the diffusion of the analytes of interest through the expression $\Gamma = Dq^2$. The use of $q$ incorporates the solvent refractive index ($n_o$) and is inversely proportional to the wavelength of the laser ($\lambda$) and $\theta$,which is the detector angle (Eq. 2.28).

$$g_1(\tau) = \int_0^{\infty} G(\Gamma)\, e^{-\Gamma_\tau \mathrm{d}\Gamma} \tag{2.27}$$

$$q = \frac{4\pi n_o}{\lambda} \sin \left({}^{\theta}/_{2}\right) \tag{2.28}$$

With these considerations, Eq. 2.26 may be rewritten by replacing Γ with the full equation giving Eq. 2.29 which correlates particle motion to measured fluctuations.

$$g_2(\tau) = 1 + \beta e^{-2Dq^2\tau} \tag{2.29}$$

Upon determining the diffusion of the analyte, the Stokes-Einstein relationship may be used to determine the hydrodynamic radius of the analyte (Eq. 2.30) where $k_B$ is Boltzmann's constant, $T$ is temperature, and the components of the denominator are similar to those described in Eq. 2.20.

$$D = \frac{k_B T}{6\pi\eta R_h} \tag{2.30}$$

There are two types of fitting functions for autocorrelation functions within a DLS experiment: cumulants and regularization.[65,68] Cumulants assumes a monodisperse population of particles and uses a slightly modified version of Eq. 2.29 that accounts for at least three different cumulants: the mean decay rate, width of the size distribution or polydispersity, and asymmetry of the distribution. Regularization assumes a polydisperse analyte where each population of particles is fit to determine its own polydispersity. Should a polydisperse analyte not have differences in size of at least three-fold, the multimodal sample will appear to have a large polydispersity index than a purely monomodal or monodisperse sample.

In addition to the determination of diffusion coefficients and hydrodynamic radius, DLS can be used to determine the diffusion interaction parameter ($k_D$). This metric is used to understand the change of $D$ with respect to analyte concentration through the relationship shown in Eq. 2.31 where $D$ is the measured diffusion coefficient, $D_0$ is the y-intercept of the $D$ vs concentration plot, and $c$ is the concentration of the particles in mg/mL.[69–71] A positive $k_D$ corresponds to a repulsive interaction of molecules in solution where $D$ increases and thus particle size decreases. In contrast, and negative $k_D$ is linked to an attraction of molecules in solution resulting in a lower $D$ and larger $R_h$.

$$D = D_0(1 + k_D c) \tag{2.31}$$

The use of DLS online with FFF and SEC instrumentation overcomes many of the drawbacks of DLS in 'batch' mode. While advantageous to use online DLS to examine sizes of recently fractionated samples, the FFF or SEC flow rates may also contribute to changes in particle diffusion. Flow rates as low as 0.2 mL/min can cause a decrease in measured particle size and the extent of the deviation from the anticipated size amplifies as particle size increases when using a flow-through cell.[66,72] There have been recent instrumental developments to increase the bore size of the flow cell (from 1.2 mm to 3.0 mm) yet most commercial systems are with the sold conventional flow cell. This will be highlighted more in Chapter 5 with how using online $D$ values can impact calculations for particle thermal diffusion ($D_T$).

## 2.3 References


(1) Giddings, J. C. A New Separation Concept Based on a Coupling of Concentration and Flow Nonuniformities. *Separation Science* **1966**, *1* (1), 123–125. https://doi.org/10.1080/01496396608049439.

(2) Schimpf, M. E.; Caldwell, Karin, D.; Giddings, J. C. *Field Flow Fractionation Handbook*, 1st ed.; John Wiley & Sons, Ltd: New York, NY, 2000.

(3) Janča, J. *Field-Flow Fractionation: Analysis of Macromolecules and Particles*; Marcel Dekker: New York, 1988.

(4) Kassalainen, G. E.; Williams, S. K. R. Lowering the Molecular Mass Limit of Thermal Field-Flow Fractionation for Polymer Separations. *J Chromatogr A* **2003**. https://doi.org/10.1016/S0021-9673(02)02061-7.

(5) Ratanathanawongs Williams, S. K.; Lee, D. Field-Flow Fractionation of Proteins Polysaccharides, Synthetic Polymers, and Supramolecular Assemblies. *J Sep Sci* **2006**, *29* (12), 1720–1732. https://doi.org/10.1002/jssc.200600151.

(6) Giddings, J. C.; Caldwell, K. D. Field-Flow Fractionation. In *Physical methods of Chemistry*; Rossiter, B. W., Hamilton, J. F., Eds.; John Wiley: New York, 1989; Vol. 3B.

(7) Giddings, J. C. Field-Flow Fractionation: Analysis of Macromolecular, Colloidal, and Particulate Materials. *Science (1979)* **1993**, *260*, 1456–1465.

(8) Beckett, R.; Hart, B. T. Use of Field-Flow Fractionation Techniques to Characterize Aquatic Particles, Colloids and Macromolecules. In *Environmental Particles*; Buffle, J., Van Leeuwen, H. P., Eds.; CRC Press: Boca Raton, 1993; Vol. 2, pp 157–195.

(9) Contado, C. Field Flow Fractionation Techniques to Explore the "Nano-World." *Anal Bioanal Chem* **2017**, *409*, 2501–2518. https://doi.org/10.1007/s00216-017-0180-6.

(10) Yohannes, G.; Jussila, M.; Hartonen, K.; Riekkola, M. L. Asymmetrical Flow Field-Flow Fractionation Technique for Separation and Characterization of Biopolymers and Bioparticles. *J Chromatogr A* **2011**, *1218*, 4104–4116. https://doi.org/10.1016/j.chroma.2010.12.110.

(11) Litzén, A.; Wahlund, K. G. Effects of Temperature, Carrier Composition and Sample Load in Asymmetrical Flow Field-Flow Fractionation. *J Chromatogr A* **1991**. https://doi.org/10.1016/S0021-9673(01)88622-2.

(12) Ahn, J. Y.; Kim, K. H.; Lee, J. Y.; Williams, P. S.; Moon, M. H. Effect of Asymmetrical Flow Field-Flow Fractionation Channel Geometry on Separation Efficiency. *J Chromatogr A* **2010**, *1217* (24), 3876–3880. https://doi.org/10.1016/j.chroma.2010.04.021.

(13) Williams, P. S. Design of an Asymmetrical Flow Field-Flow Fractionation Channel for Uniform Channel Flow Velocity. *Journal of Microcolumn Separations* **1997**, *9* (6), 459–467.

(14) Kirkland, J. J.; Dilks, C. H.; Rementer, S. W.; Yau, W. W. Asymmetric-Channel Flow Field-Flow Fractionation with Exponential Force-Field Programming. *J Chromatogr A* **1992**, *593* (1–2), 339–355. https://doi.org/10.1016/0021-9673(92)80303-C.

(15) Williams, P. S. Fractionating Power and Outlet Stream Polydispersity in Asymmetrical Flow Field-Flow Fractionation. Part I: Isocratic Operation. *Anal Bioanal Chem* **2016**, *408*, 3247–3263. https://doi.org/10.1007/s00216-016-9388-0.

(16) Williams, P. S. Fractionating Power and Outlet Stream Polydispersity in Asymmetrical Flow Field-Flow Fractionation. Part II: Programmed Operation. *Anal Bioanal Chem* **2017**, *409*, 317–334. https://doi.org/10.1007/s00216-016-0007-x.

(17) Imran Malik, M.; Mays, J.; Raza Shah, M. *Molecular Characterization of Polymers: A Fundamental Guide*; 2021.

(18) Myers, M. N.; Caldwell, K. D.; Calvin Giddings, J. A Study of Retention in Thermal Field-Flow Fractionation. *Separation Science* **1974**, *9* (1), 47–70. https://doi.org/10.1080/01496397408080043.

(19) Smith, L. R. K.; Myers, M. N.; Giddings, J. C. Peak Broadening Factors in Thermal Field-Flow Fractionation. *Anal Chem* **1977**, *49* (12), 1750–1756. https://doi.org/10.1021/ac50020a030.

(20) Gunderson, J. J.; Giddings, J. C. Chemical Composition and Molecular-Size Factors in Polymer Analysis by Thermal Field-Flow Fractionation and Size Exclusion Chromatography. *Macromolecules* **1986**, *19* (10), 2618–2621. https://doi.org/10.1021/ma00164a027.

(21) Schimpf, M. E.; Giddings, J. C. Characterization of Thermal Diffusion in Polymer Solutions by Thermal Field-flow Fractionation: Dependence on Polymer and Solvent Parameters. *J Polym Sci B Polym Phys* **1989**, *27* (6), 1317–1332. https://doi.org/10.1002/polb.1989.090270610.

(22) Shiundu, P. M.; Calvin Giddings, J. Influence of Bulk and Surface Composition on the Retention of Colloidal Particles in Thermal Field-Flow Fractionation. *J Chromatogr A* **1995**. https://doi.org/10.1016/0021-9673(95)00572-5.

(23) Belgaied, J. E.; Hoyos, M.; Martin, M. Velocity Profiles in Thermal Field-Flow Fractionation. *J Chromatogr A* **1994**, *678*, 85–96.

(24) Martin, M.; Van Batten, C.; Hoyos, M. Determination of Thermodiffusion Parameters from Thermal Field-Flow Fractionation Retention Data. In *Thermal nonequilibrium phenomena in fluid mixtures*; 2002; pp 250–284.

(25) Geisler, M.; Lederer, A. Non-Parabolicity Correction for Fifty-Nine Solvents and a Retention Study for Strongly Distorted Flow-Profiles in Thermal Field-Flow Fractionation. *J Chromatogr A* **2020**, *1621*. https://doi.org/10.1016/j.chroma.2020.461082.

(26) Geisler, M.; Plü, L.; Merna, J.; Lederer, A. The Role of Solubility in Thermal Field-Flow Fractionation: A Revisited Theoretical Approach for Tuning the Separation of Chain Walking Polymerized Polyethylene. **2020**. https://doi.org/10.1021/acs.analchem.0c03686.

(27) Anderson, J. L. *Colloid Transport by Interfacial Forces*; 1989; Vol. 21. www.annualreviews.org.

(28) Giddings, J. C.; Shinudu, P. M.; Semenov, S. N. Thermophoresis of Metal Particles in a Liquid. *J Colloid Interface Sci* **1995**, *176* (2), 454–458. https://doi.org/10.1006/jcis.1995.9946.

(29) Morozov, K. I. Thermal Diffusion in Disperse Systems. *Journal of Experimental and Theoretical Physis* **1999**, *88* (5), 944–946.

(30) Bringuier, E.; Bourdon, A. Colloid Transport in Nonuniform Temperature. *Phys Rev E Stat Phys Plasmas Fluids Relat Interdiscip Topics* **2003**, *67* (1), 6. https://doi.org/10.1103/PhysRevE.67.011404.

(31) Duhr, S.; Braun, D. Why Molecules Move along a Temperature Gradient. *Proceedings of the National Academy of Sciences* **2006**, *103* (52), 19678–19682. https://doi.org/10.1073/pnas.0603873103.

(32) Piazza, R. Thermophoresis: Moving Particles with Thermal Gradients. *Soft Matter* **2008**, *4* (9), 1740–1744. https://doi.org/10.1039/b805888c.

(33) Kim Ratanathanawongs, S.; Shiundu, P. M.; Calvin Giddings, J. Size and Compositional Studies of Core-Shell Latexes Using Flow and Thermal Field-Flow Fractionation. *Colloids Surf A Physicochem Eng Asp* **1995**, *105* (2–3), 243–250. https://doi.org/10.1016/0927-7757(95)03315-7.

(34) Mes, E. P. C.; Tijssen, R.; Kok, W. T. Influence of the Carrier Composition on Thermal Field-Flow Fractionation for the Characterisation of Sub-Micron Polystyrene Latex Particles. *J Chromatogr A* **2001**. https://doi.org/10.1016/S0021-9673(00)01010-4.

(35) Jeon, S. J.; Schimpf, M. E.; Nyborg, A. Compositional Effects in the Retention of Colloids by Thermal Field-Flow Fractionation. *Anal Chem* **1997**, *69* (17), 3442–3450. https://doi.org/10.1021/ac9613040.

(36) Mes, E. P. C.; Kok, W. T.; Tijssen, R. Sub-Micron Particle Analysis by Thermal Field-Flow Fractionation and Multi-Angle Light Scattering Detection. *Chromatographia* **2001**, *53* (11–12), 697–703. https://doi.org/10.1007/BF02493023.

(37) Liu, G.; Giddings, J. C. Separation of Particles in Aqueous Suspensions by Thermal Field-Flow Fractionation. Measurement of Thermal Diffusion Coefficients. *Chromatographia* **1992**, *34* (9–10), 483–492. https://doi.org/10.1007/BF02290241.

(38) Shiundu, P. M.; Liu, G.; Calvin Giddings, J. Separation of Particles in Nonaqueous Suspensions by Thermal Field-Flow Fractionation. *Anal Chem* **1995**, *67* (15), 2705–2713. https://doi.org/10.1021/ac00111a032.

(39) Hole, P. Particle Tracking Analysis (PTA). In *Characterization of Nanoparticles-Measurement Processes for Nanoparticles*; Elsevier, 2020; pp 79–96. https://doi.org/10.1016/b978-0-12-814182-3.00007-9.

(40) Maguire, C. M.; Rösslein, M.; Wick, P.; Prina-Mello, A. Characterisation of Particles in Solution–a Perspective on Light Scattering and Comparative Technologies. *Sci Technol Adv Mater* **2018**, *19* (1), 732–745. https://doi.org/10.1080/14686996.2018.1517587.

(41) Gardiner, C.; Ferreira, Y. J.; Dragovic, R. A.; Redman, C. W. G.; Sargent, I. L. Extracellular Vesicle Sizing and Enumeration by Nanoparticle Tracking Analysis. *J Extracell Vesicles* **2013**, *2* (1). https://doi.org/10.3402/jev.v2i0.19671.

(42) Gardiner, C.; Shaw, M.; Hole, P.; Smith, J.; Tannetta, D.; Redman, C. W.; Sargent, I. L. Measurement of Refractive Index by Nanoparticle Tracking Analysis Reveals Heterogeneity in Extracellular Vesicles. *J Extracell Vesicles* **2014**, *3* (25361), 1–6. https://doi.org/10.3402/jev.v3.25361.

(43) van der Pol, E.; Coumans, F. A. W.; Grootemaat, A. E.; Gardiner, C.; Sargent, I. L.; Harrison, P.; Sturk, A.; van Leeuwen, T. G.; Nieuwland, R. Particle Size Distribution of Exosomes and Microvesicles Determined by Transmission Electron Microscopy, Flow Cytometry, Nanoparticle Tracking Analysis, and Resistive Pulse Sensing. *Journal of Thrombosis and Haemostasis* **2014**, *12* (7), 1182–1192. https://doi.org/10.1111/jth.12602.

(44) Filipe, V.; Hawe, A.; Jiskoot, W. Critical Evaluation of Nanoparticle Tracking Analysis (NTA) by NanoSight for the Measurement of Nanoparticles and Protein Aggregates. *Pharm Res* **2010**, *27* (5), 796–810. https://doi.org/10.1007/s11095-010-0073-2.

(45) Silmore, K. S.; Gong, X.; Strano, M. S.; Swan, J. W. High-Resolution Nanoparticle Sizing with Maximum A Posteriori Nanoparticle Tracking Analysis. **2019**. https://doi.org/10.1021/acsnano.8b07215.

(46) Saveyn, H.; De Baets, B.; Thas, O.; Hole, P.; Smith, J.; Van der Meeren, P. Accurate Particle Size Distribution Determination by Nanoparticle Tracking Analysis Based on 2-D Brownian Dynamics Simulation. *J Colloid Interface Sci* **2010**, *352* (2), 593–600. https://doi.org/10.1016/j.jcis.2010.09.006.

(47) Kim, A.; Ng, W. B.; Bernt, W.; Cho, N. J. Validation of Size Estimation of Nanoparticle Tracking Analysis on Polydisperse Macromolecule Assembly. *Sci Rep* **2019**, *9* (1). https://doi.org/10.1038/s41598-019-38915-x.

(48) Fractionation, A. F. F.; Drexel, R.; Siupa, A.; Carnell-morris, P.; Carboni, M.; Sullivan, J.; Meier, F. Fast and Purification-Free Characterization of Hyphenated with Multi-Angle Light Scattering and Nanoparticle Tracking Analysis Detection. **2020**, 1–19.

(49) Sitar, S.; Kejž, A.; Pahovnik, D.; Kogej, K.; Tušek-Znidarič, M.; Lenassi, M.; Zagar, E. Size Characterization and Quantification of Exosomes by Asymmetrical-Flow Field-Flow Fractionation. *Anal Chem* **2015**, *87*, 9225–9233. https://doi.org/10.1021/acs.analchem.5b01636.

(50) Steppert, P.; Burgstaller, D.; Klausberger, M.; Tover, A.; Berger, E.; Jungbauer, A. Quantification and Characterization of Virus-like Particles by Size-Exclusion Chromatography and Nanoparticle Tracking Analysis. *J Chromatogr A* **2017**, *1487*, 89–99. https://doi.org/10.1016/j.chroma.2016.12.085.

(51) Adkins, G. B.; Sun, E.; Coreas, R.; Zhong, W. Asymmetrical Flow Field Flow Fractionation Coupled to Nanoparticle Tracking Analysis for Rapid Online Characterization of Nanomaterials. *Anal Chem* **2020**, *92*, 7071–7078. https://doi.org/10.1021/acs.analchem.0c00406.

(52) Maxwell, J. C. A Dynamical Theory of the Electromagnetic Field. *Philosophical Transactions Royal Society* **1865**, *155*, 459–512.

(53) Rayleigh F.R.S, Lord. X. On the Electromagnetic Theory of Light . *The London, Edinburgh, and Dublin Philosophical Magazine and Journal of Science* **1881**, *12* (73), 81–101. https://doi.org/10.1080/14786448108627074.

(54) Rayleigh F.R.S., Lord. XXXIV On the Transmission of Light through an Atmosphere Containing Small Particles in Suspension and the Origin of the Blue of the Sky. *The London, Edinburgh, and Dublin Philosophical Magazine and Journal of Science.* **1899**, *47* (287), 375–384.

(55) Strutt, J. W. XV. On the Light from the Sky, Its Polarization and Colour. *The London, Edinburgh, and Dublin Philosophical Magazine and Journal of Science* **1871**, *41* (271), 107–120. https://doi.org/10.1080/14786447108640452.

(56) Strutt, J. W. XXXVI. On the Light from the Sky, Its Polarization and Colour. *The London, Edinburgh, and Dublin Philosophical Magazine and Journal of Science.* **1871**, *41* (275), 274–279.

(57) Strutt, J. W. LVIII. On the Scattering of Light by Small Particles. *The London, Edinburgh, and Dublin Philosophical Magazine and Journal of Science* **1871**, *41* (275), 447–454.

(58) Mie, G. Beiträge Zur Optik Trüber Medien, Speziell Kolloidaler Metallösungen. *Ann Phys* **1908**, *330* (3), 377–445. https://doi.org/10.1002/andp.19083300302.

(59) van de Hulst, H. C. *Light Scattering by Small Particles*; John Wiley and Sons: New York, 1957.

(60) Kerker, M. *The Scattering of Light and Other Electromagnetic Radiation*; Academic Press: New York, 1969.

(61) Wyatt, P. J. Light Scattering and the Absolute Characterization of Macromolecules. *Anal Chim Acta* **1993**, *272*, 1–30.

(62) Andersson, M.; Wittgren, B.; Wahlund, K. G. Accuracy in Multiangle Light Scattering Measurements for Molar Mass and Radius Estimations. Model Calculations and Experiments. *Anal Chem* **2003**, *75* (16), 4279–4291. https://doi.org/10.1021/ac030128+.

(63) Wyatt, P. J. Measurement of Special Nanoparticle Structures by Light Scattering. *Analytical Chemistry*. American Chemical Society August 5, 2014, pp 7171–7183. https://doi.org/10.1021/ac500185w.

(64) Øgendal, L. *Light Scattering: A Brief Introduction*; 2019.

(65) Stetefeld, J.; McKenna, S. A.; Patel, T. R. Dynamic Light Scattering: A Practical Guide and Applications in Biomedical Sciences. *Biophysical Reviews*. Springer Verlag December 1, 2016, pp 409–427. https://doi.org/10.1007/s12551-016-0218-6.

(66) Runyon, J. R.; Ratanathanawongs Williams, S. K. Photon Correlation Spectroscopy Coupled with Field-Flow Fractionation for Polymer Analysis. In *Handbook of Spectroscopy*; Gauglitz, G., Vo-Dinh, T., Moore, D. S., Eds.; Wiley, 2014.

(67) Hackley, V. A.; Clogston, J. D. Measuring the Hydrodynamic Size of Nanoparticles in Aqueous Media Using Batch-Mode Dynamic Light Scattering. In *Characterization of*

*Nanoparticles Intended for Drug Delivery, Methods in Molecular Biology*; McNeil, S. E., Ed.; Springer Science, 2011; Vol. 697, pp 35–52. https://doi.org/10.1007/978-1-60327-198-1_4.

(68) Babick, F. Dynamic Light Scattering (DLS). In *Characterization of Nanoparticles: Measurement Processes for Nanoparticles*; Elsevier, 2019; pp 137–172. https://doi.org/10.1016/B978-0-12-814182-3.00010-9.

(69) Saluja, A.; Fesinmeyer, R. M.; Hogan, S.; Brems, D. N.; Gokarn, Y. R. Diffusion and Sedimentation Interaction Parameters for Measuring the Second Virial Coefficient and Their Utility as Predictors of Protein Aggregation. *Biophys J* **2010**, *99*, 2657–2665. https://doi.org/10.1016/j.bpj.2010.08.020.

(70) Connolly, B. D.; Petry, C.; Yadav, S.; Demeule, B.; Ciaccio, N.; Moore, J. M. R.; Shire, S. J.; Gokarn, Y. R. Weak Interactions Govern the Viscosity of Concentrated Antibody Solutions: High-Throughput Analysis Using the Diffusion Interaction Parameter. *Biophys J* **2012**, *103*, 69–78. https://doi.org/10.1016/j.bpj.2012.04.047.

(71) Thiagarajan, G.; Semple, A.; James, J. K.; Cheung, J. K.; Shameem, M. A Comparison of Biophysical Characterization Techniques in Predicting Monoclonal Antibody Stability. *MAbs* **2016**, *8* (6), 1088–1097. https://doi.org/10.1080/19420862.2016.1189048.

(72) Sitar, S.; Vezoč, V.; Mač, P.; Kogej, K.; Pahovnik, D.; Agar, E. Z.ˇ. Pitfalls in Size Characterization of Soft Particles by Dynamic Light Scattering Online Coupled to Asymmetrical Flow Field-Flow Fractionation. *Anal. Chem* **2017**, *89*, 38. https://doi.org/10.1021/acs.analchem.7b03251.

CHAPTER 3

# NEW ADVANCES AND APPLICATIONS IN FIELD-FLOW FRACTIONATION



Christine L. Plavchak[1], William C, Smith[1], Carmen R. M. Bria[2], and S. Kim Ratanathanawongs Williams[1]

## 3.1 Abstract

Field-flow fractionation (FFF) is a family of techniques that was created especially for separating and characterizing macromolecules, nanoparticles, and micrometer-sized analytes. It is coming of age as new nanomaterials, polymers, composites, and biohybrids with remarkable properties are introduced and new analytical challenges arise due to synthesis heterogeneities and the motivation to correlate analyte properties with observed performance. Appreciation of the complexity of biological, pharmaceutical, and food systems and the need to monitor multiple components across many size scales has also contributed to FFF's growth. This review highlights recent advances in FFF capabilities, instrumentation, and applications that feature the unique capabilities of different FFF techniques in determining a variety of information such as averages and distributions in size, composition, shape, architecture, microstructure, and in investigating transformations and function.

## 3.2 Introduction

Nanometer and larger size analytes present formidable analytical challenges as they are often heterogeneous mixtures with distributions in multiple physicochemical attributes or are

[1] Laboratory for Advanced Separations Technologies, Department of Chemistry, Colorado School of Mines, Golden, Colorado, 80401, USA
[2] Tolmar Inc., Fort Collins, Colorado 80524, USA

part of complex mixtures. [1–4] Adding to this complexity, some analytes are dynamic and undergo transformations that lead to changes in size, morphology, or surface chemistry and charge. [5–7] For many of these cases, a separation technique and additional orthogonal methods are needed to obtain a more complete picture. [8–10]

The use of external fields to achieve separations in an open channel lies at the heart of field-flow fractionation (FFF) techniques. One important feature is that it is a family of *elution* techniques and thus lends itself well to coupling with on-line detectors and collection of fractions containing purified or enriched subpopulations. The former creates a platform that incorporates orthogonal analyses of eluting enriched fractions within a single experiment. For example, the size of eluting nanoparticles can be determined from retention time using FFF theory and by on-line multiangle and dynamic light scattering detectors or by single particle ICP-MS (spICP-MS). The FFF separation is important as these detectors benefit from the increased monodispersity of the eluting sample fractions and average values and *distributions* are determined. The ease of fraction collection post-FFF gives access to well defined materials and biological species that are essential for investigating function. These and other attributes such as FFF retention theories that are grounded in first principles, an open channel design that is highly conducive for probing fragile species and for simultaneously monitoring species that span multiple orders of magnitude in size or molecular weight, and flexibility in choice of carrier liquid are some of the hallmarks that will be expanded upon in later sections.

Field-flow fractionation is a group of distinctive techniques that utilize different types of fields such as temperature gradient, centrifugal, and crossflow giving rise to thermal (ThFFF), sedimentation (SdFFF or CF3), and flow FFF (FlFFF), respectively. Figure 3.1 shows the general layout of an FFF channel and the types of fields that have been used thus far along with the separation mechanism. The extent of retention in FFF depends on the magnitude of the interactions between the applied field and physicochemical properties of the analyte and the diffusion coefficient D of each analyte. Both factors lead to opposing transport that results in each analyte occupying a unique velocity streamline of the parabolic flow in the FFF channel. Each analyte is thus driven through the channel at different speeds and elutes at different times. An FFF technique may also have different variants. For example, FlFFF is commercially available in an asymmetrical (AF4) or a hollow fiber (HF5) channel format. Sample introduction and the requisite relaxation into unique equilibrium layers prior to the start of the separation can be implemented using different processes that include stopflow (used in SdFFF), focusing flow (used in AF4), and frit inlet (FI) sample introduction with hydrodynamic relaxation. In addition to different equipment, each FFF technique also has distinctive theories that relate retention time to analyte properties. [2,11] FlFFF separates on the basis of differences in $D$ (or hydrodynamic diameter $d_h$), SdFFF separates according to differences in effective mass (or diameter and density difference between the analyte and the carrier liquid), and ThFFF differentiates according to analyte Soret coefficients (or the ratio of thermal diffusion coefficient $D_T$ to $D$). For more details on retention theories and processes specific to each type of FFF field, refer to References 2, 4, and 11.

This review highlights the latest advances in FFF technology over the past decade and how FFF has contributed to the characterization of biological particles, naturally occurring and engineered nanoparticles, and polymers and the understanding of transformations such as protein aggregation kinetics, nanoparticle degradation, and protein coronas. Practical considerations for FFF operation and challenges and opportunities are also discussed.

The work described in this thesis is centered around advancements in AF4 for biological vesicle characterization and ThFFF for colloid characterization. While the material covered within this review spans far beyond the topics of this thesis, this chapter will highlight the sections that support the work showcased in this dissertation in conjunction with the advancements of related particle characterization.

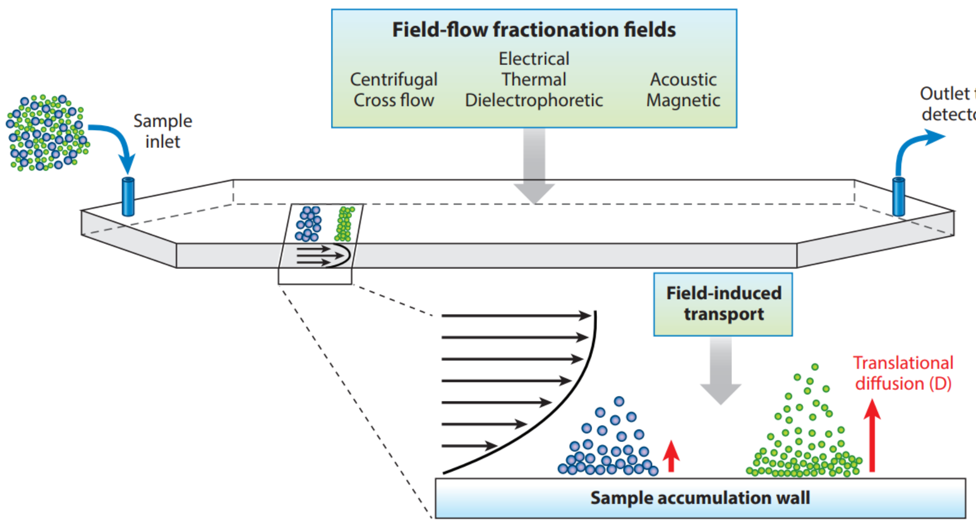


Figure 3.1 A simplified scheme of a field-flow fractionation (FFF) channel operating in normal mode. As analytes enter the channel, the applied field interacts with specific physicochemical properties of the analyte transporting it to the sample accumulation wall. The analyte's translational diffusion counteracts the field-induced transport, creating a steady state. This interplay leads to the formation of sample clouds whose average positions are in different flow velocity streamlines of the parabolic flow. In this schematic, the smaller particles diffuse faster and elute before the larger particles. FFF instruments with different externally applied fields, e.g., centrifugal, cross flow, electrical asymmetrical flow, and thermal, are available commercially. Electrical, acoustic, magnetic, and dielectrophoretic fields have also been successfully implemented.

## 3.3 Applications

### 3.3.1 Cells and Subcellular Particles

The use of FFF in bioparticle characterization spans predictive diagnosis to biomarker discovery and therapeutic development. FFF's ability to separate and elute fractions of different size and mass components and coupling with multiple analytical methods has advanced understanding of biological content and function for cells, lipoproteins, extracellular vesicles (EVs), ribosomes, viruses, and virus-like particles (VLPs). Tumor formation, purification, and subassembly formation have also been examined leading to insights in protein expression for diagnostics and vaccine development. [12,13] AF4 has been most utilized for these applications with additional contributions from FlFFF, SdFFF, ElFFF, and DEPFFF. The majority of FFF separations of bioparticles occur in the normal mode (< ~1 μm) with cell separations occurring in steric/hyperlayer mode (> ~1 μm).

Label-free cell-sorting is important for reducing costs of cell isolation in biological and clinical research. Current cell-sorting techniques rely heavily on cell-specific markers or chemical labels which lead to cell differentiation, apoptosis, and potentially impact successive cultures. Hyperlayer mode SdFFF has shown promise as a tag-less, noninvasive method for cell sorting. [14] These advantages were demonstrated with human pluripotent stem cells and progenital cells. [15] Tumor initiating cells (TICs) are usually in low abundance (~1-5%) but are responsible for driving tumor growth and treatment resistance. SdFFF-sorted TICs were amplified to study tumor development, apoptosis, proliferation, vascularization, and protein expression. [12] Cancer stem cells (CSCs) have been hypothesized to have variances in cell differentiation if grown on Classic Medium compared to colorectal cancer-specific defined medium. [16] This effect was confirmed with SdFFF. Additional efforts have focused on astrocyte subpopulations to help foster therapeutic approaches for improving neural stem cell function. [17,18] While SdFFF has been dominant in cell-sorting, HF5's smaller volume is well suited for analyzing sub-μL sample volumes of. Interestingly, HF5 columns are low-cost and can be interchanged with the column on an HPLC system. [19,20] The separation of tumor cells from blood cells and other cell types has been explored using DEPFFF. [21,22] The magnitude of the applied electric field can be constrained to localized regions of the channel and targeted tumor cells can be levitated and ablated at higher microchannel positions. This configuration allows tumor cells to be removed while blood cells remain unharmed at the accumulation wall. [21]

Analytical AF4 and semipreparative SP-AF4 have both contributed to advanced lipidomic characterization and aided in identifying lipoprotein markers for disease diagnostics. [23–26] Analytical AF4 with offline LC-MS/MS is used for multiplexed lipoprotein analysis and allowed in-depth understanding of size-dependent compositional differences. [23] Lipidomic analysis of SP-AF4 fractionated lipoproteins via nanoflow ultrahigh performance liquid chromatography-tandem mass spectrometry (nUHPLC-ESI-MS/MS) introduced potential diagnostic methods for coronary artery disease (CAD), acute coronary syndrome (ACS) [24], Alzheimer's [25], and postmenopausal osteoporosis. [26] Lipoproteins from CAD, ACS, and Alzheimer's patients had distinct differences in their lipidome when compared to healthy control groups. Beyond evolving diagnostics and lipidomic analysis, a comparison of samples prepared by SP-AF4 and UC showed a 98% overlap in HDL and LDL lipidome. [27] Additionally, SP-AF4 isolated higher protein amounts per sample volume; was significantly faster (~1 hour instead of multiple hours or days); and used buffers with lower ionic strengths thereby reducing the likelihood of lipoprotein aggregation, damage, or apolipoprotein dissociation. The ability to obtain quantitative measurements of lipoproteins with low starting volumes of serum (100 µL) post fractionation is significant compared to other methods.

Exosomes and EVs have come of interest due to their potential as biomarkers and therapeutics and their role in cell signaling. The main challenge of characterizing these vesicles is the lack of knowledge of their biogenesis, composition, and biodistributions. FlFFF with offline nUPLC-ESI-MS/MS analysis of pancreatic cancer exosomes helped determine disease status and elucidate size-dependent lipidomic differences. [28] A landmark study used AF4-MALS-DLS to isolate exosome subpopulations of melanoma cells (Figure 3.2).[29,30] Post-fractionation biochemical analyses revealed that each subpopulation had unique lipid, protein, and nucleic acid expression depending on the size, cell type, and vascular membrane structure. The in-depth protocol on exosome AF4 fractionation provided a framework for further developing EV separations. Beyond size and composition, the surface charge of EVs is also of interest and has been examined using cyclical electrical FFF (CyElFFF). [31]

AF4 and CyElFFF applications have expanded further into ribosomes [32], viruses [33], and virus-like particles (VLPs). [34] Recent work in this area has led to new questions in virology, how these materials are classified, and purification. [35] AF4's low shear mitigates undesirable changes associated with traditional methods like UC and sodium dodecyl sulfate-polyacrylamide gel electrophoresis (SDS-PAGE). Gentle purification using AF4 provided the unaltered samples necessary for identifying genome expression in the protein shell and lipid envelope. These two components are specific to host recognition of the virus and are vulnerable to biophysical and biochemical stresses used in traditional purification techniques. [33] AF4 purification of enveloped bacteriophages like Φ6 is gaining interest because of their similarities to animal viruses. The use of anionic detergents, known to affect bacteriophage purification and separations, can be eliminated by using AF4 instead of SDS-PAGE. This is typically due to residual detergent or major proteins being released from the phage. [36] Beyond purification, AF4 has been used to study the disassembly of complex virions of phage Φ6. Through controlled dissociation treatments, biologically active subassemblies were identified based on their three distinct structural layers. [37] CyElFFF-MALS-DLS has been utilized to determine electrophoretic mobilities of three Q beta bacteriophage VLPs containing different surface peptides. [13] Understanding surface composition and partial separation of monomer and aggregated VLPs initiates further opportunities for CyElFFF use in VLP characterization.

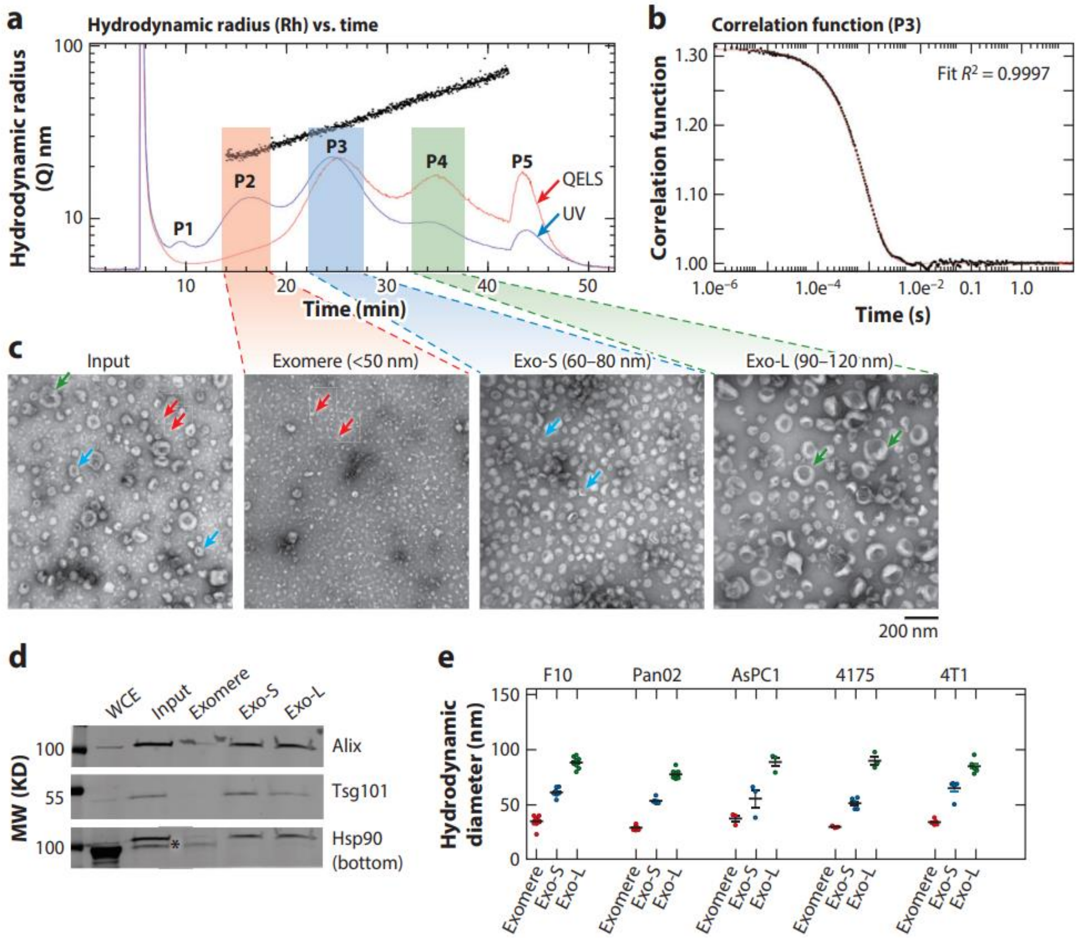


Figure 3.2 AF4 separation followed by orthogonal analyses have led to further understanding of extracellular vesicle (EV) heterogeneity. (a) AF4 separation of B10–F16 melanoma cells extracellular vesicles with ultraviolet spectroscopy (UV) and dynamic light scattering (DLS) detection shows five distinct peaks P1–P5 that correspond to unretained analytes (P1), a new class of vesicles termed exomeres (<50 nm, P2), small exosomes (60–80 nm, P3), large exosomes (90–120 nm, P4), and large aggregates (P5), respectively. The line above the fractograms correspond to the hydrodynamic radius and confirms differences in size as a function of retention time. (b) A correlation function in QELS (quasielastic light scattering, also known as DLS) analysis corresponding to P3. (c) Transmission electron microscopy (TEM) images show vesicles in the stock solution prefractionation and P2–P4 fractions collected after AF4 separation. (d) Western blot analyses confirmed the presence of exosomal proteins in whole-cell extract (WCE), exosome and exomere mixture (input), and three fractionated subpopulations. (e) Different cell lines F10, Pan02, AsPC-1, 4175, 4T1 show similar size distributions for all three populations of vesicles. Figure adapted with permission from Reference 29; Copyright 2018 Springer Nature. Other abbreviation: MW, molecular weight

### 3.3.2 Engineered and Naturally Occurring Nanoparticles (ENPs and NNPs)

The broad separation range and versatility of FFF provides a beneficial platform for the analysis of ENPs and NNPs with the majority studies employing AF4 and SdFFF.[38] Typically, ENPs include metallic, metal-oxide, and polymeric nanoparticles (NPs) while biopolymers, dissolved organic matter, and colloidal inorganic minerals are considered NNPs. Model ENPs systems (polystyrene latex (PSL) or $SiO_2$) are also commonly used to calibrate and evaluate FFF separations.[39] Studies of ENPs and NNPs cover fate and transport, particle transformation, and interactions in complex media. Several comprehensive reviews cover ENPs and NNPs as-synthesized[40], in the environment[41,42], consumer goods[43], and food.[44]

As nanomaterials have become more common in consumer products, ENPs are inevitably released into the environment. ENPS and NNPs cannot be discriminated by size alone and composition-sensitive detectors have proven to be important.[44] AF4 coupled to ICP-OES, ICP-MS, and spICP-MS is an increasingly used combination.[45–47] These methods have enabled comprehensive size and composition characterization of ENPs which is important for understanding their risk and fate in environmental matrices.[48] Optimized extraction methods prior analysis have shown that elemental ratios can be used to differentiate ENPs like $TiO_2$ and $CeO_2$ from naturally occurring NNPs in soils.[49] Other FFF techniques like ThFFF or SdFFF can separate ENPs based on their size and surface or bulk composition to identify compositional heterogeneity. ThFFF separation and characterization of metallic and metal-oxide NPs as well as multicomponent hybrids have exploited differences in NP thermal diffusion originating from surface and bulk composition differences (Figure 3.3a-d).[50] SdFFF utilizes differences in effective mass for separating particles with differing bulk composition.[51] Effective mass and particle volume from SdFFF and TEM independently has also allowed comparative particle densities to be calculated.[52]

When ENPs enter different chemical environments they have the propensity to transform through aggregation, absorption, and/or dissolution mechanisms.[53] Investigation of these transformations especially below 10 nm is important to understanding the fate, risk, and transport of ENPs in the environment. Figure 3.3e-f shows the AF4-UV-ICP-MS separation of n-vinyl-2-pyrrolidone protected silver nanoparticles (Ag-PVP) in the presence of tripeptide glutathione (GSH).The presence of GSH transformed the Ag-PVP from a single larger NP population into a heterogeneous mixture composed of $Ag^+$, nanoclusters, and small NPs.[5] Optimization of AF4 separation conditions enabled the identification of distinct NP and nanocluster subpopulations. This is the first study demonstrating AF4 isolation of ~ 1 nm nanoclusters. Transformed particles exist in a spectrum that commonly goes unnoticed, particularly, when they are introduced to environmental or biological systems.[54] Multidetector approaches can identify and quantify species in this low size range and provide further insight into the size-specific risks associated with individual subpopulations of ions, metal-ligand complexes, nanoclusters, and nanoparticles.

Carbon based nanomaterial (fullerenes, carbon nanotubes, graphene, etc.) provide an additional challenge due to colloidal stability[55] and aggregation.[56] High resolution methods have been developed[57] to further understand aggregation mechanisms[6] and probe ENPs interactions with NNPs to study their fate in complex environmental media.[58] Characterization of particle shape (structure, aspect ratios, etc.) has been of specific interest and highlight the benefits of AF4.[59–61] It is important to note that both the NP surfaces and carrier fluid composition can also strongly influence aggregation as well as interactions with the AF4 accumulation wall.[62]

The potential environmental and health impacts of microplastics and nanoplastics is a topic experiencing intense interest.[63] Both types of particles are highly challenging to separate and analyze in an expedient manner because of their low numbers. AF4 in normal and steric modes demonstrated similar recoveries of nanoplastics and microplastics compared to AUC.[3] AF4-MALS was used to detect nanoplastics in complex food matrices like fish and helped optimize digestion protocols.[64] Pyrolysis GC-MS and online Raman microspectroscopy added important chemical characterization capabilities to the analysis of nanoplastics.[3,9]

The interaction of analytes with the sample accumulation wall and the subsequent effect on retention time opened a new avenue of research. Analyte-wall interactions are generally governed by electrostatic and van der Waals forces, the sum of dispersion forces can be described in terms of the Hamaker constant. Care is often taken to select a FlFFF membrane that minimizes these interactions based on the surface coating of the particles in question.[65] Similar sized nanomaterials have shown variation in AF4 retention time which can be correlated to these interactions via the Hamaker constants of the membrane and analyte.[66] This link has enabled the development of an AF4 method for calculating an effective Hamaker constant for a given material in a variety of conditions and in various solvents.[67] The ability to predict repulsive and attractive forces between particles and substrates could play an influential role in the development of colloidal assemblies and thin film technologies. Accordingly, this approach opens a new path for the study of interactions at nanomaterial surfaces and the role of surface functionalization.

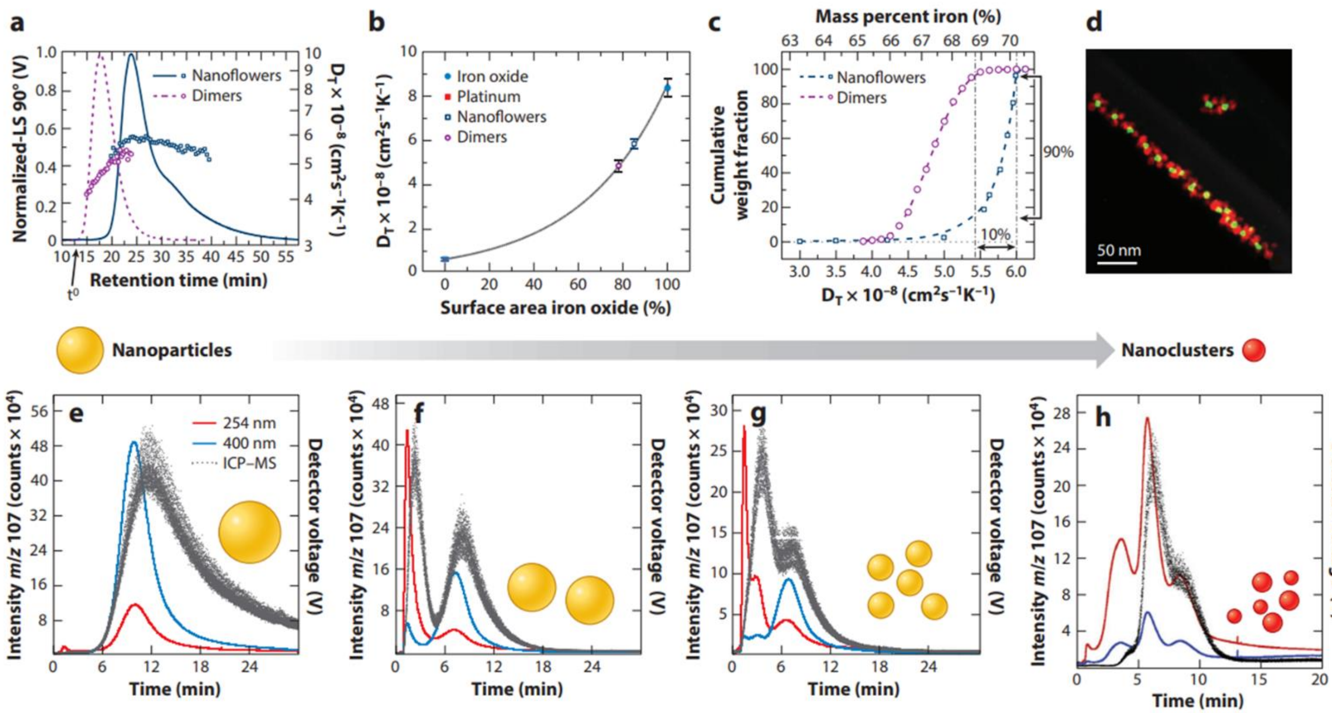


Figure 3.3 Capabilities of ThFFF and AF4 include composition distribution analysis of hybrid NPs and examination of NP-to-nanocluster (size) transformations, respectively. ThFFF composition sensitivity is reflected by the measured differences in thermal diffusion coefficient ($D_T$). *(a)* ThFFF fractograms of Pt-$Fe_3O_4$ hybrid NPs and variation in $D_T$ as a function of retention time. These variations in $D_T$ suggest compositional heterogeneity. (*b*) A thermal ($D_T$) calibration plot shows unique values for iron oxide particles and platinum cubes, dimers and nanoflowers. (*c*) Cumulative weight fraction plots using $D_T$ reveals that 90% of the nanoflowers sample are compositionally monodisperse (mass % iron of 69–70%) while the dimers sample has more composition variation (90% dimers have a mass % iron of 66–70%). Nanoflower composition was verified using (*d*) Transmission electron microscopy- energy dispersive X-ray spectroscopy (TEM-EDS) elemental mapping high-angle annular dark field scanning (HAADF) of fractionated samples. Panels *a-d* with permission from Reference 49; copyright 2018 American Chemical Society. Asymmetrical flow field-flow fractionation-inductively coupled plasma mass spectrometry (AF4-ICP-MS) can monitor changes to *N*-vinyl-2-pyrrolidone-protected silver NPs (PVP-AgNPs) (*e*) prior to the addition of excess glutathione (GSH), (*b*) 80 minutes after the addition of GSH and (*c*) 4 days after. Fractograms (*e–g*) show retention time changes that correlate with NP transformations to smaller diameter species. (*h*) The AF4 method was further optimized to resolve three distinct populations of nanoclusters (1.8, 2.5, and 5.5 nm). Panels *e-h* adapted with permission from Reference 5; copyright 2013 American Chemical Society. Other abbreviation: LS, light scattering

### 3.3.3 Nanomaterials in Drug Delivery: Nanocarriers and Nanomedicines

Nanotherapeutics often take the form of polymer micelles and dendrimers, polymersomes, liposomes, stable emulsions, porous nanoparticles, and other 'nanocarriers'. Many of these require a gentle separation technique due to their delicate structures. This challenge makes AF4 uniquely suited for the analysis of biomedicines and in-depth reviews of FFF for this can be found elsewhere.[68–70] The use of FFF has several benefits over batch methods like DLS including the quantification of populations undergoing aggregation or dissolution and examination of changes associated with drug delivery, storage, and release.[71–73]

Polymeric nanocarriers including micelles, dendrimers, and polymersomes can be produced over a wide size range and with tunable chemical functionality. This flexibility enables them to carry both hydrophilic and hydrophobic therapeutics as well as control stability, lifetime, and therefore release of drugs. The chemistry of the nanocarrier components and the composition of formulation buffer strongly impact the size, volume, and morphology of polymer micelles.[74] Studies of block copolymer micelles via AF4-MALS-DLS determined the size, shape, and MW of such particles. In conjunction with hyphenated detection, changes in these properties with respect to the carrier fluid composition can be monitored and related to degradation and aggregation.[75,76] AF4-UV/vis-MALS has be used to study the impact of nanocarriers size and colloidal stability on uptake, in vitro toxicity, and encapsulation of dyes for photodynamic therapy in block copolymer micelles.[77] The release of therapeutics can be controlled via several mechanisms including the response of nanocarriers to changes in the external chemical environment. The formulation and stability of polymersomes have been studied with respect to responses in variation of external pH and ionic strength.[78] As observed in similar studies, a change in the pH environment  may cause micelles to undergo morphological deformation and degradation[79] These studies highlight AF4's applicability to investigating formulation-based control on micelle morphology and how morphologies may exhibit differing degradation pathways and responses to changes in external environment. Similarly, porous inorganic and organic nanomaterials have shown promise for the loading and targeted delivery of proteins, dyes, and other therapeutics.[80] Formulation of metal-organic-frameworks for drug delivery have been studied by AF4-MALS highlighting the ability to monitor morphological changes, formation of aggregates, and impact of drug loading on particle stability.[81]

Nanostructured lipid carriers[82] and other emulsion-prepared therapeutics[83] for specific drug delivery have recently gained attention, with AF4 becoming a preferred method for particle characterization. Measurement of particle size distributions in medicinal products is especially important for understanding the biological effects of lipid-based nanotherapeutics.[7] Understanding the aggregation, interaction, and assembly of liposomes with existing micelles and vesicles in biological matrices is necessary for a mechanistic understanding of the bioavailability and uptake of poorly water soluble hydrophobic drugs.[84] Although AF4 is a gentle separation technique compared to centrifugation and SEC, typical AF4 methodology involves a sample focusing step which has been noted to cause fusion of very small lipid particles into larger mixed micelles.[72] To circumvent problems during focusing, researchers have investigated frit inlet versions of both FlFFF and AF4 and shown them to be good options.[85] Specific uses of frit inlet FFF are discussed in Section 3. FlFFF techniques continue to meet the accelerating characterization needs of regulatory science[86] and help further development of new nanotechnology enabled pharmaceuticals and nanoformulations.[87]

### 3.3.4 Assemblies and Complexes: Interactions of Polymers, Proteins, and Particles

Biologically derived drugs show promise for drug delivery and treatment. Assessing the interactions of these therapeutic candidates allows for a deeper understanding of factors controlling their efficacy. Aptamer-protein complexation was studied using a creative experimental design that exploited the physical characteristics of the AF4 channel. The crossflow 'field' dictates that the channel wall must be semipermeable so analytes are retained but carrier liquid can permeate through. This feature enabled incubation of the aptamer-protein solutions during the focusing/relaxation step within the AF4 channel followed immediately by separation and measurement of dissociation constants for aptamer-protein complexes.[88] Determination of weak dissociation constants at µM level were also shown for protein complexes, highlighting the potential for characterizing challenging binding systems.[89]

Protein therapeutics show promise for disease treatment but the formation of aggregates in formulations can reduce efficacy and potentially increase immunogenicity. AF4 provided the essential separation of anti-streptavidin IgG monomer from aggregates while MALS-dRI reported MW of the eluting subpopulations. These data were fit to the Lumry-Eyring nucleated polymerization model and kinetic analysis suggested that slow nucleation and aggregate condensation were the main pathways to the formation of nanometer and submicron aggregates[90] In addition, FFF's characteristic open channel permitted a comparative study of uncentrifuged and centrifuged heat stressed anti-SA IgG. (Centrifugation is commonly used as a sample preparation step to remove large size species that can clog chromatography columns.) AF4-MALS-dRI results suggested that the removal of large aggregates may influence aggregation kinetics. Polymeric protective agents that prevent aggregation during heat stress of IgG proteins were also studied using AF4.[91] Near the IgG unfolding temperature, polymer agents formed complexes with IgG to slow aggregate formation. Whole blood separation by AF4 often requires extensive pre-treatment due to the large number of blood cells, platelets, and plasma present. However, a new AF4 method characterized protein therapeutics and their aggregates in whole blood[92] This is an exciting development that facilitates better understanding of biotherapeutic behavior in complex biological media without disturbing aggregate species during sample preparation. Despite these successes, AF4 method development should consider the impact of sample injection, focusing, and separation on delicate or transient aggregate populations.[93] Additionally, the composition of the carrier fluid can impact protein retention due to protein-protein interactions and protein-membrane interactions.[94]

Potential use of nanoparticle therapeutic delivery agents along with the prevalence of nanomaterials in the environment has raised questions about the fate of these material in biologically-relevant media.[95] AF4 characterization of functionalized nanoparticles[96], antibody-nanoparticle conjugates[97–99], functionalized carbon nanotubes[100], and protein-nanoparticle adsorption[101] has shown promise for understanding these complex systems. The protein corona formed on nanoparticle surfaces in biological media has also been studied. The nature of the protein corona-nanoparticle interactions and the relative dissociation rate of the protein corona were screened using AF4 and UC.[102] The separation mechanism in AF4 allowed fast dissociating proteins to be isolated from slow dissociating proteins and the nanoparticles. Differences in protein dissociation rates as nanoparticles moved between different environments could have important implications for the protein corona. AF4 was compared to UC in order to show that loosely bound proteins (soft corona) could be preserved.[103] In this study, PSL particles were incubated with human plasma and then separated using AF4 or UC. The identification of more HSA and IgG proteins associated with the particles separated by AF4 confirmed the preservation of the soft protein corona compared to UC. Access to such nanoparticles allowed further studies that concluded that only the hard protein corona impacted cell uptake behavior. Topological features of large biohybrid systems may play an important role in their applications but are challenging to analyze. Avidin and biotinylated glycodendrimer (GD-B) complexes were formed by varying the degree of biotinylation and the ligand−receptor stoichiometry and characterized by AF4-MALS-DLS-dRI.[104] The apparent density, determined from the measured size and MW, and the MW dependence of the shape factor ($\rho = r_{rms}/r_h$) were examined to understand the scaling behavior of the avidin/GD-$B_x$ structures. Conformation plots of ρ as a function of MW suggested a transformation from stiff rod-like structures to more branched microgels. This type of in-depth characterization is important for understanding the structure-function relationship of these large, complex biohybrid systems.

Polymeric assemblies have potential use as delivery vectors for therapeutic treatments. Size and shape characterization for these assemblies is important for understanding their efficacy and function. Amphiphilic poly(ethyleneoxideb-ε-caprolactone) (PEO-b-PCL) and poly(ethylene oxide-b-methylmethacrylate) (PEO-b-PMMA) block copolymer self-assemblies were characterized by AF4-MALS-DLS-dRI and the results compared to batch-mode light scattering, transmission electron microscopy, and atomic force microscopy to understand the morphologies of the formed polymersomes.[79] Separation and identification of PEO-b-PCL micelles and vesicles by AF4 aided understanding of the synergistic effects of polymersome morphology on photodynamic therapy cancer treatments.[105] Comparison of AF4 and batch-mode DLS showed the poor suitability of the latter to accurately characterize complex mixtures of micelles and vesicles. The AF4-determined micelle and vesicle morphology distributions could be used to better understand the impact of polymersome morphology on the efficacy of photodynamic therapy during *in vitro* testing.

The analysis of shear-sensitive assemblies and complexes requires consideration of the FFF process, particularly, the sample relaxation or focusing step where undesirable alteration of samples may occur. In such cases, FI-FlFFF systems have proven to be a good alternative. FI-FlFFF and FI-AF4 were shown to be suitable for characterizing shear-prone polyion complexes (PICs).[106] Batch DLS measurements and conventional AF4 were unable to accurately characterize the complexes and dissociated the PICs, respectively. FI techniques not only preserved the self-assemblies but also identified changes in PIC compositions as a function of NaCl concentration. FI-AF4 has also improved characterization of high molecular weight biopolymers such as glycogen and pullulan compared to conventional AF4.[107] The main drawback with FI systems is lower separation resolution compared to conventional AF4.

The use of FFF to detect weakly bound biopolymer complexes, acquire topological information about biohybrid complexes, and determine the structures of micelles in complex mixtures represent state-of-the-art analyses. These types of studies are not as straightforward as the well-documented capability of AF4 and light scattering to determine size and molar mass distributions. Despite significant method development and data analysis, this information content is difficult to achieve using other methods.

### 3.4 Developments in Instrumentation and Analysis

Over the past decade, new applications have expanded FFF use while advancing instrumentation and online detection capabilities have elevated FFF into emerging fields. AF4's widespread use has led to many developments in channel design and online instrumentation. Comparison of analytical AF4 channels with SP-AF4 has evaluated how channel design impacts overloading behavior and resolution.[108] This work provides insights into SP-AF4 in both aqueous and organic solvents highlighting SP-AF4's potential in characterizing and collecting milligram quantities of different nanoparticles.

At the analytical scale, microstructured membranes were developed and examined in efforts to increase retention, selectivity, and resolution. By hot-embossing a 30 kDa regenerated cellulose membrane with perpendicular grooves, an increase in retention of BSA, γ- globulin, apoferritin, and thyroglobulin was achieved.[109] Further optimization with lower MWCO membranes, membrane fabrication processes, and COMSOL modeling helped increase the selectivity and resolution for smaller MW analytes. This initial structured membrane work led to a potentially high-throughput 2-D fractionation for proteins and nanoparticle mixtures using FI-AF4.[110]

Longstanding analysis centered around metal nanoparticles and aquatic samples has led to developments with coupling of ICP-MS with AF4. Due to MWCO limitations for AF4 membranes, an interface was recently developed to direct crossflow fluid from AF4 into the ICP-MS.[111] Monitoring the dissolved analytes in the crossflow and particulates in the channel flow of AF4 with ICP-MS increased efficiency for analysis. The abundance of particles between 0.3 - 1 kDa in natural waters has led to the use of low (~300 Da) MWCO membranes which necessitated channel modifications to handle higher channel pressures.[112] Low MWCO membranes used for dissolved organic matter could open a new realm of analysis to AF4 that has often been dominated by SEC including oligomeric polymer species in a variety of solvents as well as better facilitate the monitoring of degradation and dissolution of ENPs by ICP-MS. Comparison of spICP-MS and AF4-ICP-MS in regard to size resolution and multi-form metal analysis has shown AF4-ICP-MS to have better size resolution, providing understanding of nanoparticle complexation and aggregation.[113]

Beyond ICP-MS, other novel detection schemes have recently been coupled to AF4 channels including a liquid waveguide capillary cell (LWCC)[10], optical-trap-based Raman flow cell[9], and a γ-ray detector.[114] A longer optical path length for the capillary cell coupling LWCC to AF4 has provided enhanced sensitivity of silver nanoparticles down to the ppb (ug/L) level without any pre-concentration steps. The development of optical-trap flow cells for Raman microspectroscopy and coupling to AF4 and CF3 (or SdFFF) is a major breakthrough in on-line chemical analysis for < 1 μm particles. This has allowed the identification of PSL and polymethylmethacrylate particles[9] and overcomes the size and compositional limitations observed in traditional Raman spectroscopy. Coupling a γ-ray detector to an AF4 channel serves as a steppingstone for the analysis of theragnostic particles used in radiation and alpha therapy. This powerful tool consolidates analysis time by monitoring liposome sizes and retention of radioactive metal within the lipid vesicles. This allows AF4 to be used in tracking the dissolution, release, and retention of radioactive components in vesicles after they are incubated in biologically relevant media like human blood serum.

The rise in bioparticle analysis has led to increased interest in particle counting. Traditional batch-methods like flow cytometry (FC), particle tracking analysis (PTA), and resistive pulse sensing (RPS) are often hindered by polydisperse analytes, instrument sensitivity, and operator error.[115,116] More recently NTA has been successfully coupled to AF4 and its potential for on-line particle counting was demonstrated.[8] Particle counting with AF4-MALS is also gaining attention yet little work has been done in this area thus far.[117,118]

Recently updated designs have been implemented to analyze particles spanning the 1-10 μm size range utilizing an acoustic force field for a separation based on particle size, density, and physical properties of the solvent. Unlike previous acoustic FFF systems where the acoustic radiation forces provide lift to sedimenting particles (in opposition to the gravitational field), this system was designed to suppress diffusive and lift forces by accelerating sedimentation velocity [119]. This novel approach minimized sample relaxation time enabling faster analyses over a wider separation range and with enhanced resolution over traditional gravitational FFF. These advancements make acoustic FFF a promising technique for high throughput screening of micron sized particles.

Surface charge is important to understanding macromolecular and particle interactions. This capability was realized by the introduction of electrical asymmetrical flow FFF (EAF4) which can separate particles and macromolecules by size and charge while providing orthogonal determination of electrophoretic mobilities and zeta potentials.[120] EAF4 is an improvement over phase analysis light scattering for polydisperse systems as it can measure the *distribution* of surface charges as a function of size. PSL beads and proteins showed increased resolution and fractionating power over FlFFF techniques.

### 3.5 Practical Considerations

Proper selection of FFF technique, separation conditions, carrier liquid, sample accumulation wall, and detection methods are central to obtaining meaningful results. Most recent work addressing these practical considerations focus on AF4 but can be applied to all FFF techniques. The wide range of AF4 applications have led to many sample-specific methods. The creation of a standard method development workflow for nanoparticle characterization by AF4 provides guidance for novice and expert users[121] and the standardization of AF4 and CF3 methods has been established in an ISO method.[122] A critical overview of FlFFF also provides users with the fundamental theory and relevant factors that impact analysis.[123] The overview offers practical recommendations for common problems, a discussion of the strong and weak points of FlFFF, and recommendations for good method development and reporting practices. Other recent publications present excellent practical and theoretical discussions.[124–130] Some additional impactful and practical examples are reviewed below.

Carrier fluid ionic strength is important for controlling electrostatic interactions between the FlFFF membrane and analytes. Ions can accumulate near the semi-permeable membrane and reduce the Debye length leading to increased particle-membrane interactions and thus sample loss.[131] Higher charge state anions accumulate more than lower charge state anions highlighting the need for careful carrier fluid composition selection. Sample composition is also important for selecting FFF conditions because the sample loss mechanism can vary significantly between samples. Gold nanoparticles stabilized by citrate or PEG chains with varying MW were shown to have different sample loss mechanisms during AF4 analysis.[132] The relatively weakly bound citrate compared to the covalently bonded PEG chains resulted in more sample loss for citrate stabilized AuNPs than PEG-stabilized particles. Most of the sample loss for citrate AuNPs was due to the PEEK tubing rather than the AF4 membrane. At low ionic strengths, electrostatic repulsion between particles and the membrane resulted in lower sample loss; higher ionic strengths led to increased sample loss due to bridging interactions between the PEG chains and the membrane. Additionally, membrane “hot spots” of AuNP adsorption were observed which is a reminder that membrane heterogeneity still remains a weak point for FlFFF.[133]

The FFF separation mechanism under ideal conditions is well established. Recent work has strengthened the understanding of how non-idealities influence separation. For instance, the impact of cooperative diffusion of silica nanoparticles was demonstrated during AF4 analysis.[134] Faster diffusing 50 nm particles were shown to significantly increase the diffusion of the slower diffusing 100 nm particles resulting in poor size resolution. Cooperative diffusion effects could be eliminated by reducing sample load and reducing Debye length by adding sodium dodecyl sulfate. Theoretical and experimental studies of the impact of secondary relaxation during flow programming as well as improvements to determining the channel thickness parameter have also been reported.[124,125] Recent theoretical work which calculated the non-parabolicity correction of laminar flow profiles in fifty-nine solvents will continue to improve accuracy of the retention parameter determined for ThFFF.[135]

Coupling light scattering detectors with FFF separations has become standard practice and enables fast, accurate, and in-depth characterization. The shape factor ($r_{rms}/r_h$) obtained from online MALS and DLS measurements allow particle shape determination. However, the accuracy of these measurements is key to ensuring proper determination of the shape factor. Channel or detector flow rate has been shown to impact DLS measurements due to additional translational motion along with Brownian motion and analyte deformation.[136] Increasing flow rate from 0.2 to 1 mL/min had a significant impact on DLS accuracy for particles $\geq$ 100 nm with higher flow rates and larger particles contributing to the largest errors. Manufacturers have recognized erroneous DLS measurements and advancements have been made to improve accuracy. Extension of the Rayleigh-Ganz light scattering theory to more complex nanoparticle structures such as ellipsoids, rods, tubes, etc. allow for complex shape characterization.[137] For instance, determining rod length distributions using a rod model can be done directly from FFF-MALS data when the rod diameter is known. The parallel development and understanding of FFF separations and MALS analysis for non-spherical particles is an exciting path forward. The expansion of FFF techniques to new users and challenges continues to push current instrument capabilities.

## 3.6 Conclusions and Future Trends

Field-flow fractionation continues to be used for separating and characterizing macromolecules, nanoparticles, colloids, and micrometer-size particles with the goal of determining average size, molecular weight, density, etc. as well as distributions representative of heterogeneity in these various primary properties. In recent years, FFF techniques coupled with orthogonal analyses have broadened the scope to investigative studies of increasingly complex systems where questions such as nanomaterials transformations and bioparticle functions can start to be answered. In doing so, FFF has helped tie different fields together. Moving forward, FFF will likely play an important role in new fields such as nanoplastics and their environmental and biological impacts, smart materials design and function, and extracellular vesicles classification and purpose. Challenges and opportunities are plentiful - improved membranes for AF4 and methods to obtain a reproducible membrane surface from day-to-day; better understanding of thermal diffusion and other secrets it may hold with respect to unlocking new characterization capabilities; standardization protocols for specific high impact applications; decreased instrumental band broadening; further flatten the learning curve for new users through simulations and machine learning; develop sensitive on-line composition detectors and capabilities for nonspherical analytes – to name a few.

## 3.7 Acknowledgements

This work was supported by a grant from the US National Science Foundation (CHE-1808805).

## 3.8 References


(1) Johnston, L. J.; Gonzalez-Rojano, N.; Wilkinson, K. J.; Xing, B. Key Challenges for Evaluation of the Safety of Engineered Nanomaterials. *NanoImpact* **2020**, *18*, 100219–100229. https://doi.org/10.1016/j.impact.2020.100219.

(2) Williams, S. K. R.; Runyon, J. R.; Ashames, A. A. Field-Flow Fractionation: Addressing the Nano Challenge. *Anal Chem* **2011**, *83* (3), 634–642. https://doi.org/10.1021/ac101759z.

(3) Mintenig, S. M.; Bäuerlein, P. S.; Koelmans, A. A.; Dekker, S. C.; van Wezel, A. P. Closing the Gap between Small and Smaller: Towards a Framework to Analyse Nano- and Microplastics in Aqueous Environmental Samples. *Environ Sci Nano* **2018**, *5* (7), 1640–1649. https://doi.org/10.1039/C8EN00186C.

(4) Contado, C. Field Flow Fractionation Techniques to Explore the "Nano-World." *Anal Bioanal Chem* **2017**, *409* (10), 2501–2518. https://doi.org/10.1007/s00216-017-0180-6.

(5) Pettibone, J. M.; Gigault, J.; Hackley, V. A. Discriminating the States of Matter in Metallic Nanoparticle Transformations: What Are We Missing? *ACS Nano* **2013**, *7*, 2491–2499. https://doi.org/10.1021/nn3058517.

(6) Gigault, J.; Grassl, B. Improving the Understanding of Fullerene (NC60) Aggregate Structures: Fractal Dimension Characterization by Static Light Scattering Coupled to Asymmetrical Flow Field Flow Fractionation. *J Colloid Interface Sci* **2017**, *502*, 193–200. https://doi.org/10.1016/J.JCIS.2017.05.001.

(7) Caputo, F.; Arnould, A.; Bacia, M.; Ling, W. L.; Rustique, E.; Texier, I.; Mello, A. P.; Couffin, A.-C. Measuring Particle Size Distribution by Asymmetric Flow Field Flow Fractionation: A Powerful Method for Preclinical Characterization of Lipid-Based Nanoparticles. *Mol Pharm* **2019**, *16*, 756–767. https://doi.org/10.1021/acs.molpharmaceut.8b01033.

(8) Adkins, G. B.; Sun, E.; Coreas, R.; Zhong, W. Asymmetrical Flow Field Flow Fractionation Coupled to Nanoparticle Tracking Analysis for Rapid Online Characterization of Nanomaterials. *Anal Chem* **2020**, *92*, 7071–7078. https://doi.org/10.1021/acs.analchem.0c00406.

(9) Schwaferts, C.; Sogne, V.; Welz, R.; Meier, F.; Klein, T.; Niessner, R.; Elsner, M.; Ivleva, N. P. Nanoplastic Analysis by On-Line Coupling of Raman Microscopy and Field-Flow Fractionation Enabled by Optical Tweezers. *Anal Chem* **2020**, *92*, 5813–5820. https://doi.org/10.1021/acs.analchem.9b05336.

(10) Kim, S. T.; Cho, H.-R.; Jung, E. C.; Cha, W.; Baik, M.-H.; Lee, S. Asymmetrical Flow Field-Flow Fractionation Coupled with a Liquid Waveguide Capillary Cell for Monitoring Natural Colloids in Groundwater. *Applied Geochemistry* **2017**, *87*, 102–107. https://doi.org/10.1016/J.APGEOCHEM.2017.10.010.

(11) Schimpf, M. E.; Caldwell, K. D.; Giddings, J. C. *Field Flow Fractionation Handbook*; Wiley: New York, 2000.

(12) Mélin, C.; Perraud, A.; Christou, N.; Bibes, R.; Cardot, P.; Jauberteau, M.-O.; Battu, S.; Mathonnet, M. New Ex-Ovo Colorectal-Cancer Models from Different SdFFF-Sorted Tumor-Initiating Cells. *Anal Bioanal Chem* **2017**, *407*, 8433–8443. https://doi.org/10.1007/s00216-015-9029-z.

(13) Shiri, F.; Petersen, K. E.; Romanov, V.; Zou, Q.; Gale, B. K. Characterization and Differential Retention of Q Beta Bacteriophage Virus-like Particles Using Cyclical Electrical Field – Flow Fractionation and Asymmetrical Flow Field – Flow Fractionation. *Anal Bioanal Chem* **2020**, *412*, 1563–1572.

(14) Naves, T.; Battu, S.; Jauberteau, M.-O.; Cardot, P. J. P.; Ne Ratinaud, M.-H.; Verdier, M. Autophagic Subpopulation Sorting by Sedimentation Field-Flow Fractionation. *Anal Chem* **2012**, *84*, 8748–8755. https://doi.org/10.1021/ac302032v.

(15) Faye, P.-A.; Vedrenne, N.; De La Cruz-Morcillo, M. A.; Cécile Barrot, C.-C.; Richard, L.; Bourthoumieu, S.; Sturtz, F.; Funalot, B.; Lia, A.-S.; Battu, S. New Method for Sorting Endothelial and Neural Progenitors from Human Induced Pluripotent Stem Cells by Sedimentation Field-Flow Fractionation. *Anal Chem* **2016**, *88*, 6696–6702. https://doi.org/10.1021/acs.analchem.6b00704.

(16) Mélin, C.; Perraud, A.; Bounaix Morand du Puch, C.; Loum, E.; Giraud, S.; Cardot, P.; Jauberteau, M.-O.; Lautrette, C.; Battu, S.; Mathonnet, M. Sedimentation Field-Flow Fractionation Monitoring of in Vitro Enrichment in Cancer Stem Cells by Specific Serum-Free Culture Medium. *Journal of Chromatography B* **2014**, *963*, 40–46. https://doi.org/10.1016/j.jchromb.2014.05.039.

(17) Vedrenne, N.; Sarrazy, V.; Battu, S.; Bordeau, N.; Richard, L.; Billet, F.; Coronas, V.; Desmoulière, A. Neural Stem Cell Properties of an Astrocyte Subpopulation Sorted by Sedimentation Field-Flow Fractionation. *Rejuvenation Res* **2016**, *19* (5), 362–372. https://doi.org/10.1089/rej.2015.1776.

(18) Sarrazy, V.; Vedrenne, N.; Bordeau, N.; Billet, F.; Cardot, P.; Desmoulière, A.; Battu, S. Fast Astrocyte Isolation by Sedimentation Field Flow Fractionation. *J Chromatogr A* **2013**, *1289*, 88–93. https://doi.org/10.1016/j.chroma.2013.03.029.

(19) Mélin, C.; Lacroix, A.; Lalloué, F.; Pothier, A.; Zhang, L. Y.; Perraud, A.; Dalmay, C.; Lautrette, C.; Jauberteau, M.-O.; Cardot, P.; Mathonnet, M.; Battu, S. Improved Sedimentation Field-Flow Fractionation Separation Channel for Concentrated Cellular Elution. *J Chromatogr A* **2013**, *1302*, 118–124. https://doi.org/10.1016/j.chroma.2013.05.067.

(20) Ibrahim, T.; Battu, S.; Cook-Moreau, J.; Cardot, P. Instrumentation of Hollow Fiber Flow Field Flow Fractionation for Selective Cell Elution. *Journal of Chromatography B* **2012**, *901*, 59–66. https://doi.org/10.1016/j.jchromb.2012.05.043.

(21) Kinio, S.; Mills, J. K. Localized Electroporation with Dielectrophoretic Field Flow Fractionation: Toward Removal of Circulating Tumour Cells from Human Blood. *IEEE Trans Nanobioscience* **2017**, *16* (8), 802–809. https://doi.org/10.1109/TNB.2017.2764380.

(22) Shamloo, A.; Kamali, A. Numerical Analysis of a Dielectrophoresis Field-Flow Fractionation Device for the Separation of Multiple Cell Types. *J Sep Sci* **2017**, *40*, 4067–4075. https://doi.org/10.1002/jssc.201700325.

(23) Kuklenyik, Z.; Jones, J. I.; Gardner, M. S.; Schieltz, D. M.; Parks, B. A.; Toth, C. A.; Rees, J. C.; Andrews, M. L.; Carter, K.; Lehtikoski, A. K.; McWilliams, L. G.; Williamson, Y. M.; Bierbaum, K. P.; Pirkle, J. L.; Barr, J. R. Core Lipid, Surface Lipid and Apolipoprotein Composition Analysis of Lipoprotein Particles as a Function of Particle Size in One Workflow Integrating Asymmetric Flow Field-Flow Fractionation and Liquid Chromatography-Tandem Mass Spectrometry. *PLoS One* **2018**, *13*, 1–33. https://doi.org/10.1371/journal.pone.0194797.

(24) Lee, J. H.; Yang, J. S.; Lee, S.-H.; Moon, M. H. Analysis of Lipoprotein-Specific Lipids in Patients with Acute Coronary Syndrome by Asymmetrical Flow Field-Flow Fractionation and Nanoflow Liquid Chromatography-Tandem Mass Spectrometry. *Journal of Chromatography B* **2018**, *1099*, 56–63. https://doi.org/10.1016/J.JCHROMB.2018.09.016.

(25) Kim, S. H.; Yang, J. S.; Lee, J. C.; Lee, J.-Y.; Lee, J.-Y.; Kim, E.; Moon, M. H. Lipidomic Alterations in Lipoproteins of Patients with Mild Cognitive Impairment and Alzheimer's Disease by Asymmetrical Flow Field-Flow Fractionation and Nanoflow Ultrahigh Performance Liquid Chromatography-Tandem Mass Spectrometry. *J Chromatogr A* **2018**, *1568*, 91–100. https://doi.org/10.1016/J.CHROMA.2018.07.018.

(26) Lee, K. G.; Lee, G. Bin; Yang, J. S.; Moon, M. H. Perturbations of Lipids and Oxidized Phospholipids in Lipoproteins of Patients with Postmenopausal Osteoporosis Evaluated by Asymmetrical Flow Field-Flow Fractionation and Nanoflow UHPLC – ESI – MS / MS. *Antioxidants* **2020**, *9* (46), 1–14.

(27) Bria, C. R. M.; Afshinnia, F.; Skelly, P. W.; Rajendiran, T. M.; Kayampilly, P.; Thomas, T. P.; Andreev, V. P.; Pennathur, S.; Kim Ratanathanawongs Williams, S. Asymmetrical Flow Field-Flow Fractionation for Improved Characterization of Human Plasma Lipoproteins. *Anal Bioanal Chem* **2019**, *411*, 777–786. https://doi.org/10.1007/s00216-018-1499-3.

(28) Yang, J. S.; Lee, J. C.; Byeon, S. K.; Ho Rha, K.; Moon, M. H. Size Dependent Lipidomic Analysis of Urinary Exosomes from Patients with Prostate Cancer by Flow Field-Flow Fractionation and Nanoflow Liquid Chromatography-Tandem Mass Spectrometry. *Anal Chem* **2017**, *89*, 2488–2496. https://doi.org/10.1021/acs.analchem.6b04634.

(29) Zhang, H.; Freitas, D.; Kim, H. S.; Fabijanic, K.; Li, Z.; Chen, H.; Mark, M. T.; Molina, H.; Martin, A. B.; Bojmar, L.; Fang, J.; Rampersaud, S.; Hoshino, A.; Matei, I.; Kenific, C. M.; Nakajima, M.; Mutvei, A. P.; Sansone, P.; Buehring, W.; Wang, H.; Jimenez, J. P.; Cohen-Gould, L.; Paknejad, N.; Brendel, M.; Manova-Todorova, K.; Magalhães, A.; Ferreira, J. A.; Osório, H.; Silva, A. M.; Massey, A.; Cubillos-Ruiz, J. R.; Galletti, G.; Giannakakou, P.; Cuervo, A. M.; Blenis, J.; Schwartz, R.; Brady, M. S.; Peinado, H.; Bromberg, J.; Matsui, H.; Reis, C. A.; Lyden, D. Identification of Distinct Nanoparticles and Subsets of Extracellular Vesicles by Asymmetric Flow Field-Flow Fractionation. *Nat Cell Biol* **2018**, *20* (3), 332–343. https://doi.org/10.1038/s41556-018-0040-4.

(30) Zhang, H.; Lyden, D. Asymmetric-Flow Field-Flow Fractionation Technology for Exomere and Small Extracellular Vesicle Separation and Characterization. *Nat Protoc* **2019**, *14* (4), 1027–1053. https://doi.org/10.1038/s41596-019-0126-x.

(31) Petersen, K. E.; Shiri, F.; White, T.; Bardi, G. T.; Sant, H.; Gale, B. K.; Hood, J. L. Exosome Isolation: Cyclical Electrical Field Flow Fractionation in Low-Ionic-Strength Fluids. *Anal Chem* **2018**, *90* (21), 12783–12790. https://doi.org/10.1021/acs.analchem.8b03146.

(32) Eskelin, K.; Varjosalo, M.; Ravantti, J.; Mäkinen, K. Ribosome Profiles and Riboproteomes of Healthy and Potato Virus A- and Agrobacterium-Infected Nicotiana Benthamiana Plants. *Mol Plant Pathol* **2019**, *20* (3), 392–409. https://doi.org/10.1111/mpp.12764.

(33) Lampi, M.; Oksanen, H. M.; Meier, F.; Moldenhauer, E.; Poranen, M. M.; Bamford, D. H.; Eskelin, K. Asymmetrical Flow Field-Flow Fractionation in Purification of an Enveloped Bacteriophage Φ6. *Journal of Chromatography B* **2018**, *1095*, 251–257. https://doi.org/10.1016/J.JCHROMB.2018.07.008.

(34) Eskelin, K.; Poranen, M. M.; Oksanen, H. M. Asymmetrical Flow Field-Flow Fractionation on Virus and Virus-like Particle Applications. *Microorganisms* **2019**, *7*, 1–20. https://doi.org/10.3390/microorganisms7110555.

(35) Kondylis, P.; Schlicksup, C. J.; Zlotnick, A.; Jacobson, S. C. Analytical Techniques to Characterize the Structure, Properties, and Assembly of Virus Capsids. *Anal Chem* **2019**, *91*, 622–636. https://doi.org/10.1021/acs.analchem.8b04824.

(36) Lampi, M.; Oksanen, H. M.; Meier, F.; Moldenhauer, E.; Poranen, M. M.; Bamford, D. H.; Eskelin, K. Asymmetrical Flow Field-Flow Fractionation in Purification of an Enveloped Bacteriophage Φ6. *Journal of Chromatography B* **2018**, *1095*, 251–257. https://doi.org/10.1016/j.jchromb.2018.07.008.

(37) Eskelin, K.; Poranen, M. M. Controlled Disassembly and Purification of Functional Viral Subassemblies Using Asymmetrical Flow Field-Flow Fractionation (AF4). *Viruses* **2018**, *10* (579), 1–13. https://doi.org/10.3390/v10110579.

(38) Zhang, M.; Yang, J.; Cai, Z.; Feng, Y.; Wang, Y.; Zhang, D.; Pan, X. Detection of Engineered Nanoparticles in Aquatic Environments: Current Status and Challenges in Enrichment, Separation, and Analysis. *Environ Sci Nano* **2019**, *6*, 709–735. https://doi.org/10.1039/C8EN01086B.

(39) Bolinsson, H.; Lu, Y.; Hall, S.; Nilsson, L.; Håkansson, A. An Alternative Method for Calibration of Flow Field Flow Fractionation Channels for Hydrodynamic Radius Determination: The Nanoemulsion Method (Featuring Multi Angle Light Scattering). *J Chromatogr A* **2018**, *1533*, 155–163. https://doi.org/10.1016/J.CHROMA.2017.12.026.

(40) Mudalige, T. K.; Qu, H.; Van Haute, D.; Ansar, S. M.; Linder, S. W. Capillary Electrophoresis and Asymmetric Flow Field-Flow Fractionation for Size-Based Separation of Engineered Metallic Nanoparticles: A Critical Comparative Review. *Trends in Analytical Chemistry* **2018**, *106*, 202–212. https://doi.org/10.1016/j.trac.2018.07.008.

(41) Baalousha, M.; Stolpe, B.; Lead, J. R. Flow Field-Flow Fractionation for the Analysis and Characterization of Natural Colloids and Manufactured Nanoparticles in Environmental Systems: A Critical Review. *J Chromatogr A* **2011**, *1218* (27), 4078–4103. https://doi.org/10.1016/j.chroma.2011.04.063.

(42) Stone, V.; Nowack, B.; Baun, A.; van den Brink, N.; von der Kammer, F.; Dusinska, M.; Handy, R.; Hankin, S.; Hassellöv, M.; Joner, E.; Fernandes, T. F. Nanomaterials for Environmental Studies: Classification, Reference Material Issues, and Strategies for Physico-Chemical Characterisation. *Science of The Total Environment* **2010**, *408*, 1745–1754. https://doi.org/10.1016/J.SCITOTENV.2009.10.035.

(43) Contado, C. Nanomaterials in Consumer Products: A Challenging Analytical Problem. *Front Chem* **2015**, *3*, 1–20. https://doi.org/10.3389/fchem.2015.00048.

(44) von der Kammer, F.; Legros, S.; Hofmann, T.; Larsen, E. H.; Loeschner, K. Separation and Characterization of Nanoparticles in Complex Food and Environmental Samples by Field-Flow Fractionation. *Trends in Analytical Chemistry* **2011**, *30*, 425–436. https://doi.org/10.1016/j.trac.2010.11.012.

(45) M-M, P.; Siripinyanond, A. Field-Flow Fractionation with Inductively Coupled Plasma Mass Spectrometry: Past, Present, and Future. *J Anal At Spectrom* **2014**, *29*, 1739–1752. https://doi.org/10.1039/C4JA00207E.

(46) Loosli, F.; Wang, J.; Sikder, M.; Afshinnia, K.; Baalousha, M. Analysis of Engineered Nanomaterials ( Ag , CeO2 and Fe 2O3) in Spiked Surface Waters at Environmentally Relevant Particle Concentrations. *Science of the Total Environment* **2020**, *715*, 1–11. https://doi.org/10.1016/j.scitotenv.2020.136927.

(47) Barber, A.; Kly, S.; G., M. M.; Rand, L.; Ranville, J. F. Coupling Single Particle ICP-MS with Field-Flow Fractionation for Characterizing Metal Nanoparticles Contained in Nanoplastic Colloids. *Environ Sci Nano* **2020**, *7*, 514–524.

(48) Mitrano, D. M.; Barber, A.; Bednar, A.; Westerhoff, P.; Higgins, C. P.; Ranville, J. F. Silver Nanoparticle Characterization Using Single Particle ICP-MS (SP-ICP-MS) and Asymmetrical Flow Field Flow Fractionation ICP-MS (AF4-ICP-MS). *J Anal At Spectrom* **2012**, *27*, 1131–1142. https://doi.org/10.1039/c2ja30021d.

(49) Yi, Z.; Loosli, F.; Wang, J.; Berti, D.; Baalousha, M. How to Distinguish Natural versus Engineered Nanomaterials: Insights from the Analysis of TiO2 and CeO2 in Soils. *Environ Chem Lett* **2020**, *18*, 215–227. https://doi.org/10.1007/s10311-019-00926-5.

(50) Smith, W. C.; Morse, J. R.; Bria, C. R. M.; Schaak, R. E.; Williams, S. K. R. Composition-Based Separation of Pt–Fe3O4 Hybrid Nanoparticles by Thermal Field-Flow Fractionation. *ACS Appl Nano Mater* **2018**, *1*, 6435–6443. https://doi.org/10.1021/acsanm.8b01643.

(51) Dou, H.; Kim, B.-J.; Choi, S.-H.; Jung, E. C.; Lee, S. Effect of Size of Fe3O4 Magnetic Nanoparticles on Electrochemical Performance of Screen Printed Electrode Using Sedimentation Field-Flow Fractionation. *Journal of Nanoparticle Research* **2014**, *16*, 2679–2691. https://doi.org/10.1007/s11051-014-2679-5.

(52) Tadjiki, S.; Montaño, M. D.; Assemi, S.; Barber, A.; Ranville, J.; Beckett, R. Measurement of the Density of Engineered Silver Nanoparticles Using Centrifugal FFF-TEM and Single Particle ICP-MS. *Anal Chem* **2017**, *89*, 6056–6064. https://doi.org/10.1021/acs.analchem.7b00652.

(53) Loosli, F.; Yi, Z.; Wang, J.; Baalousha, M. Dispersion of Natural Nanomaterials in Surface Waters for Better Characterization of Their Physicochemical Properties by AF4-ICP-MS-TEM. *Science of The Total Environment* **2019**, *682*, 663–672. https://doi.org/10.1016/J.SCITOTENV.2019.05.206.

(54) López-Sanz, S.; Rodríguez Fariñas, N.; del Carmen Rodríguez Martín-Doimeadios, R.; Ríos, Á. Analytical Strategy Based on Asymmetric Flow Field Flow Fractionation Hyphenated to ICP-MS and Complementary Techniques to Study Gold Nanoparticles Transformations in Cell Culture Medium. *Anal Chim Acta* **2019**, *1053*, 178–185. https://doi.org/10.1016/J.ACA.2018.11.053.

(55) Kim, W.; Bae, J.; Eum, C. H.; Jung, J.; Lee, S. Study on Dispersibility of Thermally Stable Carbon Black Particles in Ink Using Asymmetric Flow Field-Flow Fractionation (AsFlFFF). *Microchemical Journal* **2018**, *142*, 167–174. https://doi.org/10.1016/J.MICROC.2018.06.035.

(56) Herrero, P.; Bäuerlein, P. S.; Emke, E.; Pocurull, E.; de Voogt, P. Asymmetrical Flow Field-Flow Fractionation Hyphenated to Orbitrap High Resolution Mass Spectrometry for the Determination of (Functionalised) Aqueous Fullerene Aggregates. *J Chromatogr A* **2014**, *1356*, 277–282. https://doi.org/10.1016/j.chroma.2014.06.068.

(57) Gigault, J.; El Hadri, H.; Reynaud, S.; Deniau, E.; Grassl, B. Asymmetrical Flow Field Flow Fractionation Methods to Characterize Submicron Particles: Application to Carbon-Based Aggregates and Nanoplastics. *Anal Bioanal Chem* **2017**, *409* (29), 6761–6769. https://doi.org/10.1007/s00216-017-0629-7.

(58) Amaro-Gahete, J.; Benítez, A.; Otero, R.; Esquivel, D.; Jiménez-Sanchidrián, C.; Morales, J.; Caballero, Á.; Romero-Salguero, F. J. A Comparative Study of Particle Size Distribution of Graphene Nanosheets Synthesized by an Ultrasound-Assisted Method. *Nanomaterials* **2019**, *9*, 152–167. https://doi.org/10.3390/nano9020152.

(59) El Hadri, H.; Gigault, J.; Tan, J.; Hackley, V. A. An Assessment of Retention Behavior for Gold Nanorods in Asymmetrical Flow Field-Flow Fractionation. *Anal Bioanal Chem* **2018**, *410*, 6977–6984. https://doi.org/10.1007/s00216-018-1325-y.

(60) Runyon, J. R.; Goering, A.; Yong, K. T.; Williams, S. K. R. Preparation of Narrow Dispersity Gold Nanorods by Asymmetrical Flow Field-Flow Fractionation and Investigation of Surface Plasmon Resonance. *Anal Chem* **2013**, *85*, 940–948. https://doi.org/10.1021/ac302571g.

(61) Chen, M.; Parot, J.; Mukherjee, A.; Couillard, M.; Zou, S.; Hackley, V. A.; Johnston, L. J. Characterization of Size and Aggregation for Cellulose Nanocrystal Dispersions Separated by Asymmetrical-Flow Field-Flow Fractionation. *Cellulose* **2020**, *27* (4), 2015–2028. https://doi.org/10.1007/s10570-019-02909-9.

(62) Saenmuangchin, R.; Siripinyanond, A. Flow Field-Flow Fractionation for Hydrodynamic Diameter Estimation of Gold Nanoparticles with Various Types of Surface Coatings. *Anal Bioanal Chem* **2018**, *410*, 6845–6859. https://doi.org/10.1007/s00216-018-1284-3.

(63) Schwaferts, C.; Niessner, R.; Elsner, M.; Ivleva, N. P. Methods for the Analysis of Submicrometer- and Nanoplastic Particles in the Environment. *Trends in Analytical Chemistry* **2019**, *112*, 52–65. https://doi.org/10.1016/J.TRAC.2018.12.014.

(64) Correia, M.; Loeschner, K. Detection of Nanoplastics in Food by Asymmetric Flow Field-Flow Fractionation Coupled to Multi-Angle Light Scattering: Possibilities, Challenges and Analytical Limitations. *Anal Bioanal Chem* **2018**, *410* (22), 5603–5615. https://doi.org/10.1007/s00216-018-0919-8.

(65) Qu, H.; Quevedo, I. R.; Linder, S. W.; Fong, A.; Mudalige, T. K. Importance of Material Matching in the Calibration of Asymmetric Flow Field-Flow Fractionation: Material Specificity and Nanoparticle Surface Coating Effects on Retention Time. *Journal of Nanoparticle Research* **2016**, *18*, 292–302. https://doi.org/10.1007/s11051-016-3601-0.

(66) Gigault, J.; Hackley, V. A. Observation of Size-Independent Effects in Nanoparticle Retention Behavior during Asymmetric-Flow Field-Flow Fractionation. *Anal Bioanal Chem* **2013**, *405* (19), 6251–6258. https://doi.org/10.1007/s00216-013-7055-2.

(67) Noskov, S.; Scherer, C.; Maskos, M. Determination of Hamaker Constants of Polymeric Nanoparticles in Organic Solvents by Asymmetrical Flow Field-Flow Fractionation. *J Chromatogr A* **2013**, *1274*, 151–158. https://doi.org/10.1016/j.chroma.2012.12.001.

(68) Zhang, X.; Li, Y.; Shen, S.; Lee, S.; Dou, H. Field-Flow Fractionation: A Gentle Separation and Characterization Technique in Biomedicine. *Trends in Analytical Chemistry* **2018**, *108*, 231–238. https://doi.org/10.1016/J.TRAC.2018.09.005.

(69) Zattoni, A.; Roda, B.; Borghi, F.; Marassi, V.; Reschiglian, P. Flow Field-Flow Fractionation for the Analysis of Nanoparticles Used in Drug Delivery. *J Pharm Biomed Anal* **2014**, *87*, 53–61. https://doi.org/10.1016/j.jpba.2013.08.018.

(70) Wagner, M.; Holzschuh, S.; Traeger, A.; Fahr, A.; Schubert, Ulrich. S. Asymmetric Flow Field-Flow Fractionation in the Field of Nanomedicine. *Anal Chem* **2014**, *86*, 5201–5210. https://doi.org/10.1021/ac501664t.

(71) Caputo, F.; Clogston, J.; Calzolai, L.; Rösslein, M.; Prina-Mello, A. Measuring Particle Size Distribution of Nanoparticle Enabled Medicinal Products, the Joint View of EUNCL and NCI-NCL. A Step by Step Approach Combining Orthogonal Measurements with Increasing Complexity. *Journal of Controlled Release* **2019**, *299*, 31–43. https://doi.org/10.1016/J.JCONREL.2019.02.030.

(72) Elvang, P. A.; Stein, P. C.; Bauer-Brandl, A.; Brandl, M. Characterization of Co-Existing Colloidal Structures in Fasted State Simulated Fluids FaSSIF: A Comparative Study Using AF4/MALLS, DLS and DOSY. *J Pharm Biomed Anal* **2017**, *145*, 531–536. https://doi.org/10.1016/J.JPBA.2017.07.014.

(73) Engel, A.; Plöger, M.; Mulac, D.; Langer, K. Asymmetric Flow Field-Flow Fractionation (AF4) for the Quantification of Nanoparticle Release from Tablets during Dissolution

Testing. *Int J Pharm* **2014**, *461*, 137–144. https://doi.org/10.1016/J.IJPHARM.2013.11.044.

(74) Contado, C.; Vighi, E.; Dalpiaz, A.; Leo, E. Influence of Secondary Preparative Parameters and Aging Effects on PLGA Particle Size Distribution: A Sedimentation Field Flow Fractionation Investigation. *Anal Bioanal Chem* **2013**, *405*, 703–711. https://doi.org/10.1007/s00216-012-6113-5.

(75) Wagner, M.; Barthel, M. J.; Freund, R. R. A.; Hoeppener, S.; Traeger, A.; Schacher, F. H.; Schubert, U. S. Solution Self-Assembly of Poly(Ethylene Oxide)-Block-Poly(Furfuryl Glycidyl Ether)-Block-Poly(Allyl Glycidyl Ether) Based Triblock Terpolymers: A Field-Flow Fractionation Study. *Polym Chem* **2014**, *5* (24), 6943–6956. https://doi.org/10.1039/C4PY00863D.

(76) Boye, S.; Appelhans, D.; Boyko, V.; Zschoche, S.; Komber, H.; Friedel, P.; Formanek, P.; Janke, A.; Voit, B. I.; Lederer, A. PH-Triggered Aggregate Shape of Different Generations Lysine-Dendronized Maleimide Copolymers with Maltose Shell. *Biomacromolecules* **2012**, *13* (12), 4222–4235. https://doi.org/10.1021/bm301489s.

(77) Pound-Lana, G. E. N.; Garcia, G. M.; Trindade, I. C.; Capelari-Oliveira, P.; Pontifice, T. G.; Vilela, J. M. C.; Andrade, M. S.; Nottelet, B.; Postacchini, B. B.; Mosqueira, V. C. F. Phthalocyanine Photosensitizer in Polyethylene Glycol-Block-Poly(Lactide-Co-Benzyl Glycidyl Ether) Nanocarriers: Probing the Contribution of Aromatic Donor-Acceptor Interactions in Polymeric Nanospheres. *Materials Science and Engineering C* **2019**, *94*, 220–233. https://doi.org/10.1016/J.MSEC.2018.09.022.

(78) Miwa, S.; Takahashi, R.; Rössel, C.; Matsumoto, S.; Fujii, S.; Lee, J. H.; Schacher, F. H.; Sakurai, K. Core–Shell–Corona Micelles from a Polyether-Based Triblock Terpolymer: Investigation of the PH-Dependent Micellar Structure. *Langmuir* **2018**, *34* (26), 7813–7820. https://doi.org/10.1021/acs.langmuir.8b01168.

(79) Till, U.; Gaucher-Delmas, M.; Saint-Aguet, P.; Hamon, G.; Marty, J.-D.; Chassenieux, C.; Payré, B.; Goudounèche, D.; Mingotaud, A.-F.; Violleau, F. Asymmetrical Flow Field-Flow Fractionation with Multi-Angle Light Scattering and Quasi-Elastic Light Scattering for Characterization of Polymersomes: Comparison with Classical Techniques. *Analytica and Bioanalytical Chemistry* **2014**, *406* (30), 7841–7853. https://doi.org/10.1007/s00216-014-7891-8.

(80) Deodhar, G. V.; Adams, M. L.; Joardar, S.; Joglekar, M.; Davidson, M.; Smith, W. C.; Mettler, M.; Toler, S. A.; Davies, F. K.; Williams, S. K. R.; Trewyn, B. G. Conserved Activity of Reassociated Homotetrameric Protein Subunits Released from Mesoporous Silica Nanoparticles. *Langmuir* **2018**, *34* (1), 228–233. https://doi.org/10.1021/acs.langmuir.7b03310.

(81) Roda, B.; Marassi, V.; Zattoni, A.; Borghi, F.; Anand, R.; Agostoni, V.; Gref, R.; Reschiglian, P.; Monti, S. Flow Field-Flow Fractionation and Multi-Angle Light Scattering as a Powerful Tool for the Characterization and Stability Evaluation of Drug-Loaded Metal–Organic Framework Nanoparticles. *Anal Bioanal Chem* **2018**, *410*, 5245–5253. https://doi.org/10.1007/s00216-018-1176-6.

(82) Khosa, A.; Reddi, S.; Saha, R. N. Nanostructured Lipid Carriers for Site-Specific Drug Delivery. *Biomedicine & Pharmacotherapy* **2018**, *103*, 598–613. https://doi.org/10.1016/J.BIOPHA.2018.04.055.

(83) Qu, H.; Wang, J.; Wu, Y.; Zheng, J.; Krishnaiah, Y. S. R.; Absar, M.; Choi, S.; Ashraf, M.; Cruz, C. N.; Xu, X. Asymmetric Flow Field Flow Fractionation for the Characterization of Globule Size Distribution in Complex Formulations: A Cyclosporine Ophthalmic Emulsion Case. *Int J Pharm* **2018**, *538*, 215–222. https://doi.org/10.1016/J.IJPHARM.2018.01.012.

(84) Elvang, P. A.; Hinna, A. H.; Brouwers, J.; Hens, B.; Augustijns, P.; Brandl, M. Bile Salt Micelles and Phospholipid Vesicles Present in Simulated and Human Intestinal Fluids: Structural Analysis by Flow Field-Flow Fractionation/Multiangle Laser Light Scattering. *J Pharm Sci* **2016**, *105* (9), 2832–2839. https://doi.org/10.1016/J.XPHS.2016.03.005.

(85) Till, U.; Gaucher, M.; Amouroux, B.; Gineste, S.; Lonetti, B.; Marty, J. D.; Mingotaud, C.; Bria, C. R. M.; Williams, S. K. R.; Violleau, F.; Mingotaud, A. F. Frit Inlet Field-Flow Fractionation Techniques for the Characterization of Polyion Complex Self-Assemblies. *J Chromatogr A* **2017**, *1481*, 101–110. https://doi.org/10.1016/j.chroma.2016.12.050.

(86) Parot, J.; Caputo, F.; Mehn, D.; Hackley, V. A.; Calzolai, L. Physical Characterization of Liposomal Drug Formulations Using Multi-Detector Asymmetrical-Flow Field Flow Fractionation. *Journal of Controlled Release* **2020**, *320*, 495–510. https://doi.org/10.1016/j.jconrel.2020.01.049.

(87) Hu, Y.; Crist, R. M.; Clogston, J. D. The Utility of Asymmetric Flow Field-Flow Fractionation for Preclinical Characterization of Nanomedicines. *Anal Bioanal Chem* **2020**, *512*, 425–438.

(88) Ashby, J.; Schachermeyer, S.; Duan, Y.; Jimenez, L. A.; Zhong, W. Probing and Quantifying DNA-Protein Interactions with Asymmetrical Flow Field-Flow Fractionation. *J Chromatogr A* **2014**, *1358*, 217–224. https://doi.org/10.1016/j.chroma.2014.07.002.

(89) Pollastrini, J.; Dillon, T. M.; Bondarenko, P.; Chou, R. Y. T. Field Flow Fractionation for Assessing Neonatal Fc Receptor and Fcγ Receptor Binding to Monoclonal Antibodies in Solution. *Anal Biochem* **2011**, *414*, 88–98. https://doi.org/10.1016/j.ab.2011.03.001.

(90) Bria, C. R. M.; Jones, J.; Charlesworth, A.; Ratanathanawongs Williams, S. K. Probing Submicron Aggregation Kinetics of an IgG Protein by Asymmetrical Flow Field-Flow Fractionation. *J Pharm Sci* **2016**, *105* (1), 31–39. https://doi.org/10.1002/jps.24703.

(91) Ma, D.; Martin, N.; Tribet, C.; Winnik, F. M. Quantitative Characterization by Asymmetrical Flow Field-Flow Fractionation of IgG Thermal Aggregation with and without Polymer Protective Agents. *Analytica and Bioanalytical Chemistry* **2014**, *406*, 7539–7547. https://doi.org/10.1007/s00216-014-8200-2.

(92) Leeman, M.; Choi, J.; Hansson, S.; Storm, M. U.; Nilsson, L. Proteins and Antibodies in Serum, Plasma, and Whole Blood—Size Characterization Using Asymmetrical Flow Field-Flow Fractionation (AF4). *Anal Bioanal Chem* **2018**, *410* (20), 4867–4873. https://doi.org/10.1007/s00216-018-1127-2.

(93) Bria, C. R. M.; Williams, S. K. R. Impact of Asymmetrical Flow Field-Flow Fractionation on Protein Aggregates Stability. *J Chromatogr A* **2016**, *1465*, 155–164. https://doi.org/10.1016/j.chroma.2016.08.037.

(94) Boll, B.; Josse, L.; Heubach, A.; Hochenauer, S.; Finkler, C.; Huwyler, J.; Koulov, A. V. Impact of Non-Ideal Analyte Behavior on the Separation of Protein Aggregates by Asymmetric Flow Field-Flow Fractionation. *J Sep Sci* **2018**, *41* (13), 2854–2864. https://doi.org/10.1002/jssc.201701457.

(95) Caracciolo, G.; Farokhzad, O. C.; Mahmoudi, M. Biological Identity of Nanoparticles in Vivo: Clinical Implications of the Protein Corona. *Trends Biotechnol* **2017**, *35*, 257–264. https://doi.org/10.1016/j.tibtech.2016.08.011.

(96) Ojea-Jiménez, I.; Capomaccio, R.; Osório, I.; Mehn, D.; Ceccone, G.; Hussain, R.; Siligardi, G.; Colpo, P.; Rossi, F.; Gilliland, D.; Calzolai, L. Rational Design of Multi-Functional Gold Nanoparticles with Controlled Biomolecule Adsorption: A Multi-Method Approach for in-Depth Characterization. *Nanoscale* **2018**, *10* (21), 10173–10181. https://doi.org/10.1039/C8NR00973B.

(97) Safenkova, I. V.; Slutskaya, E. S.; Panferov, V. G.; Zherdev, A. V.; Dzantiev, B. B. Complex Analysis of Concentrated Antibody-Gold Nanoparticle Conjugates' Mixtures Using Asymmetric Flow Field-Flow Fractionation. *J Chromatogr A* **2016**, *1477*, 56–63. https://doi.org/10.1016/J.CHROMA.2016.11.040.

(98) Bouzas-Ramos, D.; García-Alonso, J. I.; Costa-Fernández, J. M.; Ruiz Encinar, J. Quantitative Assessment of Individual Populations Present in Nanoparticle–Antibody Conjugate Mixtures Using AF4-ICP-MS/MS. *Anal Chem* **2019**, *91* (5), 3567–3574. https://doi.org/10.1021/acs.analchem.8b05482.

(99) Ferreira, H. S.; Moreira-Alvarez, B.; Montoro Bustos, A. R.; Encinar, J. R.; Costa-Fernández, J. M.; Sanz-Medel, A. Capabilities of Asymmetrical Flow Field – Flow Fractionation on-Line Coupled to Different Detectors for Characterization of Water-Stabilized Quantum Dots Bioconjugated to Biomolecules. *Talanta* **2020**, *206*, 120228–120236. https://doi.org/10.1016/j.talanta.2019.120228.

(100) Niezabitowska, E.; Smith, J.; Prestly, M. R.; Akhtar, R.; von Aulock, F. W.; Lavallée, Y.; Ali-Boucetta, H.; McDonald, T. O. Facile Production of Nanocomposites of Carbon Nanotubes and Polycaprolactone with High Aspect Ratios with Potential Applications in Drug Delivery. *RSC Adv* **2018**, *8* (30), 16444–16454. https://doi.org/10.1039/C7RA13553J.

(101) Contado, C.; Mehn, D.; Gilliland, D.; Calzolai, L. Characterization Methods for Studying Protein Adsorption on Nano-Polystyrene Beads. *J Chromatogr A* **2019**, *1606*, 460383–460394. https://doi.org/10.1016/J.CHROMA.2019.460383.

(102) Ashby, J.; Schachermeyer, S.; Pan, S.; Zhong, W. Dissociation-Based Screening of Nanoparticle‒protein Interaction via Flow Field-Flow Fractionation. *Anal Chem* **2013**, *85*, 7494–7501. https://doi.org/10.1021/ac401485j.

(103) Weber, C.; Simon, J.; Mailänder, V.; Morsbach, S.; Landfester, K. Preservation of the Soft Protein Corona in Distinct Flow Allows Identification of Weakly Bound Proteins. *Acta Biomater* **2018**, *76*, 217–224. https://doi.org/10.1016/J.ACTBIO.2018.05.057.

(104) Boye, S.; Ennen, F.; Scharfenberg, L.; Appelhans, D.; Nilsson, L.; Lederer, A. From 1D Rods to 3D Networks: A Biohybrid Topological Diversity Investigated by Asymmetrical Flow Field-Flow Fractionation. *Macromolecules* **2015**, *48*, 4607–4619. https://doi.org/10.1021/acs.macromol.5b00824.

(105) Till, U.; Gibot, L.; Mingotaud, C.; Vicendo, P.; Rols, M.-P.; Gaucher, M.; Violleau, F.; Mingotaud, A.-F. Self-Assembled Polymeric Vectors Mixtures: Characterization of the Polymorphism and Existence of Synergistic Effects in Photodynamic Therapy. *Nanotechnology* **2016**, *27*, 315102–315112. https://doi.org/10.1088/0957-4484/27/31/315102.

(106) Till, U.; Gaucher, M.; Amouroux, B.; Gineste, S.; Lonetti, B.; Marty, J. D.; Mingotaud, C.; Bria, C. R. M.; Williams, S. K. R.; Violleau, F.; Mingotaud, A. F. Frit Inlet Field-Flow Fractionation Techniques for the Characterization of Polyion Complex Self-Assemblies. *J Chromatogr A* **2017**, *1481*, 101–110. https://doi.org/10.1016/j.chroma.2016.12.050.

(107) Fuentes, C.; Choi, J.; Zielke, C.; Peñarrieta, J. M.; Lee, S.; Nilsson, L. Comparison between Conventional and Frit-Inlet Channel in Separation of Biopolymers by Asymmetric Flow Field-Flow Fractionation. *Analyst* **2019**, *144*, 4559–4568. https://doi.org/10.1039/C9AN00466A.

(108) Bria, C. R. M.; Skelly, P. W.; Morse, J. R.; Schaak, R. E.; Williams, S. K. R. Semi-Preparative Asymmetrical Flow Field-Flow Fractionation: A Closer Look at Channel Dimensions and Separation Performance. *J Chromatogr A* **2017**, *1499*, 149–157. https://doi.org/10.1016/j.chroma.2017.03.017.

(109) Marioli, M.; Kavurt, B.; Stamatialis, D.; Kok, W. T. Application of Microstructured Membranes for Increasing Retention, Selectivity and Resolution in Asymmetrical Flow Field-Flow Fractionation. *J Chromatogr A* **2019**, *1605*, 360347–360356. https://doi.org/10.1016/j.chroma.2019.07.001.

(110) Marioli, M.; Kok, W. T. Continuous Asymmetrical Flow Field-Flow Fractionation for the Purification of Proteins and Nanoparticles. *Sep Purif Technol* **2020**, *242*, 116744–116753. https://doi.org/10.1016/j.seppur.2020.116744.

(111) Tan, P.; Yang, J.; Nischwitz, V. A Novel Approach for Determination of the Dissolved and the Particulate Fractions in Aqueous Samples by Flow Field Flow Fractionation via Online Monitoring of Both the Cross Flow and the Detector Flow Using ICP-MS. *J Anal At Spectrom* **2020**, *35*, 548–559. https://doi.org/10.1039/c9ja00313d.

(112) Cuss, C. W.; Grant-Weaver, I.; Shotyk, W. AF4-ICPMS with the 300 Da Membrane to Resolve Metal-Bearing "Colloids" < 1 KDa: Optimization, Fractogram Deconvolution, and Advanced Quality Control. *Anal Chem* **2017**, *89*, 8027–8035. https://doi.org/10.1021/acs.analchem.7b01427.

(113) Mitrano, D. M.; Barber, A.; Bednar, A.; Westerhoff, P.; Higgins, C. P.; Ranville, J. F. Silver Nanoparticle Characterization Using Single Particle ICP-MS (SP-ICP-MS) and

Asymmetrical Flow Field Flow Fractionation ICP-MS (AF4-ICP-MS). *J Anal At Spectrom* **2012**, *27* (7), 1131–1142. https://doi.org/10.1039/c2ja30021d.

(114) Huclier-Markai, S.; Grivaud-Le Du, A.; N'tsiba, E.; Montavon, G.; Mougin-Degraef, M.; Barbet, J. Coupling a Gamma-Ray Detector with Asymmetrical Flow Field Flow Fractionation (AF4): Application to a Drug-Delivery System for Alpha-Therapy. *J Chromatogr A* **2018**, *1573*, 107–114. https://doi.org/10.1016/J.CHROMA.2018.08.065.

(115) Maguire, C. M.; Rösslein, M.; Wick, P.; Prina-Mello, A. Characterisation of Particles in Solution – a Perspective on Light Scattering and Comparative Technologies. *Sci Technol Adv Mater* **2018**, *19* (1), 732–745. https://doi.org/10.1080/14686996.2018.1517587.

(116) Hu, Z.; Ye, C.; Mi, W.; Zhao, Y.; Quan, C.; Li, W. W.; Li, H.; Hang, H. Light-Scattering Detection within the Difficult Size Range of Protein Particle Measurement Using Flow Cytometry. *Nanoscale* **2018**, *10* (41), 19277–19285. https://doi.org/10.1039/C8NR05214J.

(117) Sitar, S.; Kejž, A.; Pahovnik, D.; Kogej, K.; Tuš Ek-Z, M.; Nidarič, ˇ; Lenassi, M.; Agar, E. Z. ˇ. Size Characterization and Quantification of Exosomes by Asymmetrical-Flow Field-Flow Fractionation. *Anal Chem* **2015**, *87*, 9225–9233. https://doi.org/10.1021/acs.analchem.5b01636.

(118) Kato, H.; Nakamura, A.; Banno, H. Determination of Number-Based Size Distribution of Silica Particles Using Centrifugal Field-Flow Fractionation. *J Chromatogr A* **2019**, *1602*, 409–418. https://doi.org/10.1016/j.chroma.2019.05.055.

(119) Hwang, J. Y.; Youn, S.; Yang, I.-H. Gravitational Field Flow Fractionation: Enhancing the Resolution Power by Using an Acoustic Force Field. *Anal Chim Acta* **2019**, *1047*, 238–247. https://doi.org/10.1016/J.ACA.2018.09.056.

(120) Johann, C.; Elsenberg, S.; Schuch, H.; Rösch, U. Instrument and Method to Determine the Electrophoretic Mobility of Nanoparticles and Proteins by Combining Electrical and Flow Field-Flow Fractionation. *Anal Chem* **2015**, *87* (8), 4292–4298. https://doi.org/10.1021/ac504712n.

(121) Gigault, J.; Pettibone, J. M.; Schmitt, C.; Hackley, V. A. Rational Strategy for Characterization of Nanoscale Particles by Asymmetric-Flow Field Flow Fractionation: A Tutorial. *Anal Chim Acta* **2014**, *809*, 9–24. https://doi.org/10.1016/j.aca.2013.11.021.

(122) *Nanotechnologies-Analysis of Nano-Objects Using Asymmetrical-Flow and Centrifugal Field-Flow Fractionation*; International Organization for Standardization, ISO/TS 21362:2018(E) Geneva, Switzerland, 2018.

(123) Wahlund, K.-G. Flow Field-Flow Fractionation: Critical Overview. *J Chromatogr A* **2013**, *1287*, 97–112. https://doi.org/10.1016/j.chroma.2013.02.028.

(124) Håkansson, A.; Magnusson, E.; Bergenståhl, B.; Nilsson, L. Hydrodynamic Radius Determination with Asymmetrical Flow Field-Flow Fractionation Using Decaying Cross-Flows. Part I. A Theoretical Approach. *J Chromatogr A* **2012**, *1253*, 120–126. https://doi.org/10.1016/J.CHROMA.2012.07.029.

(125) Magnusson, E.; Håkansson, A.; Janiak, J.; Bergenståhl, B.; Nilsson, L. Hydrodynamic Radius Determination with Asymmetrical Flow Field-Flow Fractionation Using Decaying

Cross-Flows. Part II. Experimental Evaluation. *J Chromatogr A* **2012**, *1253*, 127–133. https://doi.org/10.1016/J.CHROMA.2012.07.005.

(126) Williams, P. S. Fractionating Power and Outlet Stream Polydispersity in Asymmetrical Flow Field-Flow Fractionation. Part I: Isocratic Operation. *Anal Bioanal Chem* **2016**, *408* (12), 3247–3263. https://doi.org/10.1007/s00216-016-9388-0.

(127) Williams, P. S. Fractionating Power and Outlet Stream Polydispersity in Asymmetrical Flow Field-Flow Fractionation. Part II: Programmed Operation. *Anal Bioanal Chem* **2017**, *409*, 317–334. https://doi.org/10.1007/s00216-016-0007-x.

(128) Wang, J.-L.; Alasonati, E.; Fisicaro, P.; Benedetti, M. F.; Martin, M. Theoretical and Experimental Investigation of the Focusing Position in Asymmetrical Flow Field-Flow Fractionation (AF4). *J Chromatogr A* **2018**, *1561*, 67–75. https://doi.org/10.1016/J.CHROMA.2018.04.056.

(129) Dou, H.; Lee, Y. J.; Jung, E. C.; Lee, B. C.; Lee, S. Study on Steric Transition in Asymmetrical Flow Field-Flow Fractionation and Application to Characterization of High-Energy Material. *J Chromatogr A* **2013**, *1304*, 211–219. https://doi.org/10.1016/j.chroma.2013.06.051.

(130) Dou, H.; Jung, E. C.; Lee, S. Factors Affecting Measurement of Channel Thickness in Asymmetrical Flow Field-Flow Fractionation. *J Chromatogr A* **2015**, *1393*, 115–121. https://doi.org/10.1016/J.CHROMA.2015.03.025.

(131) Mudalige, T. K.; Qu, H.; Linder, S. W. Rejection of Commonly Used Electrolytes in Asymmetric Flow Field Flow Fractionation: Effects of Membrane Molecular Weight Cutoff Size, Fluid Dynamics, and Valence of Electrolytes. *Langmuir* **2017**, *33* (6), 1442–1450. https://doi.org/10.1021/acs.langmuir.6b03749.

(132) Jochem, A.-R.; Ankah, G. N.; Meyer, L.-A.; Elsenberg, S.; Johann, C.; Kraus, T. Colloidal Mechanism of Gold Mechanisms of Gold Nanoparticle Loss in Asymmetric Flow Field-Flow Fractionation. *Anal Chem* **2016**, *88* (20), 10065–10073. https://doi.org/10.1021/acs.analchem.6b02397.

(133) Williams, S. K. R.; Caldwell, K. D. *Field-Flow Fractionation in Biopolymer Analysis*; Springer-Verlag/Wien: Verlag/Wien, 2012.

(134) Kato, H.; Nakamura, A.; Banno, H.; Shimizu, M. Separation of Different-Sized Silica Nanoparticles Using Asymmetric Flow Field-Flow Fractionation by Control of the Debye Length of the Particles with the Addition of Electrolyte Molecules. *Colloids and Surfaces A* **2018**, *538*, 678–685. https://doi.org/10.1016/J.COLSURFA.2017.11.067.

(135) Geisler, M.; Lederer, A. Non-Parabolicity Correction for Fifty-Nine Solvents and a Retention Study for Strongly Distorted Flow-Profiles in Thermal Field-Flow Fractionation. *J Chromatogr A* **2020**, *1621*, 461082–461090. https://doi.org/10.1016/j.chroma.2020.461082.

(136) Sitar, S.; Vezočnik, V.; Maček, P.; Kogej, K.; Pahovnik, D.; Žagar, E. Pitfalls in Size Characterization of Soft Particles by Dynamic Light Scattering Online Coupled to

Asymmetrical Flow Field-Flow Fractionation. *Anal Chem* **2017**, *89* (21), 11744–11752. https://doi.org/10.1021/acs.analchem.7b03251.

(137) Wyatt, P. J. Measurement of Special Nanoparticle Structures by Light Scattering. *Anal Chem* **2014**, *86* (15), 7171–7183. https://doi.org/10.1021/ac500185w.

CHAPTER 4

# ENUMERATION OF BIOLOGICAL PARTICLES SEPARATED AND ANALYZED BY AF4-MALS: DEPENDENCIES ON LIGHT SCATTERING MODEL AND REFRACTIVE INDEX

Prepared for submission to *Analytical Chemistry*

Christine L. Plavchak[1], Allision Z. Werner[2], Elizabeth Betz[1], Davinia Salvachúa[2], Gregg T. Beckham[2], and S. Kim Ratanathanawongs Williams[1]

## 4.1 Abstract

Determining accurate counts and size distributions for biological particles (bioparticles) is crucial in wide-ranging fields, but current ensemble methods to this end are susceptible to bias from polydispersity in size. Particle separation can mitigate bias and lead to more accurate particle sizing, but the impact of light scatting models and refractive indices (RI) on multiangle light scattering (MALS)-derived biological particle counts is still not well understood. Here, we develop an analysis workflow using asymmetrical flow field-flow fractionation (AF4) with on-line MALS to simultaneously separate and provide particles sizes and counts, respectively. The effect of particle counting theory or models and RI on particle counts and size distributions are systematically assessed for both polystyrene latex (PSL) particles ($d_h$ = 20-496 nm) and bacterial outer membrane vesicles (OMVs, $d_h$ = 20-438 nm). Across spherical models, PSL particle counts vary up to 13 %. For the coated-sphere model used in the analysis of OMV samples, the sphere RI value greatly impacts particle counts: as the sphere RI value approaches the RI of the suspending medium, the model becomes more sensitive to the acquired light scattering signal ultimately causing erroneous particle counts. Overall, this work establishes the importance of

[1] Laboratory for Advanced Separations Technologies, Department of Chemistry, Colorado School of Mines, Golden, Colorado, 80401, USA
[2] Renewable Resources and Enabling Sciences Center, National Renewable Energy Laboratory, Golden, Colorado, 80401, USA

selecting appropriate models and RI values for bioparticles to obtain accurate counts, and provides a validated AF4-MALS method for the separation, enumeration, and sizing of polydisperse bioparticles.

## 4.2 Introduction

Outer membrane vesicles (OMVs) are nanometer-sized lipid particles (25-500 nm) that are produced from the outer membrane of Gram-negative bacteria and play various roles in biotechnology. OMVs are of interest for vaccine development due to their enrichment of bioactive proteins, toxins, virulence factors and immunogenic materials to stimulate host-bacteria interactions.[1] More recently they have been explored to coat nanoparticles (NPs) to promote a more biomimetic approach with NPs, helping preserve NP functionality while enhancing the functions of OMVs.[2] Beyond their medical applications, they have shown potential in the biomass conversion community where certain strains of bacteria have shown to have a particular affinity for aromatic catabolism[3].

In addition to their vast applications, understanding OMV cargo composition and biogenesis has been of importance since the discovery of OMVs in the 1965.[4] Two of the main challenges with the OMV characterization is centered around understanding OMV biogenesis and functionality and uncovering potential size-dependencies with their cargo load.[5] Typically, OMV composition consists of a ratio of different lipoproteins, phospholipids, and proteins.[6] Along their complex composition, their polydispersity in size makes it difficult to probe potential size-dependent cargo unless rigorously measured through biochemical and analytical techniques. Correlating how particle size and number relate to OMV cargo can lead to a better understanding of efficiency per OMV particle and aid in normalizing protein content.

Despite bioparticles like OMVs being measured using a variety of methodologies, there still lacks a standalone technique for accurately sizing and counting nanoparticles.[7] Current ensemble methods used for bioparticle counting include tunable resistive-pulse sensing (TRPS)[8], Coulter counter (CC)[9], dynamic light scattering (DLS)[10], flow cytometry (FC)[7], nanoparticle tracking analysis (NTA)[11], and multiangle light scattering (MALS).[12] However, ensemble methods such as these only provide averages and do not deliver information regarding size distributions within the sample. Further, TRPS, CC, and FC are not sensitive enough to analyze small particles (e.g., < 30 nm in diameter) and all methods except for FC often cannot accommodate large particle size distributions within a sample set (e.g., 20-500 nm). The latter is because of either instrumental constraints (e.g., needing multiple apertures (CC), buildup of particles around tunable pores (TRPS), or camera sensitivities (NTA)) or larger particles impacting average values or signal intensity (MALS).

Particle separation can mitigate ensemble biases by creation of more monodisperse subpopulations prior to sizing and quantifying. Two of the techniques mentioned previously, NTA and MALS, have been coupled to separation mechanisms like size exclusion chromatography (SEC) and asymmetrical flow field-flow fractionation (AF4).[13,14] NTA estimates particle size and count by optically tracking the Brownian motion of particles in solution; however, the results of NTA measurements are often influenced by instrumental parameters.[15,16] MALS fits the light scattering intensity from all regions of a particle to light scattering formalisms or shape-specific models to obtain size and count information yet using incorrect models or formalisms may introduce significant errors overall values.[17]

MALS has gained traction over the past 20 years as it is commercially available with most SEC and FFF systems, and has been shown to effectively quantify bioparticles such as virus-like particles and lipid-based nanocarriers.[12,18,19] Comparisons between NTA and MALS techniques has led to a better understanding of methodological robustness and accuracy,[14,20] including by utilizing AF4-MALS to separate and size extracellular vesicles.[21–23] However, the influence of analyte-dependent parameters (e.g., particle size, refractive index, and light scattering model) during sample analysis raises concern about the accuracy of MALS particle counting, yet the impact(s) of these parameters on particle counts have yet to be systematically studied.

To address this knowledge gap, an analytical AF4-MALS method was developed and the effect of counting model and refractive index on particle counts was systematically evaluated for both polystyrene latex (PSL) standards and bacterial outer membrane vesicles (OMVs). OMVs were chosen as an exemplary bioparticle for this study as they are polydisperse (e.g., 25 to 500 nm[24–26]) and the composition varies based on ratios of lipoproteins, phospholipids and proteins,[6] all of which affect RI. The AF4-MALS method we present provides simultaneous size-based separation and enumeration of PSL standards and OMVs. We found MALS particle counts of PSL standards vary up to 13% based on the selection of light scattering models. Further, we systematically examine the effect of RI values determined from varying lipoprotein:phospholipid:protein ratios in conjunction with light scattering model, and find this to affect particle counts by up to 200%. Overall, this study provides foundational knowledge necessary to acquire accurate bioparticle counts via MALS, and presents a validated AF4-MALS method for the separation and enumeration of bioparticles such as bacterial OMVs.

### 4.3 MALS Particle Counting Theory

The basic principles of particle counting using light scattering was examined in the 1960s using Mie scattering theory.[27] Since then, there has been adaptations and assumptions made to determine particle counts using the Rayleigh-Gans-Debye (RGD) approximation.[28] Based on each theory, there are subtle differences in the particle counting theories and it is important to understand the assumptions for data analysis and interpretation.

### 4.3.1 Mie Scattering Theory

It is understood that there is an angular dependence on size determination through MALS.[17] The intensity of scattered light from a spherical particle for measurements made in the θ plane with incident light polarized perpendicularly and at some known angle can be represented as

$$I_{\theta S} = \frac{I_o N \Delta v}{(kr)^2} i(\theta) \tag{4.1}$$

where $N$ is the total number of particles/mL, $\Delta v$ is a pre-determined scattering volume, $k = 2\pi n_o / \lambda_o$ where $n_o$ is the refractive index of the solvent and $\lambda_o$ is the wavelength of the laser, $r$ is the length to the detector, and $i(\theta)$ is the differential intensity or single particle scattering function (Eq. 4.2). The most important analyte-dependent parameters in this equation are the volume of the sphere or size (V), the refractive index of the analyte ($n_a$) and form factor ($P(\theta)$).

$$i(\theta) = \left(\frac{1}{4\pi}\right) k^6 V^2 \left(\frac{n_a}{n_o} - 1\right)^2 P(\theta) \tag{4.2}$$

Eq. 4.1 can be substituted into the commonly known Rayleigh ratio ($R(\theta) \propto I_{\theta S}/I_0$) and then simplified and solved for *N* (number of particles per milliliter) leading to the following equation

$$N = \frac{k^2 R(\theta)}{i\,(\theta)} \tag{4.3}$$

Particle counting using Mie theory can be applied to particles spanning a range of 20-500 nm in diameter, but the reliability of using this model is greatly influenced by RI values and fitting parameters.

### 4.3.2 Rayleigh-Gans-Debye (RGD) Approximation

To satisfy the RGD approximation for particle counting, it is of interest to consider the Rayleigh ratio at the 0° angle instead at each individual angle θ; however, the 0° angle cannot be measured experimentally due to the placement of the MALS laser. For the RGD approximation, it is known that

$$\frac{K^{*}c}{R(\theta)} \approx \frac{1}{M_w\big(P(\theta)\big)} \tag{4.4}$$

$$K^{*} = \frac{4\pi^2 {n_0}^2}{N_A {\lambda_0}^2}\left(\frac{dn}{dc}\right)^2 \tag{4.5}$$

If the limit $\theta \to 0$ is considered, then $P(0) = 1$. Plugging this value back into Eq. 4.4, the RGD approximation can be rewritten as

$$R(0) \approx K^{*}c\, M_w \approx K^{*} n_i\, M_i^2 \tag{4.6}$$

The concentration can be considered as $c = n_i\, M_i^2$ and assuming the analyte has a mass ($M_i$), can occupy a volume ($V_i$) and thus a uniform density ($\rho$) so that $\rho = M_i/V_i$. If this holds true the following proportionality can be made:

$$N \propto \frac{R(0)}{V_i^2} \tag{4.7}$$

The upper size limit for using the RGD approximation is roughly 100 nm in diameter, prohibiting the use of the RGD approximation for a more polydisperse sample (20-500 nm). While Eqs. 4.3 and 4.7 are very similar, it is important to note the assumptions included in these theories: 1) particles are monodisperse in size 2) there are zero contributions of scattering from solvent, giving an absolute Rayleigh ratio (R(θ)) ($R(\theta_i) = R_s(\theta_i) - R_f(\theta_i)$ where $\theta_i$ = known angle, $R_s$= Rayleigh ratio of the solution and $R_f$ = Rayleigh ratio of carrier fluid), 3) real and imaginary refractive index (RI) values are known, and 4.) RGD approximation can be used when particle refractive index is close to the RI value of suspending fluid ($n_a/n_o - 1 \ll 1$). If the analyte is being examined after a separation has occurred, additional assumptions that should be considered are that 100 % sample recovery is achieved and there is no aggregation of the analyte.[29]

### 4.3.3 Particle Count Models

Current models that are used in determining particle counts consist of spherical and rod-shaped models. The latter is based off the RGD approximation and can give particle counts using a rod radius and RI value. Due to the focus of this work, particle counting with rods will not be discussed further. Three different spherical models can be used to analyze particles and follow either Mie theory or the RGD approximation. The "Lorenz-Mie" and "coated sphere" models follow Mie theory while "sphere" model follows the RGD approximation.

To successfully use these models, all three require sphere radius information which can be determined by online MALS along with the analytes' absolute and imaginary RI value. The sphere and Lorenz-Mie models only require one RI value whereas the coated sphere model needs two RI values (sphere and shell RI) and some knowledge of the shell thickness. Differences in particle counts based on model will be examined for a polystyrene latex standard and two different sets of OMVs in this study.

## 4.4 Results and Discussion

### 4.4.1 Validation of an AF4-MALS Method for Sized-Based Separation and Enumeration

#### 4.4.1.1 Adaptation and Validation of AF4 Method with PSL Standards

Current AF4 separations for biological particles or macromolecules use injection volumes that span 10-150 µL.[30,31] While these volumes are suitable for characterization, they may not be suitable for fraction collection and further offline analyses due to significant sample dilution. This may also lead to low light scattering intensities thereby impacting size analysis. To mitigate sample dilution and decrease the number of AF4 injections needed for sample collection, injection volumes of 200, 500, and 1000 µL were investigated. A polystyrene latex (PSL) mixture of 22, 100, and 496 nm particles was chosen due to the size range of the OMVs used in this study (25-500 nm). Each sample loop contained the same mass which was adjusted to accommodate the larger injection volumes, and retention time and sample recovery were evaluated across injection volumes.

As injection volume increased, consistent retention times and peak areas were observed for each species in the PSL mixture showing successful separations (Figures 4.1 and 4.7). Sample recovery, assessed by comparing the UV peak areas of the separated mixture from the area of the peak observed without the crossflow (Figure 4.7), was slightly higher than the accepted sample recovery of >70% across the three sample volumes.[32] For the 22, 100, and 496 nm PSL standard mixture, the total sample recovery was estimated to be 81, 83, and 75 % for the 200, 500, and 1000 µL loops, respectively. Thus, the AF4 method used here is amenable to scale-up without reduced sample recovery, and therefore the 1000 µL was used for separation of the OMVs to maximize the amount of sample processed per run.

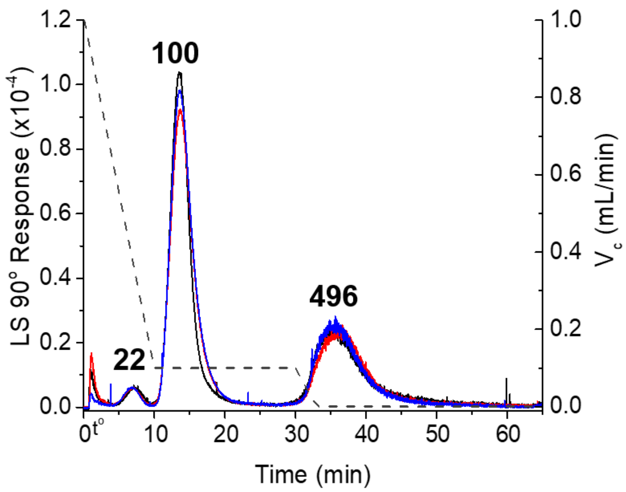

Figure 4.1 AF4-MALS separation of a 22, 100, and 500 nm polystyrene latex mixture using 200 (black), 500 (red) and 1000 (blue) µL sample loops. The dashed line and right y-axis shows the crossflow rate program

#### 4.4.1.2 MALS Particle Counting: Utilization of Spherical Models with PSL Standards

To understand the nuances associated with MALS particle counting, it was of interest to utilize the PSL standards used in the AF4 method development for particle counting. Expanding beyond the AF4 method, PSL has a known spherical shape and well-known RI value (1.58). Currently there is no latex particle count standard (< 1 µm) or count standard for biological particles, which would provide a better model for assessing MALS particle counting for OMVs. As discussed in the Methods section, the sphere and Lorenz-Mie models can be used to examine spherical particles. Since the 100 nm PSL particles are at the upper limit of the sphere model, this size was used to examine changes in particle count between the two models. The 22 nm PSL sample could not be fit to either the sphere or the Lorenz-Mie models. This could be due to the lower size limitations of the MALS used in this study. The Lorenz-Mie model could only be utilized for the 496 nm PSL because of that upper size limitation of the RGD approximation. Two additional assumptions are considered: PSL stock solutions are 1 % solids based on the manufacturer's certification of analysis (CoA) and 100 % recovery is achieved in the AF4 separation. Based on this estimated value and diameter of the particle, one can calculate a particle count using Eq. 4.8 where $W_v\%$ is the percent solids based on the CoA, $\rho_p$ is the polymer microsphere density, and $D$ is the diameter of the particle.

$$N_p = \frac{W_v\% \times 6x10^{10}}{\pi \rho_p D^3} \tag{4.8}$$

Experimental particle counts compared to nominal values for the 100 nm PSL can be seen in Figure 4.2. Both the sphere and Lorenz-Mie models have linear trends with good $R^2$ values (0.999). This linear trend demonstrates that we see the appropriate response to changes in particle counts with an increase in injected sample concentration. It would be suggested that if the calculated particle count was accurate and 100 % sample recovery was achieved, the slope of the line would reach unity. Between the two models, the Lorenz-Mie model has consistently larger particle counts compared to the sphere model by 11-12% raising question as to which is the more accurate model.

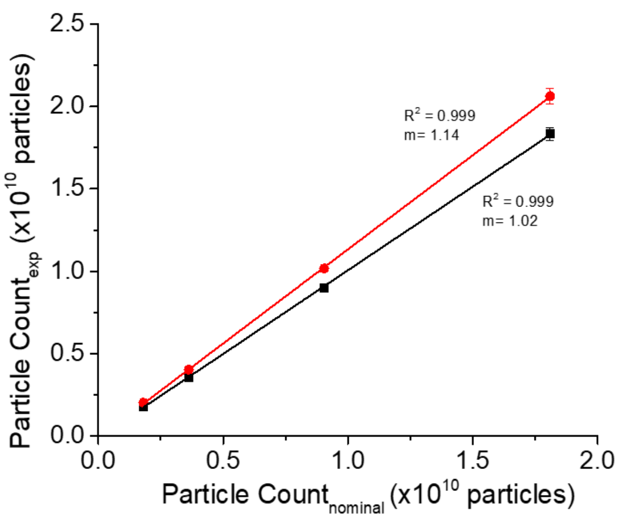


Figure 4.2 Comparison of experimental and nominal particles counts using the sphere (black squares) and Lorenz-Mie (red spheres) models for PSL standards. The nominal counts are based on a 200 µL injection volume and 1 % solid suspension of 100 nm PSL. Detectors 5-18 were used in this analysis.

One contribution to this consistent difference between the two models could lie within the measurement of the particle size or volume. In both Eqs. 4.2 and 4.7, the volume is a squared term, and inversely proportional to the number of particles per milliliter. Upon further investigation, online radius data showed minimal differences in size or changes in the uncertainty in the measurement (< 2 %). The other potential reasoning for this consistent difference is centered around the assumption $(n_a/n_o - 1 \ll 1)$. While the RI value for PSL is 1.58, the differences in particle count values between the two models can be examined by changing the RI values. Figure 4.3 shows an increasing percent difference between the two models as you increase the analyte's RI. Between RI values of 1.55 and 1.6, the percent difference ranges between 10.1 and 13.3 %, correlating to differences seen in Figure 4.2. This hints at the Lorenz-Mie model being a better suited model for samples with higher RI.

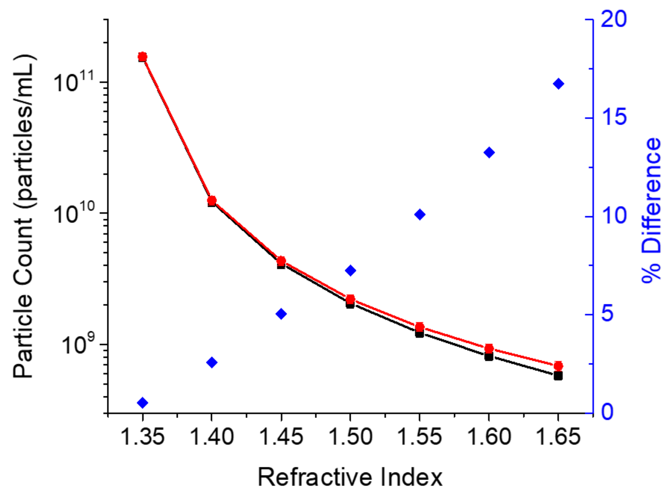


Figure 4.3 Changes in particle count with due to refractive index for 100 nm PSL particles using the sphere (black squares) and Lorenz-Mie (red circles) models

In addition to the two different models, another component of data processing is the use of different MALS detectors during the particle counting analysis. Because of this, the smaller angles should be kept on during data analysis to better satisfy the RGD approximation. Larger angles may also be selected as it is suggested that the more detectors selected would provide the best representation of the sample.

Effects of selected detectors during analysis of the 100 nm PSL can be seen in Figure 4.8 Three detector ranges were investigated (2-18, 5-18, and 9-18) based on their $R^2$ values. There were no significant changes in particle counts between selecting detectors 2-18 and 5-18 for either sphere or Lorenz-Mie models; however, the fits were drastically different with detectors 2-18 having an average $R^2$ = 0.05-0.07 and detectors 5-18 $R^2$ = 0.6-0.7. While the smallest angles (detectors 2-4) should satisfy the RGD approximation, they do not contribute to significantly different particle counts. Across the two models there is a difference between the use of detectors 5-18 and 9-18. This suggests that detectors 5-8 may be crucial to using MALS to calculate particle counts. The linearity of the data still hints to detector and model choice being major contributions to changes in experimental counts.

Revisiting the assumptions made for the calculated particle counts in Figures 4.2 and 4.7, it was assumed that PSL stock is 1 % solids. To assess how the slopes of each data set would change, calculated particle counts assuming 0.8 and 1.2 % solids were investigated. Between the two other sets of calculated counts, the data is still represented linearly, but there is a 22 % increase in slope for assuming 0.8 % solids and 18-19 % decrease in slope for 1.2 % solids (Figure 4.9). These trends are consistent where 0.8 % solids should have less particles compared to what we see with MALS, therefore a larger slope and the opposite effect with 1.2 % solids.

The 496 nm PSL particles were also examined considering the influences of calculated counts, detector selection and model choice. One major hindrance with a larger-sized population is that because light scatters in the more forward direction and to the diameter to the sixth power, saturation of the lower angled detectors (< detector 8, $\theta$= 64°) is easily achieved at low concentrations. To mitigate this, the laser power of the MALS had to be decreased to 25 %, and lower concentrations had to be utilized. This could make particle counting analysis of large particles, that scatter light more intensely, more challenging. Additionally, because of the larger diameter, only the Lorenz-Mie model could be assessed. Like Figures 4.2 and 4.8, the 496 nm PSL show a linear trend, but with much larger slopes (Figure 4.10). Again, the linear trends suggest that MALS can provide a good correlation between increased concentration and increased particle counts, but absolute particle counts cannot be determined.

### 4.4.2 Separation and Enumeration of *P. putida* OMVs using AF4-MALS

#### 4.4.2.1 Size-based Separation of *P. putida* OMVs using AF4-MALS

Given the methodological validation with a polydisperse mixture of PSL standards, we next sought to apply the AF4-MALS method to bioparticles and evaluate the effect of key parameters, such as model and RI, on counts. To generate OMVs, *P. putida* was cultivated in lignin-free or lignin-rich media, and bulk OMVs were harvested at 24 h from biological triplicates. OMVs harvested from both types of media were projected to contain both a small ($\bar{d}$ = 17 and 28 nm) and large ($\bar{d}$ = 120 and 307 nm) OMV populations in lignin-free and lignin-rich cultivations, respectively.[33] For OMV separation, an AF4 method with 1000 µL sample volume was applied to accomplish the following: (i) remove small particles ($d \approx$ 4-6 nm, approximately the size of a single protein) in the focusing step, (ii) elute small OMVs rapidly thereafter, and (iii) elute the large OMVs with intra-population separation.

AF4 separation, MALS signal, and radius were similar for the lignin-rich and lignin-free OMVs (Figure 4.4d). The total OMV populations for lignin-free samples display a lower light scattering signal and a lower size range ($d$=40-138 nm, both populations) compared to the lignin-rich OMVs ($d$=32-404 nm, both populations), which is similar yet slightly larger than each anticipated size range.[33] Close alignment between technical replicates demonstrates the AF4 method is reproducible. Within the larger OMV population, the continuous increase in the radius demonstrates intra-population separation is achieved (Figure 4.4d).[29] To the presence and characterize the smaller OMV population ($d$ < 30 nm), AF4 experiments using an isocratic crossflow rate of 0.1 mL/min were completed using the lignin-rich samples (Figure 4.4c). The retention times and MALS signal were then used to calculate the OMV size using AF4 theory to be 20-50 nm, and particle size was confirmed using batch DLS (Figure 4.4c), confirming the smaller population presence and size. OMV sizes across biological replicates is of interest to understand how size distributions vary. Finally, AF4-MALS was conducted on the biological replicates for both the lignin-free and lignin-rich samples. AF4 retention times, MALS signal (LS 90° Response), and radius distributions were consistent across the triplicates in both media conditions (Figure 4.4e and 4.4f). The higher signal-to-noise within the lignin-rich samples is due to the presence of larger particles, as light is scattered $\sim d^6$.

#### 4.4.2.2 Estimation of OMV RI Values using the Coated-Sphere Model

Despite PSL being a simple system to evaluate MALS particle counting, the structure and composition of OMVs are more complex. Thus, how to best represent these vesicles during analysis needs to be considered. The current understanding of *P. putida* OMVs suggests they should be modeled as a core-shell structure: compositionally the shell contains a mixture of lipopolysaccharides (LPS), phospholipids (PL), and transmembrane proteins while the core is filled primarily with water and protein, suggesting the core and shell may have different RIs. One major challenge with examining OMVs and other biological particles is the lack of experimentally determined RI values or methods to easily obtain this information.[34,35] Few studies have utilized experimental data from other techniques like NTA or flow cytometry scatter ratios (Flow- SR) of mammalian EVs to estimate RI values spanning 1.35-1.40.[34] One drawback is that these values may not effectively represent the OMVs used here due to differences in composition.

Taking a more calculated approach, the RI for OMVs could be determined based on the weight percent, partial specific volume of a sphere, and dn/dc values of the individual components to propose how composition changes the overall RI values (Table 4.2).[12] Using this approach, a range of RI values were determined for both the ‘shell’ and ‘core’ of the *P. putida* OMVs. For the RI value of the shell, it is understood that there is an LPS and PL bilayer in which transmembrane proteins can embed. Shell RI values were determined for a sliding ratio of LPS, PL, and protein from no protein in the OMV shell (50:50:0 LPS:PL:protein) to having more than half of the surface being protein (20:20:60 LPS:PL:protein). Similarly, core RI values for ranging water:protein content were determined (Table 4.1). Shell and core RIs ranged from 1.49-1.52 and 1.33-1.58, respectively**.** While this range appears to be broad, it encompasses a similar range of RI values determined for mammalian EVs.[36–40] In lieu of having compositional ratios of the OMV components it is important to not only consider how RI changes particle counts, but also how this may affect compositional heterogeneity in these biological systems, discussed in the next section.

#### 4.4.2.3 Impacts of RI and LS Model on OMV Particle Counts

The impact of RI and light scattering models on particle counts were examined. While both populations are present, the larger vesicle populations ranging from 8-17 min. (lignin-free) and 15-40 min. (lignin-rich) were used in evaluating the particle count method. The coated sphere model is considered to most closely approximate the OMV structure; additionally, the sphere and Lorenz-Mie models were assessed to identify trends in particle counts and sensitivities in the models.

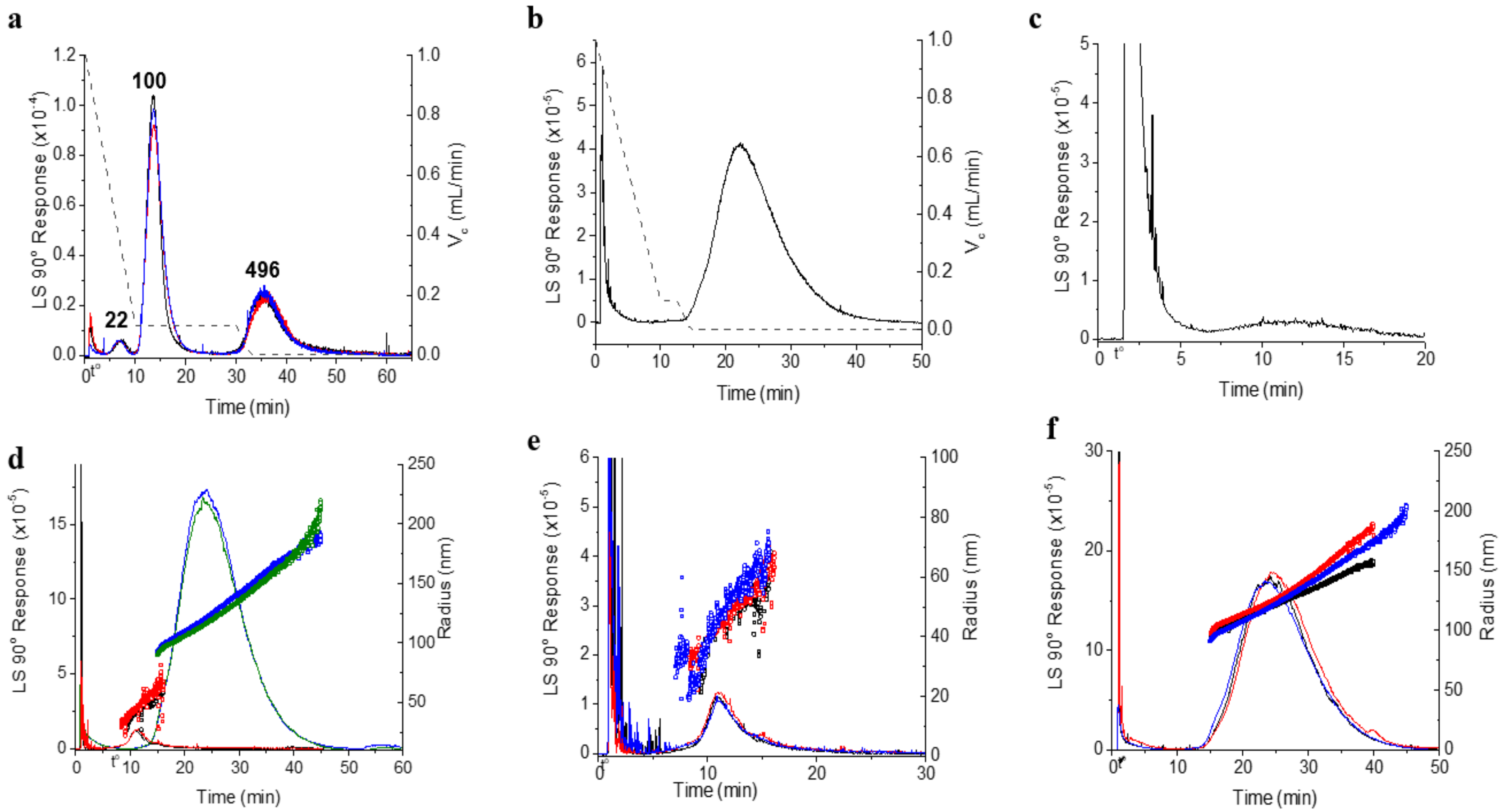


Figure 4.4 (a) Reproduction of Figure 3.1 for comparison with (b) AF4-MALS fractogram of lignin-rich OMVs overlayed with a modified AF4 crossflow program (dotted line) used to fractionate vesicles (c) AF4-MALS fractogram of lignin-rich OMVs separated using an isocratic crossflow of 0.1 mL/min (d) MALS responses and radius distributions across the AF4 separation of P. putida OMVs isolated from lignin-free (red and black traces) and lignin rich (blue and green traces) cultivations Technical duplicates are shown. Reproducibility of three biological replicates of P. putida OMVs (black, red, and blue) grown in (e) lignin-free and (f) lignin-rich media. Each MALS fractogram and radius distribution is an average of two AF4 injections

Table 4.1 Calculated dn/dc and RI values for the OMV core-shell structure (coated-sphere model) based on varying composition ratios.

| Ratio of LPS: PL: protein | dn/dc (mL/g) | RI Value |
|---|---|---|
| 50:50:0 | 0.14 | 1.49 |
| 40:40:20 | 0.15 | 1.50 |
| 33:33:33 | 0.16 | 1.50 |
| 20:20:60 | 0.17 | 1.52 |
| **Ratio of $H_2O$: protein** | | |
| 100 :0 | - | 1.33 |
| 80:20 | - | 1.38 |
| 50:50 | - | 1.46 |
| 20:80 | - | 1.53 |
| 0:100 | - | 1.58 |

Despite the sphere model having an upper size limit, it was of interest to observe if there were any major changes between the counts determined with sphere and Lorenz-Mie models for the lignin-rich OMVs. Moving forward, the RI values for the “core” of the coated sphere model will be termed “sphere RI.”

For lignin-free OMVs, the coated sphere model gives rise to unrealistic particle counts (> $10^{16}$ particles/mL) (Figure 4.5a), likely owing to poor signal-to-noise observed (Figure 4.4d and 4.4e). When looking at particle counts across the entirety of the peak within the ASTRA software, these erroneous counts greatly influence the total particle count. The sphere and Lorenz-Mie models show similar particle count; however, across the RI range of 1.35 to 1.65, a two order of magnitude change in particle counts is observed and is consistent between both OMV samples.

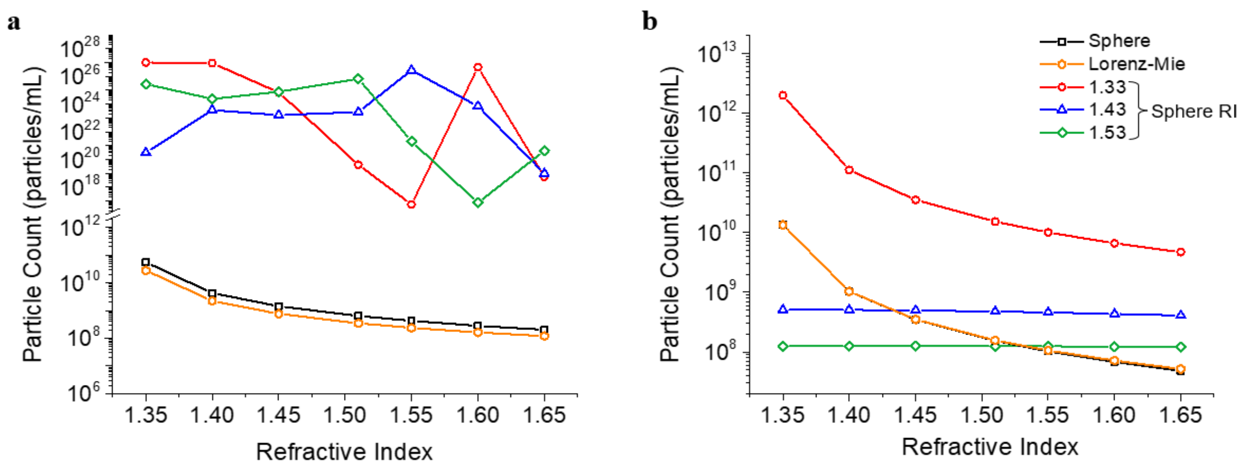


Figure 4.5 Effect of RI values and light scattering model on particle counts for results for (a) lignin-free and (b) lignin-rich samples. Light scattering models include sphere (black squares), Lorenz-Mie (orange hexagons), and coated sphere (red, blue, and green). For the coated sphere model, the sphere RI value was kept constant at 1.33, 1.43, or 1.53 while the shell RI value (x-axis) was changed. The shell thickness was held constant at 6 nm. Data corresponds to fractograms shown in Figures 4.3e and f.

Unlike the lignin-free OMVs, the lignin-rich OMVs do not exhibit the higher particle counts for the coated sphere model (Figure 4.5b) likely as lignin-rich samples exhibited a much lower signal-to-noise ratio owing to larger particle size (Figure 4.4f)**.** Instead, there is a trend where at low sphere RI values (1.33), the coated sphere model behaves similarly to the sphere and Lorenz-Mie model but gives rise to larger particle counts. With sphere RI values held constant 1.43 or 1.53, the particle counts are stabilized across the changing shell RI values and at a constant shell thickness. These trends hint at the sphere RI in the coated sphere model having a greater influence on particle counts. The difference in magnitude of the particle counts between sphere RI values of 1.43 and 1.53 can be attributed to the ratio of analyte and solvent refractive index that is seen in the single particle scattering function (i (θ), Eq. 4.2).

While this change in counts can be attributed to the sphere RI, this trend does not hold for the sphere RI of 1.33 and can be examined more closely via the shell RI and shell thickness. With respect to using the sphere model for the lignin-rich samples, the overall trend in counts matched those using the Lorenz-Mie model which is unexpected. Despite the upper size limit being lower than the sizes measured for the lignin-rich OMVs, the sphere model may not be showing major differences in particle counts due to the influence of detector selection as discussed earlier.

#### 4.4.2.4 Impacts of Shell Thickness on OMV Particle Counts

As the sphere RI approaches or equal the RI value of the suspending fluid using the coated sphere model, particle appear to increase significantly (Figure 4.5b, red trace). Because this trend deviates from the higher sphere RI values, the shell thickness and RI values could be influencing the magnitude of the particle counts. When examining different shell thickness values of 2, 4, and 6 nm across the different sphere RI values, a sphere value of 1.33 shows significant variation in particle counts with respect to shell refractive index and shell thickness[41] (Figure 4.6a).

Based on the results from Figures 4.5b and 4.5c, it can be concluded that the counts are not affected by either the shell RI or thickness (Figure 4.6b and 4.6c). This reiterates the dominating parameter in the coated sphere model is the sphere RI. In the case of unknown shell thickness and RI values, there is more leniency in the estimation of shell thickness compared to sphere RI values. Despite being a better representation of the OMVs, the sensitivity of the coated sphere model does not allow accurate particle counting. Therefore, particle counts in lignin-free and lignin-rich media cannot be compared using this model.

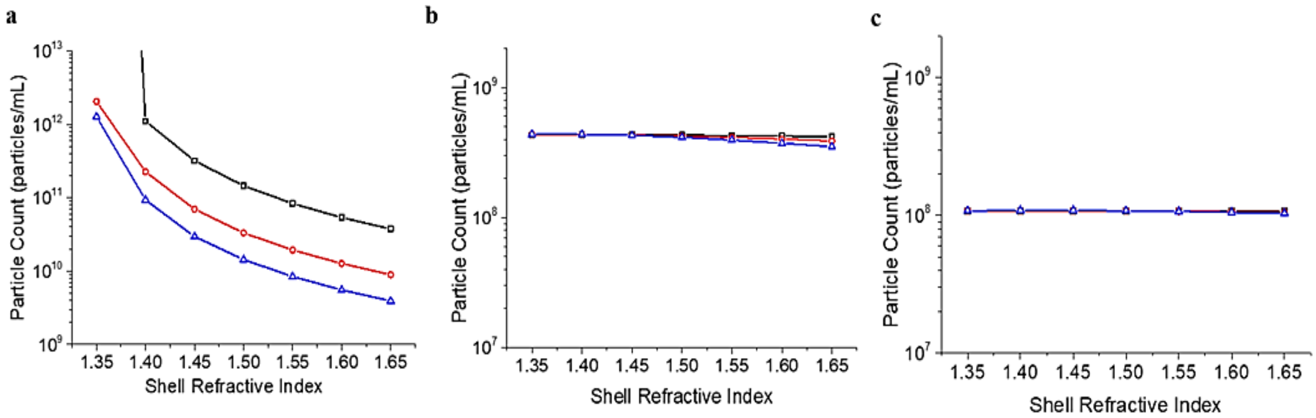


Figure 4.6 Effect of shell thickness on particle counts for the peak in the MALS fractogram of the lignin-rich samples using the coated sphere model. The sphere RI was kept constant at (a) 1.33, (b) 1.43, or (c) 1.53 while changing shell RI value. For each sphere and shell RI value combination, the particle counts were calculated for shell thicknesses of 2 (black), 4 (red), and 6 (blue) nm.

## 4.5 Conclusions

### 4.5.1 Separation and Enumeration of *P. putida* OMVs using AF4-MALS

This work presents an AF4-MALS method for the simultaneous separation and enumeration of polydisperse bioparticles, including bacterial OMVs. Key analyte-dependent parameters that impact MALS particle counts were identified to include light scattering theory/model, RI, and signal-to-noise ratio (S/N). Bioparticle counts via MALS was found to be most suitable when shape and RI are known, and good signal intensity at all angles is achieved. In sum, AF4-MALS can be used as a separation, enumeration, and purification method for bioparticles such as OMVs but relies on careful consideration of key MALS parameters.

The effect of light scattering theory was systematically evaluated for PSL standards and OMV bioparticles using sphere, Lorenz-Mie, and coated sphere models. Between the three spherical models studied, the coated sphere model is most sensitive to noise in the measured signal intensity; samples with S/N > 800 returned reasonable particle counts but were greatly influenced by the inner sphere RI. The sphere and Lorenz-Mie models are less sensitive to S/N, but a small RI range yields up to a 200% variation in OMV particle counts. Deviations between results from the sphere and Lorenz-Mie models can be attributed to assumptions within the light scattering theory and warrant special consideration when working with materials that strongly scatter light. To address this, improved model fits utilizing lower detector angles would provide more accurate particle counts for both sphere and Lorenz-Mie models. Moreover, the trends observed with PSL standards demonstrate appropriate and expected MALS responses, however only relative particle counts can be achieved. To determine absolute particle counts, a particle count standard with a closer refractive index to water (RI =1.33) would satisfy the assumptions made with the RGD approximation

RI selection also greatly impacts particle counts regardless of model, and therefore should be carefully and independently considered for each bioparticle's analysis. While biochemical analyses can inform the compositional ratio of biological particles and aid in calculating an RI, this remains a time-intensive process and is not a standard practice in the field. Thus, new methods for RI determination of bioparticles could aid in improving the accuracy of MALS particle counts and could impact other data analyses such as DLS.

### 4.5.2 Application of Fractionated OMVS and Particle Counts for OMV Protein Sorting

While the nature of the work showcased in this chapter is fundamental, it was of interest to further study how initial separation and quantification of the OMVs could improve offline characterization of the OMV proteome. In addition to the two OMV samples shown above which were cultivated after 24 hours, two additional OMV samples were examined: lignin-free and lignin-rich samples cultivated at 72-hours. Due to differences in size distributions between OMVs grown under lignin-free and lignin-rich conditions, it was originally hypothesized that the larger populations seen with the lignin-rich OMVs are more enriched with enzymes that are essential in breaking down aromatic compounds found within the beta-ketoadipate (βKA) pathway. Two collected OMV fractions for both sets of OMVs which were termed small OMVs (OMV-S, 30-180 nm = $d_h$) and large OMVs (OMV-L, 200-400 nm = $d_h$) were examined via shotgun proteomics. Initial findings show significant protein enrichment for the OMV-S fractions (~76-81 %) compared to OMV-L (~4 %) and hints at potential differences in biogenesis between OMV populations. Examining proteins found within the βKA pathway, eleven out of the fourteen proteins in the pathway were enriched within the OMV-S. populations.

While this initial proteomics study is qualitative, the particle counts obtained from MALS were used to examine different normalization strategies to compare the small and large OMV fractions. Applying particle counts as a normalization strategy the overall trend does not change, but there is a change in the magnitude of the fold-change compared to other normalization processes (e.g. median-centered). These initial proteomic experiments show how AF4-MALS can aid in identifying differences among OMV subpopulations and can be applied to other bacterial OMVs.

It should be noted that the proteomic characterization of *P. putida* OMVs used in this study was conducted by co-authors of this work at Oak Ridge National Laboratory. The specific experimental methods and results will be discussed in more detail in a future publication of this work.

## 4.6 Materials and Methods

### 4.6.1 Materials

Duke polystyrene latex (PSL) particles with sizes of 22, 100, and 496 nm (Thermo Fisher Scientific, Waltham, Massachusetts) were used in the AF4 method development and were suspended in 0.02% sodium azide (Sigma-Aldrich, St. Louis, Missouri) and 0.05% FL-70 surfactant (Thermo Fisher Scientific, Waltham, Massachusetts) in deionized 18.2 MΩ·cm water for the carrier fluid. For OMV separation, 150 mM phosphate buffered saline (PBS) was prepared with sodium chloride (Thermo Fisher Scientific, Waltham, Massachusetts), potassium chloride (Mallinckrodt Chemical, St. Louis, Missouri), sodium phosphate dibasic (Thermo Fisher Scientific, Waltham, Massachusetts), and potassium phosphate monobasic (Mallinckrodt Chemical, St. Louis, Missouri).

*Pseudomonas putida* KT2440 (*P. putida)* was inoculated into 50 mL of M9 minimal media (6.78 g/L $Na_2HPO_4$, 3 g/L $KH_2PO_4$, 0.5 g/L NaCl, 1 g/L $NH_4Cl$, 2 mM $MgSO_4$, 100 μM $CaCl_2$, and 18 μM $FeSO_4$) supplemented with 5 g/L glucose ("lignin-free" condition) or 5 g/L glucose plus 25% (v/v) alkaline liquor from corn stover pretreatment with NaOH ("lignin-rich" condition) in biological triplicate. These cultivation conditions were selected based on a previous study that suggested that OMV sizes depend on the media composition.[33] All chemicals other than 'the lignin-rich' liquor, which was made in-house as has been described previously,[42] were purchased from Sigma-Aldrich (St. Louis, Missouri). Cultivation conditions and OMV isolation and purification were performed as previously described.[33]

### 4.6.2 Asymmetrical Flow Field-Flow Fractionation (AF4) and Multi-angle Light Scattering (MALS)

All experiments were performed using an AF2000 system (Postnova Analytics, Salt Lake City, Utah) coupled to a SPD-20A UV/Vis detector (Shimadzu, Japan), multi-angle light scattering (MALS) DAWN HELEOS II (Wyatt Technology Corporation, Santa Barbara, California). The channel was formed with a tip-to-outlet length of 27.5 cm, breadth at channel inlet of 2 cm, breadth of channel outlet of 0.5 cm, and a spacer with a nominal thickness of 350 μm. The accumulation wall was a 30 kDa molecular weight cutoff regenerated cellulose membrane (Postnova Analytics, Salt Lake City, Utah). A 0.1 μm inline filter (Merck Millipore

Ltd, Ireland) between the HPLC pump and the AF4 channel was used to filter 0.02% sodium azide and 0.05 % FL-70 surfactant along with 1x PBS as the two carrier fluids used in this study.

The initial AF4-UV-MALS method had a focusing time of either 10 or 15 minutes, the injection flow rate was 0.2 mL/min, the detector flow rate was 0.5 mL/min, and the sample injection volume was either 200, 500, and 1000 µL. The crossflow rate was programmed to start at 1.0 mL/min during focusing, then decreased linearly to 0.1 mL/min over 10 minutes, held at 0.1 mL/min for 20 minutes, and then turned off. For OMV fractionation, the isocratic hold at 0.1 mL/min was shortened to 2.5 minutes after testing the methods with the different OMV samples used in this study. Changes in the methods can be seen in Figure 4.6.

### 4.6.3 Particle Counting Analysis using MALS

Data acquisition and particle counting analysis were performed using ASTRA 7.3.2.21 (Wyatt Technology Corporation, Santa Barbara, California). The MALS detector was normalized using bovine serum albumin (BSA) (Sigma-Aldrich, St. Louis, Missouri). For each PSL size, triplicate runs of each size were injected into the AF4 using the 200 µL loop and method described in the previous section. The 22 and 100 nm PSL particles were diluted by 200, 400, 1,000, or 2,000x and 90% of the MALS laser power was used. The 496 nm particles were diluted by 1,000, 2,000, 4,000, and 8,000x and the MALS laser power was set to 25 % to prevent saturation of the low-angled detectors (detectors 1-8). Using the ASTRA software, the sphere and Lorenz-Mie models and RI = 1.58 were used. Detectors 2-18, 5-18, and 9-18 were examined for the 100 nm and 2-18, 5-18, and 8-18 were used for 496 nm particles. Corresponding detector angles can be seen in Table 4.3.

For OMV particle counting, the MALS laser power was set to 90%, and the signal intensity was heavily despiked. In addition to the sphere and Lorenz-Mie models used in the PSL analysis, the coated sphere model was also examined. A RI range of 1.35-1.65 were used to encompass the varying composition of the OMVs which will be discussed more in the following section. Detector selection was based on what provided the best fit ($R^2$ value) across AF4 replicate measurements. For lignin-free samples, detectors 8-17 were selected while detectors 7-17 were chosen for the lignin-rich samples.

## 4.7 Supporting Information

### 4.7.1 AF4 Method Development

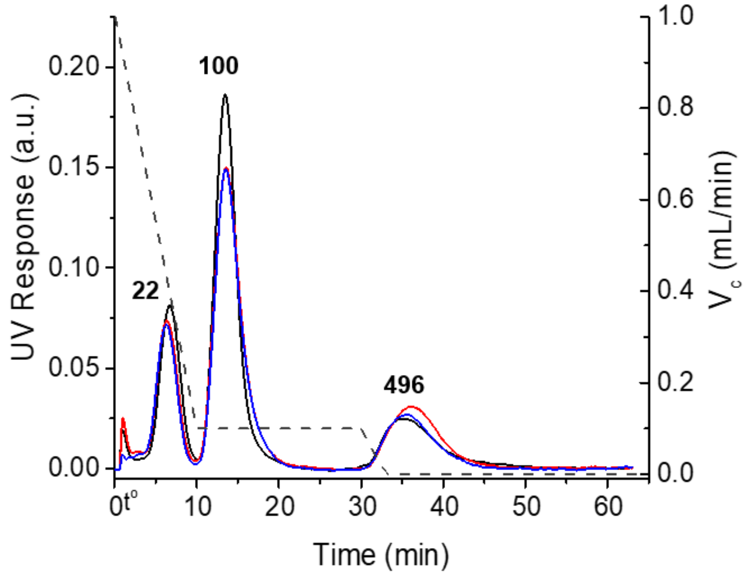


Figure 4.7 AF4-UV of a 22, 100, and 500 nm polystyrene latex mixture using 200 (black), 500 (red) and 1000 (blue) µL sample loops. The dashed line and right y-axis shows the crossflow rate program

### 4.7.2 Polystyrene and Spherical Models

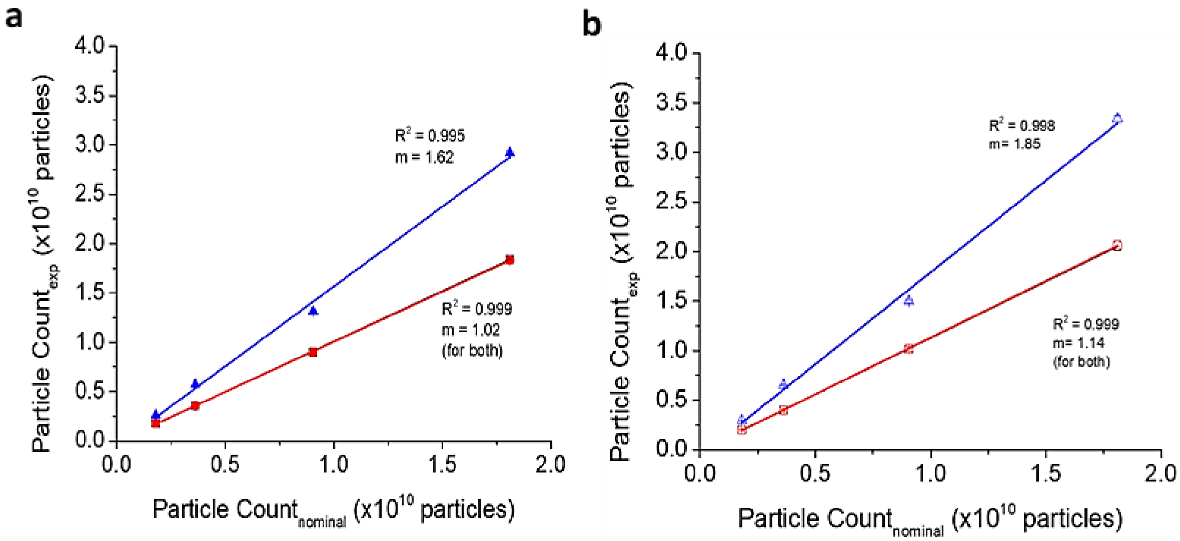


Figure 4.8 Influence of detectors selected in ASTRA for particle counting analysis of 100 nm PSL. Experimental MALS particle count using (a) the sphere and (b) Lorenz-Mie models compared to nominal particle count. Detectors 2-18 (black squares), 5-18 (red circles), and 9-18 (blue triangles) were used across both models.

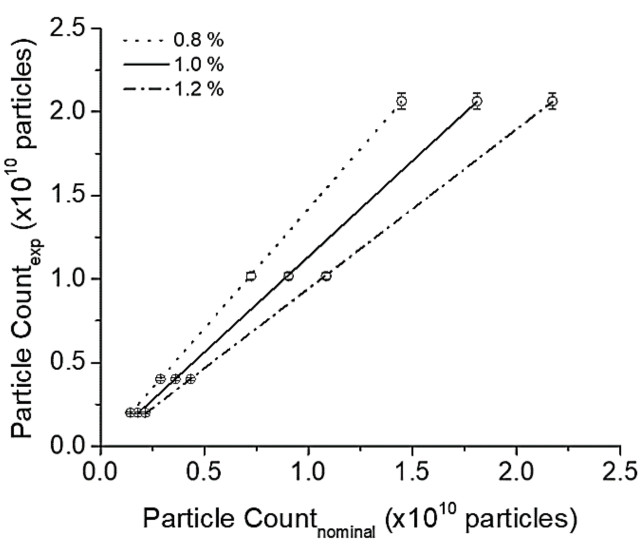


Figure 4.9 Influence of initial 100nm PSL stock solution concentration on nominal counts. Detectors 5-18 were used to determine experimental particle count

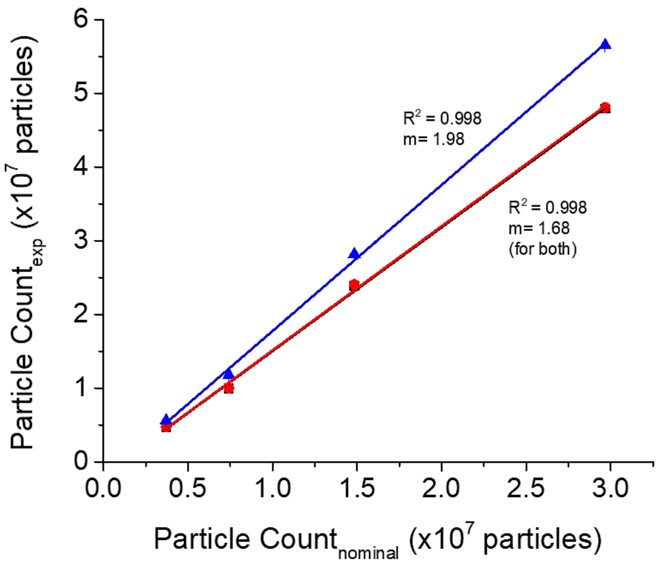


Figure 4.10 Influence of detectors selected in ASTRA for particle counting analysis of 496 nm PSL. Experimental particle count using the Lorenz-Mie model compared to nominal particle count. Detectors 2-18 (black squares), 5-18 (red circles), and 8-18 (blue triangles) were used.

### 4.7.3 OMV RI Values and Coated-Sphere Models

Table 4.2 Literature dn/dc and real RI values of the components of *P. putida* OMVs

| Component | Refractive Index | dn/dc (mL/g) |
|---|---|---|
| Polysaccharides/Lipopolysaccharides | - | 0.15[b,c] |
| Proteins | 1.584[a] | 0.18[b] |
| Phospholipids/lipid vesicles | 1.460[a] | 0.14[b] |
| Water | 1.333 | - |

[a] Wyatt DYNAMICS software manual

[b] https://www.materials-talks.com/blog/2013/06/18/refractive-index-increment-dndc-values/

[c] Santos *et al. ChemBioChem* **2003**, *4*, 96-100

Table 4.3 Detector number and corresponding angles for the DAWN HELEOS II instrument, adapted from Wyatt Technology Corporation

| Detector Number | Fixed Angles | Detector Number | Fixed Angles |
|---|---|---|---|
| 1 | 22.5 | 10 | 81.0 |
| 2 | 28.0 | 11 | 90.0 |
| 3 | 32.0 | 12 | 99.0 |
| 4 | 38.0 | 13 | 108.0 |
| 5 | 44.0 | 14 | 117.0 |
| 6 | 50.0 | 15 | 126.0 |
| 7 | 57.0 | 16 | 134.0 |
| 8 | 64.0 | 17 | 141.0 |
| 9 | 72.0 | 18 | 147.0 |

## 4.8 Acknowledgements

This material is based upon work primarily supported by the National Science Foundation (NSF) under NSF Award CHE-401438 (CLP and SKRW) along with the Colorado School of Mines Undergraduate Research Fellowship (MURF) (LB) and the National Renewable Energy Laboratory. The authors would like thank Wyatt Technology Corporation for the customer service support and suggestions.

## 4.9 References

(1) Jan, A. T. Outer Membrane Vesicles (OMVs) of Gram-Negative Bacteria: A Perspective Update. *Front Microbiol* **2017**, *8* (JUN), 1–11. https://doi.org/10.3389/fmicb.2017.01053.

(2) Naskar, A.; Cho, H.; Lee, S.; Kim, K. Biomimetic Nanoparticles Coated with Bacterial Outer Membrane Vesicles as a New-Generation Platform for Biomedical Applications. **2021**.

(3) Salvachúa, D.; Werner, A. Z.; Pardo, I.; Michalska, M.; Black, B. A. Outer Membrane Vesicles Catabolize Lignin-Derived Aromatic Compounds in Pseudomonas Putida KT2440. *PNAS* **2020**, *117* (17). https://doi.org/10.1073/pnas.1921073117.

(4) Bishop, D. G.; Work, E. *An Extracellular Glycolipid Produced by Escherichia Coli Grown under Lysine-Limiting Conditions*; 1965; Vol. 96.

(5) Sartorio, M. G.; Pardue, E. J.; Feldman, M. F.; Haurat, M. F. Bacterial Outer Membrane Vesicles : From Discovery to Applications. **2021**.

(6) Nagakubo, T.; Nomura, N.; Toyofuku, M. Cracking Open Bacterial Membrane Vesicles. *Front Microbiol* **2020**, *10* (January), 1–9. https://doi.org/10.3389/fmicb.2019.03026.

(7) Vogel, R.; Savage, J.; Muzard, J.; Camera, G. della; Vella, G.; Law, A.; Marchioni, M.; Mehn, D.; Geiss, O.; Peacock, B.; Aubert, D.; Calzolai, L.; Caputo, F.; Prina-Mello, A. Measuring Particle Concentration of Multimodal Synthetic Reference Materials and Extracellular Vesicles with Orthogonal Techniques: Who Is up to the Challenge? *J Extracell Vesicles* **2021**, *10* (3). https://doi.org/10.1002/jev2.12052.

(8) Coumans, F. A. W.; Van Der Pol, E.; Böing, A. N.; Hajji, N.; Sturk, G.; Van Leeuwen, T. G.; Nieuwland, R.; Bö Ing, A. N. Reproducible Extracellular Vesicle Size and Concentration Determination with Tunable Resistive Pulse Sensing. *J Extracell Vesicles* **2014**, *3* (25922). https://doi.org/10.3402/jev.v3.25922.

(9) Péter, P.; Terejánszky, T.; Makra, I. I.; Fü, P. P.; Róbert, R.; Gyurcsányigyurcsányi, E. Calibration-Less Sizing and Quantitation of Polymeric Nanoparticles and Viruses with Quartz Nanopipets. **2014**. https://doi.org/10.1021/ac500184z.

(10) Makra, I.; Terejánszky, P.; Gyurcsányi, R. E. A Method Based on Light Scattering to Estimate the Concentration of Virus Particles without the Need for Virus Particle Standards. *MethodsX* **2015**. https://doi.org/10.1016/j.mex.2015.02.003.

(11) Filipe, V.; Hawe, A.; Jiskoot, W. Critical Evaluation of Nanoparticle Tracking Analysis (NTA) by NanoSight for the Measurement of Nanoparticles and Protein Aggregates. *Pharm Res* **2010**, *27* (5), 796–810. https://doi.org/10.1007/s11095-010-0073-2.

(12) Wei, Z.; McEvoy, M.; Razinkov, V.; Polozova, A.; Li, E.; Casas-Finet, J.; Tous, G. I.; Balu, P.; Pan, A. A.; Mehta, H.; Schenerman, M. A. Biophysical Characterization of Influenza Virus Subpopulations Using Field Flow Fractionation and Multiangle Light Scattering: Correlation of Particle Counts, Size Distribution and Infectivity. *J Virol Methods* **2007**, *144* (1–2), 122–132. https://doi.org/10.1016/j.jviromet.2007.04.008.

(13) Adkins, G. B.; Sun, E.; Coreas, R.; Zhong, W. Asymmetrical Flow Field Flow Fractionation Coupled to Nanoparticle Tracking Analysis for Rapid Online Characterization of Nanomaterials. **2020**. https://doi.org/10.1021/acs.analchem.0c00406.

(14) Sitar, S.; Kejž, A.; Pahovnik, D.; Kogej, K.; Tušek-Znidarič, M.; Lenassi, M.; Zagar, E. Size Characterization and Quantification of Exosomes by Asymmetrical-Flow Field-Flow Fractionation. *Anal Chem* **2015**, *87*, 9225–9233. https://doi.org/10.1021/acs.analchem.5b01636.

(15) Gardiner, C.; Ferreira, Y. J.; Dragovic, R. A.; Redman, C. W. G.; Sargent, I. L. Extracellular Vesicle Sizing and Enumeration by Nanoparticle Tracking Analysis. *J Extracell Vesicles* **2013**, *2* (1). https://doi.org/10.3402/jev.v2i0.19671.

(16) Bachurski, D.; Schuldner, M.; Nguyen, P.-H.; Malz, A.; Reiners, K. S.; Grenzi, P. C.; Babatz, F.; Schauss, A. C.; Hansen, H. P.; Hallek, M.; Pogge, E.; Strandmann, V. Extracellular Vesicle Measurements with Nanoparticle Tracking Analysis – An Accuracy

and Repeatability Comparison between NanoSight NS300 and ZetaView. *J Extracell Vesicles* **2019**, *8*. https://doi.org/10.1080/20013078.2019.1596016.

(17) Andersson, M.; Wittgren, B.; Wahlund, K. G. Accuracy in Multiangle Light Scattering Measurements for Molar Mass and Radius Estimations. Model Calculations and Experiments. *Anal Chem* **2003**, *75* (16), 4279–4291. https://doi.org/10.1021/ac030128+.

(18) Gao, W.; Cohen, J.; Acholla, F.; Su, W. Development of Asymmetrical Flow Field Fractionation with On-Line Advanced Detections for Particle Size Distribution Analysis of Silica Colloidal Particles. *ACS Symposium Series* **2018**, *1281*, 111–143. https://doi.org/10.1021/bk-2018-1281.ch007.

(19) Mildner, R.; Hak, S.; Parot, J.; Hyldbakk, A.; Borgos, S. E.; Some, D.; Johann, C.; Caputo, F. Improved Multidetector Asymmetrical-Flow Field-Flow Fractionation Method for Particle Sizing and Concentration Measurements of Lipid-Based Nanocarriers for RNA Delivery. *European Journal of Pharmaceutics and Biopharmaceutics* **2021**, *163*, 252–265. https://doi.org/10.1016/j.ejpb.2021.03.004.

(20) Steppert, P.; Burgstaller, D.; Klausberger, M.; Tover, A.; Berger, E.; Jungbauer, A. Quantification and Characterization of Virus-like Particles by Size-Exclusion Chromatography and Nanoparticle Tracking Analysis. *J Chromatogr A* **2017**, *1487*, 89–99. https://doi.org/10.1016/j.chroma.2016.12.085.

(21) Zhang, H.; Lyden, D. Asymmetric-Flow Field-Flow Fractionation Technology for Exomere and Small Extracellular Vesicle Separation and Characterization. *Nat Protoc* **2019**, *14* (4), 1027–1053. https://doi.org/10.1038/s41596-019-0126-x.

(22) Zhang, H.; Freitas, D.; Kim, H. S.; Fabijanic, K.; Li, Z.; Chen, H.; Mark, M. T.; Molina, H.; Martin, A. B.; Bojmar, L.; Fang, J.; Rampersaud, S.; Hoshino, A.; Matei, I.; Kenific, C. M.; Nakajima, M.; Mutvei, A. P.; Sansone, P.; Buehring, W.; Wang, H.; Jimenez, J. P.; Cohen-Gould, L.; Paknejad, N.; Brendel, M.; Manova-Todorova, K.; Magalhães, A.; Ferreira, J. A.; Osório, H.; Silva, A. M.; Massey, A.; Cubillos-Ruiz, J. R.; Galletti, G.; Giannakakou, P.; Cuervo, A. M.; Blenis, J.; Schwartz, R.; Brady, M. S.; Peinado, H.; Bromberg, J.; Matsui, H.; Reis, C. A.; Lyden, D. Identification of Distinct Nanoparticles and Subsets of Extracellular Vesicles by Asymmetric Flow Field-Flow Fractionation. *Nat Cell Biol* **2018**, *20* (3), 332–343. https://doi.org/10.1038/s41556-018-0040-4.

(23) Put, R. M. F. Van Der; Spies, A.; Metz, B.; Some, D.; Scherrers, R.; Pieters, R. Validation of an FFF-MALS Method to Characterize the Production and Functionalization of Outer-Membrane Vesicles for Conjugate Vaccines. *Anal Chem* **2022**, *94*, 12033–12041. https://doi.org/10.1021/acs.analchem.2c01590.

(24) Dell'annunziata, F.; Folliero, V.; Giugliano, R.; De Filippis, A.; Santarcangelo, C.; Izzo, V.; Daglia, M.; Galdiero, M.; Arciola, C. R.; Franci, G.; Belén Flórez, A. Molecular Sciences Gene Transfer Potential of Outer Membrane Vesicles of Gram-Negative Bacteria. *Int J Mol Sci* **2021**, 5985. https://doi.org/10.3390/ijms.

(25) Reimer, S. L.; Beniac, D. R.; Hiebert, S. L.; Booth, T. F.; Chong, P. M.; Westmacott, G. R.; Zhanel, G. G.; Bay, D. C. Comparative Analysis of Outer Membrane Vesicle Isolation Methods With an Escherichia Coli TolA Mutant Reveals a Hypervesiculating Phenotype

With Outer-Inner Membrane Vesicle Content. *Front Microbiol* **2021**, *12*. https://doi.org/10.3389/fmicb.2021.628801.

(26) Schwechheimer, C.; Kuehn, M. J. Outer-Membrane Vesicles from Gram-Negative Bacteria: Biogenesis and Functions. *Nature Reviews Microbiology*. Nature Publishing Group September 16, 2015, pp 605–619. https://doi.org/10.1038/nrmicro3525.

(27) Kerker, M. *The Scattering of Light and Other Electromagnetic Radiation*, 1st ed.; Loebl, E. M., Ed.; Academic Press, 1969. https://doi.org/https://doi.org/10.1016/C2013-0-06195-6.

(28) Wyatt, P. J.; Weida, M. J. Method and Apparatus for Determining Absolute Number Densities of Particles in Solution. US 6,774,994 B1, 2004.

(29) McEvoy, M.; Razinkov, V.; Wei, Z.; Casas-finet, J. R.; Tous, G. I.; Schenerman, M. A. Improved Particle Counting and Size Distribution Determination of Aggregated Virus Populations by Asymmetric Flow Field-Flow Fractionation and Multiangle Light Scattering Techniques. **2011**, 547–554. https://doi.org/10.1002/btpr.499.

(30) Leeman, M.; Choi, J.; Hansson, S.; Storm, M. U.; Nilsson, L. Proteins and Antibodies in Serum, Plasma, and Whole Blood-Size Characterization Using Asymmetrical Flow Field-Flow Fractionation (AF4). https://doi.org/10.1007/s00216-018-1127-2.

(31) Gao, Z.; Hutchins, Z.; Li, Z.; Zhong, W. Offline Coupling of Asymmetrical Flow Field-Flow Fractionation and Capillary Electrophoresis for Separation of Extracellular Vesicles. **2022**. https://doi.org/10.1021/acs.analchem.2c03550.

(32) Caputo, F.; Vogel, R.; Savage, J.; Vella, G.; Law, A.; Della Camera, G.; Hannon, G.; Peacock, B.; Mehn, D.; Ponti, J.; Geiss, O.; Aubert, D.; Prina-Mello, A.; Calzolai, L. Measuring Particle Size Distribution and Mass Concentration of Nanoplastics and Microplastics: Addressing Some Analytical Challenges in the Sub-Micron Size Range. *J Colloid Interface Sci* **2021**, *588*, 401–417. https://doi.org/10.1016/j.jcis.2020.12.039.

(33) Salvachúa, D.; Werner, A. Z.; Pardo, I.; Michalska, M.; Black, B. A.; Donohoe, B. S.; Haugen, S. J.; Katahira, R.; Notonier, S.; Ramirez, K. J.; Amore, A.; Purvine, S. O.; Zink, E. M.; Abraham, P. E.; Giannone, R. J.; Poudel, S.; Laible, P. D.; Hettich, R. L.; Beckham, G. T. Outer Membrane Vesicles Catabolize Lignin-Derived Aromatic Compounds in Pseudomonas Putida KT2440. *PNAS* **2020**, *117*, 1–9. https://doi.org/10.1073/pnas.1921073117.

(34) Welsh, J. A.; Pol, E. van der; Bettin, B. A.; Carter, D. R. F.; Hendrix, A.; Lenassi, M. Towards Defining Reference Materials for Measuring Extracellular Vesicle Refractive Index , Epitope Abundance , Size and Concentration. *J Extracell Vesicles* **2020**, *9* (1). https://doi.org/10.1080/20013078.2020.1816641.

(35) Ramirez, M. I.; Amorim, M. G.; Gadelha, C.; Milic, I.; Welsh, J. A.; Freitas, V. M.; Nawaz, M.; Akbar, N.; Couch, Y.; Makin, L.; Cooke, F.; Vettore, A. L.; Batista, P. X.; Freezor, R.; Pezuk, J. A.; Rosa-Fernandes, L.; Carreira, A. C. O.; Devitt, A.; Jacobs, L.; Silva, I. T.; Coakley, G.; Nunes, D. N.; Carter, D.; Palmisano, G.; Dias-Neto, E. Technical Challenges of Working with Extracellular Vesicles. *Nanoscale* **2018**, *10* (3), 881–906. https://doi.org/10.1039/c7nr08360b.

(36) van der Pol, E.; Coumans, F. A. W.; Grootemaat, A. E.; Gardiner, C.; Sargent, I. L.; Harrison, P.; Sturk, A.; van Leeuwen, T. G.; Nieuwland, R. Particle Size Distribution of Exosomes and Microvesicles Determined by Transmission Electron Microscopy, Flow Cytometry, Nanoparticle Tracking Analysis, and Resistive Pulse Sensing. *Journal of Thrombosis and Haemostasis* **2014**, *12* (7), 1182–1192. https://doi.org/10.1111/jth.12602.

(37) Gardiner, C.; Shaw, M.; Hole, P.; Smith, J.; Tannetta, D.; Redman, C. W.; Sargent, I. L. Measurement of Refractive Index by Nanoparticle Tracking Analysis Reveals Heterogeneity in Extracellular Vesicles. *J Extracell Vesicles* **2014**, *3* (25361), 1–6. https://doi.org/10.3402/jev.v3.25361.

(38) Pol, E. Van Der; Rond, L. De; Coumans, F. A. W.; Gool, E. L.; Böing, A. N.; Sturk, A.; Nieuwland, R. Absolute Sizing and Label-Free Identification of Extracellular Vesicles by Flow Cytometry LPs EVs. *Nanomedicine* **2018**, *14* (3), 801–810. https://doi.org/10.1016/j.nano.2017.12.012.

(39) Geeurickx, E.; Tulkens, J.; Dhondt, B.; Deun, J. Van; Lippens, L.; Vergauwen, G.; Heyrman, E.; Sutter, D. De; Gevaert, K.; Impens, F.; Miinalainen, I.; Bockstal, P. Van; Beer, T. De; Wauben, M. H. M.; Nieuwland, R.; Braems, G.; Callewaert, N.; Mestdagh, P.; Vandesompele, J. The Generation and Use of Recombinant Extracellular Vesicles as Biological Reference Material. *Nat Commun* **2019**, *10*, 3288–3298. https://doi.org/10.1038/s41467-019-11182-0.

(40) Rond, L. De; Libregts, S. F. W. M.; Rikkert, L. G.; Hau, C. M.; Pol, E. Van Der; Nieuwland, R.; Leeuwen, T. G. Van. Refractive Index to Evaluate Staining Specificity of Extracellular Vesicles by Flow Cytometry. *J Extracell Vesicles* **2019**, *8* (1). https://doi.org/10.1080/20013078.2019.1643671.

(41) Santos, N. C.; Silva, A. C.; Castanho, M. A. R. B.; Martins-silva, J.; Saldanha, C. Evaluation of Lipopolysaccharide Aggregation by Light Scattering Spectroscopy. **2003**, 96–100.

(42) Linger, J. G.; Vardon, D. R.; Guarnieri, M. T.; Karp, E. M.; Hunsinger, G. B.; Franden, M. A.; Johnson, C. W.; Chupka, G.; Strathmann, T. J.; Pienkos, P. T.; Beckham, G. T. Lignin Valorization through Integrated Biological Funneling and Chemical Catalysis. *PNAS* **2014**, *111* (33), 12013–12018. https://doi.org/10.1073/pnas.1410657111.

CHAPTER 5

# PROBING THE COMPOSITIONAL SENSITIVITY OF AQUEOUS THERMAL FIELD-FLOW FRACTIONATION THROUGH THE ACIDIC COMONOMERS OF POLYMER COLLOIDS

Prepared for submission to *Analytica Chimica Acta*

Christine L. Plavchak[1], Wei Gao[2], David M. Meunier[3], Yongfu Li[3], Edwin Mes[4], Pu Luo[2], S. Kim. Ratanathanawongs Williams[1]

## 5.1 Abstract

In this study, the compositional sensitivity of thermal field-flow fractionation (ThFFF) in aqueous solutions is examined through the use of a model polymer colloid system containing subtle differences in their acidic comonomer content (0-3 %). The particles in this system have similar diameters and provide a platform for understanding the effect of additives and particle composition on ThFFF retention and particle thermal diffusion ($D_T$). Tetrabutylammonium perchlorate (TBAP) and FL-70 detergent, which have both been used previously in ThFFF, were the focus of this work. Thermal FFF results showed that TBAP had a large impact on retention while FL-70 was important for sample recovery. Differences in $D_T$ were observed between particles having < 1 % difference in their acidic comonomer content depending on the additives used in the carrier fluid. The retention time that is measured by ThFFF is proportional to $D_T$ and the translational diffusion coefficient ($D$). To assess $D_T$, accurate $D$ values are needed. To this end, asymmetrical flow FFF (AF4) and batch dynamic light scattering (DLS) were used to measure $D$. Comparison of these values to those obtained via on-line DLS helped identify

---

[1] Laboratory for Advanced Separations Technologies, Department of Chemistry, Colorado School of Mines, Golden, Colorado, 80401, USA
[2] The Dow Chemical Company, Collegeville, Pennsylvania, 19426
[3] The Dow Chemical Company, Midland, Michigan, 48674
[4] The Dow Chemical Company, Ternuzen, Netherlands

possible influences of fluid flow on *D*. Results show that flow rates as low as 0.3 $mLmin^{-1}$ can cause an erroneously large *D* values. While this ultimately impacts the magnitude of calculated $D_T$ values, it does not impact overall trends observed across samples with differing acrylic acid content.

## 5.2 Introduction

Field-flow fractionation (FFF) is a family of methods used for the separation and characterization of colloids and other macromolecules. Each FFF technique utilizes a different field to interact with analytes of interest and drive them towards an accumulation wall. The analytes' translational diffusion causes their transport in an opposite direction to the field-induced motion. At steady state, each analyte cloud has an exponential concentration profile with a unique average thickness that is dependent on the opposing transport processes. Differences in translational diffusion coefficient (*D)* allows for a size-dependent concentration gradient to be established.[1] Retention within an FFF channel depends on the physicochemical properties of the analyte and their interactions with the applied field as well as *D*.

Thermal field-flow fractionation (ThFFF) is a technique within the FFF umbrella that utilizes a temperature gradient to fractionate macromolecular and colloidal samples. The separation mechanism of ThFFF is governed by both the analyte's *D* (or size) along with the interactions at the solvent-analyte interface. This additional interaction leads to a compositional sensitivity providing both separation and characterization of the analyte simultaneously. The primary separation mechanism is based on the ratio of an analyte's thermal diffusion coefficient ($D_T$) to its translational diffusion coefficient (*D*) along with knowledge of the temperature gradient that is applied ($\Delta T$).[2] Thermal FFF has been predominantly used to examine polymers with complex composition and architecture but has also been successful with characterizing compositionally different colloids.[3–5] In organic solvents, similar sized latex particles such as polystyrene, polymethyl methacrylate, and polybutadiene have been shown to have different ThFFF retention times which correspond to differences in their $D_T$.[6,7] Differences in surface functionalities for particles of the same composition have also led to changes in particle $D_T$ such as pre- and post-silanization of silica particles.[8] Latexes with carboxyl or amide groups have also been compared to those that are non-functionalized and changes in ThFFF retention were observed. It is also noted that additional components added to the carrier fluids (e.g., salts or surfactants) can amplify differences in retention.

While this compositional sensitivity is easily observed with homopolymer latexes and latexes with different surface functionalities, expansion to more complex particle compositions has led to a debate on whether the differences in retention are due to bulk or surface compositions.[9,10] Additionally, minor changes in particle composition also give rise to questions centered around the compositional resolution of ThFFF yet little has been done to assess this sensitivity. Two works have examined differences in core-shell latex compositions, but changes in the particles size due to swelling have prohibited this compositional resolution from being further studied.[11,12]

Polymer colloids synthesized via emulsion polymerization are employed at large scale in well-established consumer products such as coatings, adhesives, home, and personal care along with many emerging applications in energy, biotechnology, and medicine. The stability of polymer colloids during production, transportation, and formulation to final products is often an important aspect during product design and scale up. The incorporation of acidic comonomers into the polymer colloids during emulsion polymerization provides an avenue to manipulate the stability through electrostatic stabilization. Analysis of colloidal surfaces with low acid moieties is challenging and requires a separation step ideally done under aqueous conditions.

Performing ThFFF experiments under aqueous conditions (AqThFFF) has been inherently challenging due to the need to incorporate additives into the carrier fluid in order to improve retention of analytes.[13,14] Additional limitations of AqThFFF center around the use of aqueous buffers with ionic strengths or pHs that can corrode the ThFFF channel surface and the reduced ability to cool the sample accumulation wall when higher field strengths are used. Changes in analyte retention have also been poorly understood due to different particle thermophoresis theories across literature.[15–21] Previous work has examined differences in particle retention by changing anions and cations of different salts, ionic strength, and utilizing different surfactants.[8,22–26] While there have been attempts to identify general trends in increasing or decreasing retention, there still remains a lack of understanding of how additives control retention and how they can help characterize differences in particle composition..

This work aims to probe AqThFFF's sensitivity to subtle changes in low acid moieties (< 3%) of a model polymer colloid system. To improve retention of these latexes within the ThFFF channel, four different carrier fluid compositions were examined. The two main components of these carrier fluid mixtures contained both or either tetrabutylammonium perchlorate (TBAP) and FL-70 detergent. These two main additives were chosen because of their use in previous FFF literature and their aid in improving the retention of colloids in thermal and asymmetrical flow FFF[5,8,9,13]. Across these carrier liquid systems, trends in $D_T$ and retention, sample recovery, and changes in size of the colloids were examined. The measured ThFFF retention time is proportional to $D_T/D$ and thus $D$ values are required in order to calculate $D_T$. Asymmetrical flow

FFF (AF4) and DLS (batch and on-line modes) were used to determine $D$ and also examine the effect of fluid flow on DLS measurements.

## 5.3 Results and Discussion

The measurement of $D$ is important as this value is subsequently used to calculate $D_T$ and infer information about colloid composition. In addition to examining the effect of additives, experiments are performed with batch-mode DLS, flow-through DLS using a syringe pump, and AF4 with on-line DLS to better understand the impact of flow rate on $D$ and $d_h$.

### 5.3.1 Influence of Carrier Fluid Additives on Colloid Diffusion Coefficient Determined by Batch DLS

Prior to AF4 or ThFFF experiments, batch DLS was completed on the colloids to assess any impact of the carrier fluid additives on particle size. Table 5.1 summarizes the average diffusion coefficients of the colloids suspended in the different carrier fluids used in this study. Across the colloid samples, those containing 0 to 3 % AA had similar $D$ values of 5.6-6.1 x$10^{-8}$ $cm^2$ $s^{-1}$ ($d_h$ = 78-86 nm, Table 5.4) while the 1 % AA redox sample has a smaller $D$ of 4.7 x$10^{-8}$ $cm^2$ $s^{-1}$ ($d_h$ = 101 nm). Dilution of the colloids from the stock (water) into a 0.05 % FL-70 carrier fluid showed a slight, but insignificant, decrease in $D$. Because the diffusion coefficients (and diameters) are not significantly different across the five carrier fluids, any differences in ThFFF retention could be attributed to changes in particle $D_T$.

### 5.3.2 Determination of Colloid Diffusion Coefficients Using AF4

Since batch DLS provides average values, AF4 was performed to better understand $D$ and size distribution for each of the colloid samples. AF4 theory allows for $D$ to be determined from retention time ($t_r$) if a constant crossflow rate ($V_c$) is applied. For well retained analytes, Eq. 5.1 can be used to calculate $D$ and $d_h$ from results obtained using an AF4 channel with thickness ($w$), void volume ($V^0$) and void time ($t^0$).[27]

Table 5.1 Diffusion coefficients of BA: MMA: AA colloids determined by batch DLS using $H_2O$ (pH = 7), 0.1 mM TBAP (pH = 6.5), 0.1mM TBAP and 0.1 mM NaOH (pH = 9.9), 0.1 mM TBAP and 0.05 % FL-70 (pH = 9.8), and 0.05 % FL-70 (pH = 9.8) as the suspending fluid

| Composition (BA:MMA:AA) | Sample (% AA) | $D_{,H2O}$ (x$10^{-8}$ cm$^2$ s$^{-1}$) | $D_{,\mathrm{TBAP}}$ (x$10^{-8}$ cm$^2$ s$^{-1}$) | $D_{,\mathrm{TBAP+NaOH}}$ (x$10^{-8}$ cm$^2$ s$^{-1}$) | $D_{,\mathrm{TBAP+FL\text{-}70}}$ (x$10^{-8}$ cm$^2$ s$^{-1}$) | $D_{,\mathrm{FL\text{-}70}}$ (x$10^{-8}$ cm$^2$ s$^{-1}$) |
|---|---|---|---|---|---|---|
| 50: 50 : 0 | 0 | 5.6 ± 0.2 | 5.7 ± 0.2 | 5.9 ± 0.2 | 6.0 ± 0.2 | 5.9 ± 0.2 |
| 49.75 : 49.74 : 0.51 | 0.5 | 6.1 ± 0.2 | 6.4 ± 0.2 | 6.5 ± 0.2 | 6.5 ± 0.2 | 6.4 ± 0.2 |
| 49.5 : 49.5 : 1 | 1 | 5.7 ± 0.2 | 6.2 ± 0.2 | 6.0 ± 0.1 | 6.3 ± 0.2 | 6.4 ± 0.2 |
| 49 : 49 : 2 | 2 | 6.1 ± 0.2 | 6.2 ± 0.2 | 5.8 ± 0.6 | 6.3 ± 0.2 | 6.3 ± 0.2 |
| 48.5 : 48.5 : 3 | 3 | 6.1 ± 0.2 | 6.3 ± 0.3 | 6.0 ± 0.2 | 6.3 ± 0.2 | 6.3 ± 0.3 |
| 49.5 : 49.5 : 1 | 1R | 4.7 ± 0.2 | 4.8 ± 0.2 | 4.8 ± 0.1 | 4.6 ± 0.2 | 4.9 ± 0.2 |

Figure 5.1 shows the AF4-UV fractograms of the different % AA samples using 0.1 mM TBAP and 0.05 % FL-70 in water as the carrier fluid. Consistent retention times at peak max are observed for the 0.5 to 3 % AA samples while the 0 % AA and 1 % redox sample are shifted to higher retention times. Eq. 5.1 with $t_r$ at peak maximum was used to calculate the $D$ values that are overlaid over the fractograms. These AF4 $D$ values show a similar trend to those obtained by batch DLS (Table 5.1).

$$t_r = \frac{t^0 V_c w^2}{6DV^0} \tag{5.1}$$

In addition to using AF4 theory to calculate $D$ and $d_h$ values, the impact of online DLS was examined and showed consistently larger $D$ (and smaller $d_h$) values than compared to batch DLS measurements for all colloids. This is mainly due to the influence of the flowrate (0.5 mL/min) used in the AF4 separation and will be explained in more detail later in this work. Despite the AF4 results providing similar sizes to those determined by batch DLS, AF4 is unable to identify differences between the colloids containing 0.5 and 3 % AA.

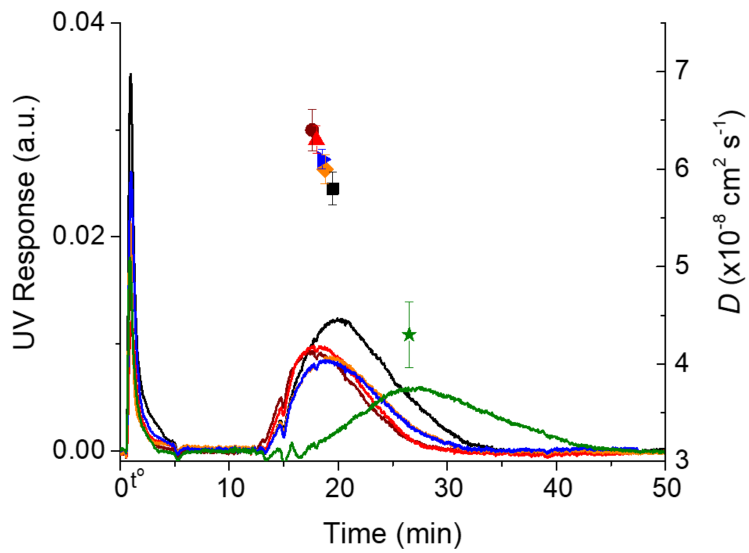

Figure 5.1 AF4-UV fractograms of BA: MMA: AA colloids using 0.1 mM TBAP and 0.05 % FL-70 in water as the carrier fluid. Fractograms correspond (left y-axis) to colloids having 0 (black), 0.5 (maroon), 1 (red), 2 (orange), 3 (blue), 1 redox (green) % AA in the synthesis monomer feed. $V_c$ was held constant at 0.5 mL/min. The individual data points (right y-axis) are the *D* values at peak maxima calculated using Eq. 1.

### 5.3.3 AqThFFF of Acrylate Colloids

The consistency in the of elution profiles for the colloids observed in AF4 and *D* values from batch DLS in all solvents allowed for further investigation of the compositional sensitivity of AqThFFF. Additionally, the influence of different carrier fluid additives on retention and sample recovery could also be assessed without an influence of size. As mentioned previously, the use of TBAP in both organic and AqThFFF carrier fluids at various concentrations (0.01-1mM) has shown to improve colloidal retention.[8,9,26,28,29] However the driving mechanism as to why this quaternary salt increases retention is still poorly understood and there is a lack of information regarding the sample recovery of the latexes when using TBAP as an additive to the carrier fluid.

When injected into the AqThFFF channel using 0.1 mM TBAP solution, a trend arises with the thermal-initiated samples where the 0 % AA sample has the largest retention time. As the amount of AA increases, AqThFFF retention time decreases (Figure 5.2a). The longer retention time for the 1 % AA redox is expected as the colloids are slightly larger in diameter. While it provides good retention for all of the colloids, the sample recovery for all of the samples in 0.1 mM TBAP is inadequate ranging from 30-44% with the exception of the 3% AA sample (77%) (Table 5.5). This poor sample recovery is hypothesized to be due to the reversible adsorption of the particles onto the cold wall or the spacer material. Figure 5.3 demonstrates the loss of light scattering and concentration signal across three subsequent AqThFFF injections. To understand this phenomenon, both the LS and UV signal were monitored after transitioning the solvent from 0.1 mM TBAP in water, to 18.2 MΩ·cm water, and then finally to acetonitrile. With no field applied, it is not until the instrument is fully flushed with acetonitrile that an increase in LS and UV signal is observed at 25 minutes (Figure 5.3b) which suggests a release of adsorbed latexes from the channel.

Comparing 0.1 mM TBAP (pH = 6.5) fractograms to those using 0.1 mM TBAP and 0.1 mM NaOH (pH = 9.9), it is observed that the trends in retention are the same yet the incorporation of NaOH causes all colloids to be less retained (Figure 5.2b). Despite the decrease in retention times, the sample recovery is almost doubled that of TBAP alone ranging from 65-77% (Table 5.5) and the peak widths are consistent with those at pH = 6.5. This shift to a lower retention time and increased sample recovery could be due fewer particle-wall interactions. Another potential mechanism could lie within the use of NaOH. Hydroxide ions in aqueous solutions have been hypothesized to be ‘high mobility’ ions and have a mobility towards the cold wall.[24] Because of this, it could push analytes towards the hot wall and causing them to be positioned in higher flow velocity streamlines in the parabolic flow profile.

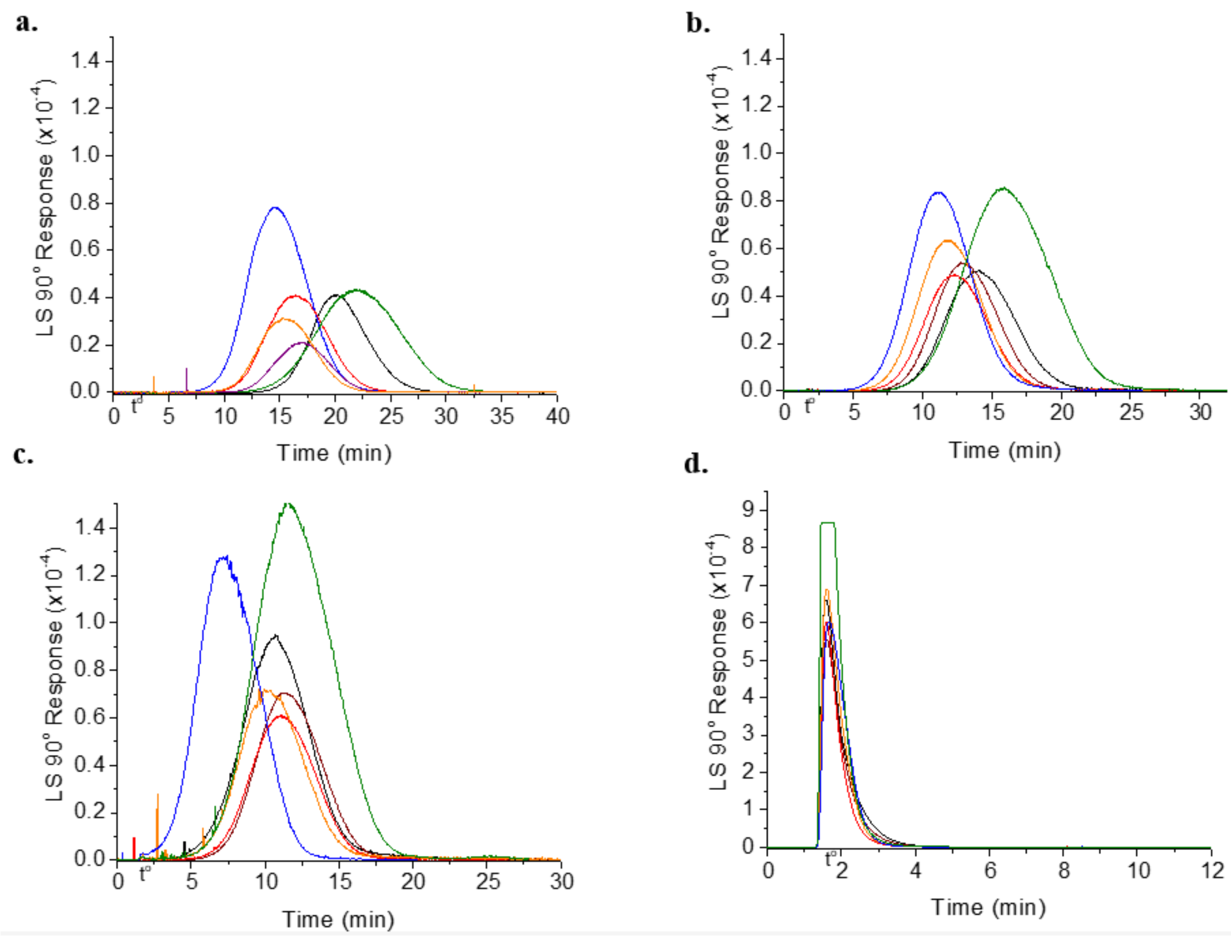


Figure 5.2 Superimposed AqThFFF fractograms of BA: MMA: AA colloids using (a) 0.1 mM TBAP, pH = 6.5, (b) 0.1 mM TBAP and 0.1 mM NaOH, pH 9.9, (c) 0.1 mM TBAP and 0.05 % FL-70, pH = 9.8, and (d) 0.05 % FL-70, pH = 9.8 as the carrier fluids. Fractograms correspond to colloids having 0 (black), 0.5 (maroon), 1 (red), 2 (orange), 3 (blue), 1 redox (green) % AA in the synthesis monomer feed. Experimental conditions: $V_o$ = 0.3 mL/min, ΔT= 41-43 K, $T_c$ = 305 K

Utilizing 0.1 mM TBAP and 0.05 % FL-70 as the carrier fluid shows similar retention trends as the other two carrier fluid compositions but the colloids are less retained than in 0.1 mM TBAP and 0.1 mM NaOH (Figure 5.2c). The one major difference across the retention trends in all three solvents is that the 0 % AA sample no longer has the highest retention time of the thermal-initiated samples. This could be due to the lack of acidic comonomer in this sample or a different particle-solvent interaction between the colloid surface and FL-70 components.

The use of FL-70 improves sample recovery (67-84 %), but what component of the detergent that is increasing the recovery is unknown and continues to be a major question in the FFF community (Table 5.5). Unlike improving retention in AF4, using 0.05 % FL-70 as the carrier fluid does not increase retention for this particular latex system. Figure 5.2d shows that there is no retention of the colloids within the AqThFFF channel. Across all the carrier fluids, it can be seen that the use of TBAP is governing retention and impacting the trend observed in the latex samples.

While TBAP is dominating retention trends for the colloids, it is also important to probe is whether the differences in retention using NaOH or FL-70 are strictly due to pH or additive effects. One way to examine this is to look at the peak widths of the fractograms in TBAP, TBAP and NaOH, and TBAP and FL-70. Comparing the peak widths between TBAP and TBAP with NaOH, there is no change in peak width indicating no potential change in charge on the colloids. When using FL-70 instead of NaOH however, the peak width decreases, and overall peak intensity increases. The change in peak width between NaOH and FL-70 at similar pH values suggests that these retention effects and increases in recovery are dictated by the additives used.

In conjunction with additives used in the carrier fluids, surface charge of the colloids is another factor that could be impacting AqThFF retention. Across all solvents the zeta potential of all the colloids is negative, but vary depending on the solvents used. Dilution of the colloids from the original stock solution in water give rise to a more negative zeta potential with increasing AA content with the exception of the 0% AA sample (Table 5.6). A similar trend arises when the colloids are in TBAP, but the zeta potential is less negative for the colloids than in water. Across the TBAP and NaOH, TBAP and FL-70, and FL-70 solutions, the zeta potentials across all samples show no trend in relating charge to % AA. This suggests that similar to pH, surface charge is not a dominating factor in the case of the observed AqThFFF retention trends.

### 5.3.4 Variability in Colloid Thermal Diffusion Coefficients

Qualitatively, the trends identified in the previous section show sensitivity to subtle changes in overall acidic comonomer content and can be greatly influenced by carrier fluid additives. Based on these trends and the AF4, the compositional sensitivity of AqThFFF can be examined through calculating the thermal diffusion values of the different colloids which is related to the Soret coefficient ($S_T$). In ThFFF, the retention parameter, λ, depends on an analyte's translational diffusion coefficient ($D$), thermal diffusion coefficient ($D_T$), and field strength (ΔT) (Eq. 5.2).

$$\lambda = \frac{D}{D_T \Delta T} = \frac{1}{S_T \Delta T} \tag{5.2}$$

An analyte's λ is related to its retention time ($t_r$) and channel's void time ($t^0$) through the retention ratio (R). In ThFFF, λ must be corrected for the perturbations in the parabolic flow profile due to the temperature gradient inducing variations in carrier fluid viscosity. This leads to the expression:

$$R = 6\lambda \left\{ v + (1 - 6\lambda v) \left[ \coth\left(\frac{1}{2\lambda}\right) - 2\lambda \right] \right\} \tag{5.3}$$

Because of the subtle variations in retention time across of the colloids used in this study, it was of interest to further compare $D$ values obtained from both batch DLS and online DLS measurements. The comparison of $D$ values across all methods provides a platform to ensure accurate values are being used in the calculation of $D_T$. Table 5.7 shows average $D$ values for the colloids when measured by batch DLS with no flow ($D_{DLS}$), calculated from AF4 theory

($D_{AF4}$), online AF4-DLS ($D_{AF4\text{-}DLS}$), online ThFFF-DLS ($D_{ThFFF\text{-}DLS}$), and transformed from online radius of gyration ($R_g$) ($D_{ThFFF\text{-}Rg}$) values using TBAP and FL-70 as the carrier fluid. For all samples, the latter transformation was assuming a hard sphere thus an $R_g/R_h$ ratio of 0.78. Across the table, $D_{DLS}$, $D_{AF4}$, and $D_{ThFFF\text{-}Rg}$ values are not significantly different from one another while values from online AF4 and ThFFF show upwards of a 20 % increase in $D$ relating to a smaller diameter. One other anomaly can be observed in the 1 % redox sample for $D_{ThFFF\text{-}Rg}$ value. Compared to the other thermally initiated samples, this value is significantly different from the $D_{DLS}$ and $D_{AF}$ results. This could hint at the redox samples being slightly swollen in solution, giving rise to a slightly different $R_g/R_h$ ratio thus impacting the transformation from $R_g$ to $D$.

To further understand if the ~20 % difference in $D$ measurements is related to the flow rates used in AqThFFF and AF4, batch DLS experiments were completed at different flow rates (Figure 5.4). It can be seen in Figure 5.4a that the expected hydrodynamic radius does not change significantly up to 0.1 mLmin$^{-1}$ but begins to decrease at 0.3 mLmin$^{-1}$ which coincides with the same flow rate used in the ThFFF experiments. A more prominent change of ~ 20 % in size can be seen with a flow rate of 0.5 mLmin$^{-1}$ which coincides with the AF4 experiments. This impact of fluid flow on $D$ measurements is mainly due to the standard bore of the MALS flow cell (1.2 mm) and this has also been observed in other studies.[30] For While utilizing the average $D$ value to calculate experimental $D_T$s, obtaining online $D$ values may also help in examining if $D_T$ values change across a sample.

Again, from Table 5.1 the overall $D$ values do not vary across the carrier fluids hinting at the changes in particle retention seen in Figure 5.2 must be due to changes in particle $D_T$. When using the $D$ values from Table 5.7, similar $D_T$ values for $D_{T,\,DLS}$, $D_{T,\,AF4}$, and $D_{T,\,ThFFF\text{-}Rg}$ are observed but a much larger $D_T$ is determined using online $D$ values when the particles are in TBAP and FL-70 (Table 5.2). The $D$ value used, while doesn't change the overall trend of $D$ values across the colloid samples, it does impact the magnitude of $D_T$ for the colloids.

Table 5.2 Experimentally determined $D_T$ values for BA: MMA: AA colloids in 0.1 mM TBAP and 0.05 % FL-70 as the carrier fluid

| Sample (% AA) | $D_{T, DLS}$ (x10$^{-8}$ cm$^2$ s$^{-1}$) | $D_{T, AF4}$ (x10$^{-8}$ cm$^2$ s$^{-1}$) | $D_{T, AF4\text{-}DLS}$ (x10$^{-8}$ cm$^2$ s$^{-1}$) | $D_{T, ThFFF\text{-}DLS}$ (x10$^{-8}$ cm$^2$ s$^{-1}$) | $D_{T, ThFFF\text{-}Rg}$ (x10$^{-8}$ cm$^2$ s$^{-1}$) |
|---|---|---|---|---|---|
| 0 | 3.0 ± 0.1 | 2.86 ± 0.09 | 4.2 ± 0.1 | 3.5 ± 0.1 | 2.9 ± 0.2 |
| 0.5 | 3.3 ± 0.1 | 3.3 ± 0.1 | 4.6 ± 0.1 | 4.1 ± 0.1 | 3.2 ± 0.2 |
| 1 | 3.2 ± 0.1 | 3.20 ± 0.09 | 4.6 ± 0.1 | 3.9 ± 0.1 | 3.1 ± 0.2 |
| 2 | 2.9 ± 0.1 | 2.77± 0.08 | 4.1 ± 0.1 | 3.43 ± 0.09 | 2.8 ± 0.2 |
| 3 | 2.06 ± 0.08 | 2.00 ± 0.06 | 2.85 ± 0.08 | 2.38 ± 0.07 | 2.0 ± 0.2 |
| 1R | 2.5 ± 0.1 | 2.3 ± 0.1 | 4.1 ± 0.1 | 3.12 ± 0.09 | 2.8 ± 0.1 |

With this in mind $D_{DLS}$ values were used to calculate $D_T$ values for the different colloids using the different carrier fluids (Table 5.3). With 0.1 mM TBAP as the carrier fluid, the $D_T$ values match the trend observed in retention whereas % AA increases, $D_T$ decreases. Using 0.1 mM TBAP and 0.1 mM NaOH showcases a similar trend however the 0 and 0.5 % AA along with the 2 and 3 % AA samples have the same $D_T$. For 0.1 mM TBAP and 0.05 % FL-70, a similar trend exists except for the 0 % AA sample. Another component to examine is potential differences between the 1 % thermal and redox sample. Using TBAP alone or TBAP and NaOH as the carrier fluid, there are no significant differences between the $D_T$ values of these samples. Substituting FL-70 with TBAP instead of NaOH shows a significant difference between the two samples. While not clear what the driving factor of this change in $D_T$ is (bulk or surface composition, FL-70 components, etc.) it hints at the use of additives may attenuate or amplify potential analyte composition differences. AqThFFF is a promising technique to look at subtle compositional differences in analytes under aqueous conditions.

Table 5.3 Experimentally determined $D_T$ values for BA: MMA: AA colloids in 0.1 mM TBAP, 0.1 mM TBAP and 0.1 mM NaOH, and 0.1 mM TBAP and 0.05 % FL-70. $D_T$ values were calculated using different $D$ values determined by batch DLS

| Sample (% AA) | $D_{T,TBAP}$ ($x10^{-8}$ $cm^2$ $s^{-1}$ $K^{-1}$) | $D_{T, TBAP+NaOH}$ ($x10^{-8}$ $cm^2$ $s^{-1}$ $K^{-1}$) | $D_{T, TBAP+FL-70}$ ($x10^{-8}$ $cm^2$ $s^{-1}$ $K^{-1}$) |
|---|---|---|---|
| 0 | $4.7 \pm 0.2$ | $3.4 \pm 0.1$ | $3.0 \pm 0.1$ |
| 0.5 | $4.4 \pm 0.2$ | $3.4 \pm 0.1$ | $3.3 \pm 0.1$ |
| 1 | $4.0 \pm 0.2$ | $3.1 \pm 0.1$ | $3.2 \pm 0.1$ |
| 2 | $3.5 \pm 0.1$ | $2.8 \pm 0.1$ | $2.9 \pm 0.1$ |
| 3 | $3.4 \pm 0.2$ | $2.8 \pm 0.1$ | $2.06 \pm 0.08$ |
| 1 R | $3.8 \pm 0.2$ | $3.1 \pm 0.1$ | $2.5 \pm 0.1$ |

## 5.4 Conclusion

The compositional sensitivity of AqThFFF was probed through the use of a model latex system with subtle differences in the acidic comonomer content (0-3% AA). After confirmation that the colloids used were of similar diameters though DLS and AF4, it was possible to uncover potential trends in ThFFF retention and thus composition. Qualitatively TBAP appears to be the dominant additive in dictating retention yet the use of NaOH and FL-70 improve sample recovery dramatically. NaOH and FL-70 increased the pH of the system yet their impacts on retention are suggested to be due to the identity of the additive itself and not a pH effect. By determining the $D_T$ values of the colloids under different carrier fluids, it is shown that AqThFFF can distinguish between 0 and 0.5% AA depending on the carrier fluid compositions. Across all carrier fluids examined, more distinct differences can be observed in $D_T$ between the 0.5 and 3 % AA samples which is a smaller range than previous literature has reported (0-9 %).[12] Similar to organic ThFFF and polymer analysis, solvent and/or additive selection along with accurate diffusion coefficient information is paramount in determining differences in particle composition.

## 5.5 Materials and Methods

### 5.5.1 Synthesis of Acrylate Colloids

Butyl acrylate: methyl methacrylate: acrylic acid (BA:MMA:AA) colloids were synthesized using a semi-batch polymerization with 1 % sodium laurel sulfate as a surfactant, buffered using sodium bicarbonate, and left for six hours at 85 °C under nitrogen. To initiate the polymerization, persulfates and sodium sulfoxylate formaldehyde (SSF) with t-butyl hydroperoxide (t-BHP) were used as the thermal and redox initiators, respectively. The colloids contained an equal ratio of butyl acrylate and methyl methacrylate, and subtle differences in acrylic acid comonomer (0-3 %).

### 5.5.2 Carrier Fluid Composition

Four different carrier liquids were used and consisted of deionized 18.2 MΩ·cm water with the following additives: 0.1 mM tetrabutylammonium perchlorate (TBAP, pH = 6.5) (Sigma-Aldrich, St. Louis, Missouri), 0.1 mM TBAP and 0.1 mM sodium hydroxide (Thermo Fisher Scientific, Waltham, Massachusetts) (pH 9.9), 0.1 mM TBAP and 0.05 % FL-70 surfactant (Thermo Fisher Scientific, Waltham, Massachusetts) (pH 9.8), or 0.05 % FL-70 (pH = 9.8). TBAP and FL-70 were chosen due to their previous successes in increasing particle retention in aqueous ThFFF.[8,13] Sodium hydroxide was used as a pH modifier with TBAP to better examine pH effects with and without the use of FL-70.

### 5.5.3 Zeta Potential

Surface charge of the colloids were examined in all carrier fluids described above using a Zetasizer Nanoseries instrument (Malvern Panalytical, Malvern, United Kingdom). A clear folded capillary zeta cell (DTS1060C) and Zetasizer software v6.01 were used to measure and process all samples.

### 5.5.4 Asymmetrical Flow Field-Flow Fractionation and Dynamic Light Scattering (AF4-DLS)

All experiments were performed using an AF2000 system (Postnova Analytics, Salt Lake City, Utah) coupled to a SPD-20A UV/Vis detector (Shimadzu, Japan), multi-angle light scattering/dynamic light scattering (MALS/DLS) DAWN HELEOS II (Wyatt Technology Corporation, Santa Barbara, California). The channel was formed with a tip-to-outlet length of 27.5 cm, breadth of 2 cm and 0.5 cm at the channel inlet and outlet respectively, and a spacer with a nominal thickness of 350 µm. The accumulation wall was a 30 kDa molecular weight cutoff regenerated cellulose membrane (Postnova Analytics, Salt Lake City, Utah). A 0.1 µm inline filter (Merck Millipore Ltd, Ireland) between the PN1130 pump and the AF4 channel was used to filter an aqueous solution with 0.1 mM TBAP and 0.05 % FL-70 surfactant.

The AF4-UV-MALS method consisted of a 5-minute focus time, injection flow rate of 0.2 mL/min, detector flow rate of 0.5 mL/min, and a constant crossflow rate of 0.5 mL/min. The colloids were injected into the channel using a 20 µL sample loop. All samples were prepared via dilutions from particle stock solutions (~34-39 % solids) to equate to 0.4 mg/mL concentrations. A further 1:2 sample dilution occurred to achieve approximately 4 µg of sample analyzed per AF4 experiment. Batch DLS measurements were also completed to assess impacts of carrier fluid composition on colloid size. Using a syringe pump, diluted suspensions were introduced into the HELEOS II detector using flow rates of 0.5, 0.3, 0.1 and 0.0 mL/min.

### 5.5.5 Thermal Field-Flow Fractionation (ThFFF)

Experiments were performed using a homemade ThFFF system described previously[31] and coupled to a MALS/DLS DAWN HELEOS II (Wyatt Technology Corporation, Santa Barbara, California) and a Model SPD-6A UV-Vis detector (Shimadzu Corporation, Kyoto, Japan). The ThFFF channel was formed using a 127 µm Mylar spacer with a ribbon-like section removed that was 2.0 cm in breadth and a tip-to-outlet length of 27.5 cm. For all experiments, the temperature difference between the hot and cold walls ($\Delta T$) was 41-43 K, the ThFFF cold wall and MALS temperature were maintained at 303-305K, and a 10 µL sample loop was used to introduce the sample into the channel. All carrier fluids were pumped into the channel using an Agilent 1100 series quaternary pump (Agilent Technologies, Santa Clara, California) flowing at 0.3 mL/min. All samples were prepared via dilutions from particle stock solutions as described in the previous section. Because of the smaller sample loop used for ThFFF experiments, the 1:2 dilution used in AF4 experiments was not performed to keep injection masses consistent at 4 µg per run.

## 5.6 Supporting Information

Table 5.4 consists of the same information as in Table 5.1 but *D* values were transformed to hydrodynamic diameters through the use of Stokes Einstein's equation.

Table 5.4 Hydrodynamic diameters of BA: MMA: AA colloids determined by batch DLS using H2O (pH = 7), 0.1 mM TBAP (pH = 6.5), 0.1mM TBAP and 0.1 mM NaOH (pH = 9.9), 0.1 mM TBAP and 0.05 % FL-70 (pH = 9.8), and 0.05 % FL-70 (pH = 9.8) as the suspending fluid.

| Composition (BA: MMA: AA) | Sample (% AA) | $d_{h,H2O}$ (nm) | $d_{h,\text{TBAP}}$ (nm) | $d_{h,\text{TBAP + NaOH}}$ (nm) | $d_{h,,\text{TBAP + FL-70}}$ (nm) | $d_{h,\text{FL-70}}$ (nm) |
|---|---|---|---|---|---|---|
| 50: 50 : 0 | 0 | 86 ± 2 | 89 ± 2 | 90 ± 3 | 86 ± 2 | 83 ± 2 |
| 49.75: 49.74: 0.51 | 0.5 | 78 ± 2 | 81 ± 2 | 81 ± 2 | 80 ± 2 | 77 ± 2 |
| 49.5: 49.5: 1 | 1 | 83 ± 2 | 85 ± 3 | 87 ± 2 | 83 ± 2 | 77 ± 2 |
| 49: 49: 2 | 2 | 79 ± 2 | 86 ± 2 | 89 ± 3 | 84 ± 4 | 79 ± 2 |
| 48.5: 48.5: 3 | 3 | 79 ± 2 | 84 ± 5 | 87 ± 4 | 83 ± 3 | 79 ± 5 |
| 49.5 : 49.5 : 1 | 1R | 101 ± 3 | 110 ± 5 | 108 ± 3 | 108 ± 3 | 100 ± 3 |

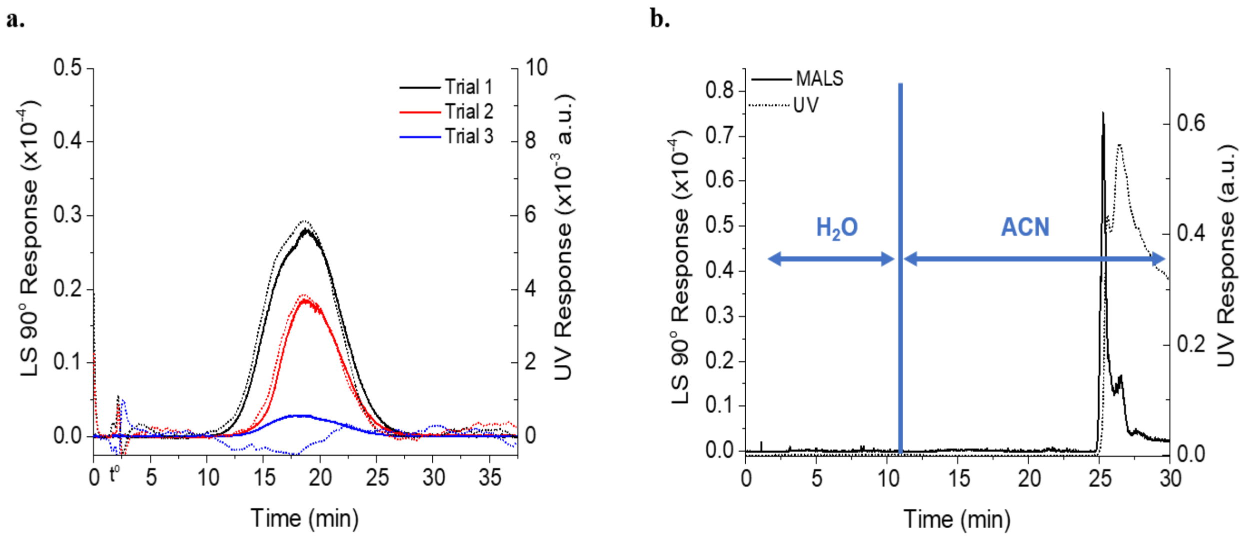


Figure 5.3 (a) Triplicate AqThFFF-MALS-UV fractograms of the 0% AA colloids with 0.1 mM TBAP as the carrier fluid and (b) transitioning the ThFFF channel back to acetonitrile after flushing with water and no temperature gradient.

Table 5.5 Percent sample recovery for each colloidal suspension using different carrier liquids.

| Sample (% AA) | TBAP | TBAP + NaOH | TBAP + FL-70 |
|---|---|---|---|
| 0 | 44 ± 14 | 76 ± 2 | 67 ± 8 |
| 0.5 | 30 ± 10 | 67 ± 1 | 79 ± 1 |
| 1 | 44 ± 17 | 72 ± 5 | 84 ± 2 |
| 2 | 39 ± 24 | 65 ± 2 | 82 ± 5 |
| 3 | 77 ± 17 | 77 ± 1 | 72 ± 3 |
| 1 R | 33 ± 24 | 72 ± 2 | 82 ± 7 |

Table 5.6 Zeta potential (ζ) values for BA: MMA: AA colloids in 0.1 mM TBAP, 0.1 mM TBAP and 0.1 mM NaOH, and 0.1 mM TBAP and 0.05 % FL-70.

| Sample (%AA) | $\zeta_{H2O}$ (mV) | $\zeta_{TBAP}$ (mV) | $\zeta_{TBAP,NaOH}$ (mV) | $\zeta_{TBAP,FL\text{-}70}$ (mV) | $\zeta_{FL\text{-}70}$ (mV) |
|---|---|---|---|---|---|
| 0 | -64 ± 1 | -50 ± 1 | -60 ± 1 | -59.0 ± 0.5 | -62 ± 1 |
| 0.5 | -57 ± 1 | -51.4 ± 0.5 | -59.0 ± 0.2 | -59 ± 1 | -63 ± 1 |
| 1 | -62 ± 2 | -52 ± 1 | -60.5 ± 0.2 | -58 ± 1 | -63 ± 1 |
| 2 | -66 ± 3 | -57 ± 2 | -62.7 ± 0.4 | -58.2 ± 0.3 | -62 ± 1 |
| 3 | -68 ± 2 | -66 ± 1 | -62.1 ± 0.4 | -58 ± 1 | -60 ± 2 |
| 1R | -62 ± 2 | -51 ± 1 | -60.9 ± 0.4 | -58 ± 1 | -60 ± 1 |

Table 5.7 Diffusion coefficient values for each BA: MMA: AA colloid from batch DLS, AF4 theory ($D_{AF4}$), AF4 retention time ($D_{AF4\text{-}DLS}$), ThFFF retention time ($D_{ThFFF\text{-}DLS}$), and ThFFF online $R_g$ ($D_{ThFFF\text{-}Rg}$) in 0.1 mM TBAP and 0.05 % FL-70

| Sample (% AA) | $D_{DLS}$ (x$10^{-8}$ cm$^2$ s$^{-1}$) | $D_{AF4}$ (x$10^{-8}$ cm$^2$ s$^{-1}$) | $D_{AF4\text{-}DLS}$ (x$10^{-8}$ cm$^2$ s$^{-1}$) | $D_{ThFFF\text{-}DLS}$ (x$10^{-8}$ cm$^2$ s$^{-1}$) | $D_{ThFFF\text{-}Rg}$ (x$10^{-8}$ cm$^2$ s$^{-1}$) |
|---|---|---|---|---|---|
| 0 | 6.0 ± 0.2 | 5.8 ± 0.1 | 8.5 ± 0.1 | 7.0 ± 0.1 | 5.9 ± 0.2 |
| 0.5 | 6.5 ± 0.2 | 6.4 ± 0.2 | 8.9 ± 0.1 | 7.9 ± 0.1 | 6.3 ± 0.2 |
| 1 | 6.3 ± 0.2 | 6.3 ± 0.1 | 9.0 ± 0.1 | 7.7 ± 0.1 | 6.1 ± 0.2 |
| 2 | 6.2 ± 0.2 | 6.0 ± 0.1 | 8.9 ± 0.1 | 7.4 ± 0.1 | 6.0 ± 0.2 |
| 3 | 6.3 ± 0.2 | 6.1 ± 0.1 | 8.7 ± 0.1 | 7.3 ± 0.1 | 6.2 ± 0.2 |
| 1R | 4.6 ± 0.2 | 4.3 ± 0.2 | 7.7 ± 0.1 | 5.8 ± 0.1 | 5.1 ± 0.1 |

*$D_{calc}$, AF4 $D_{tr}$, ThFFF $D_{tr}$, and ThFFF $D_{Rg}$ values are determined at peak max from UV signal*

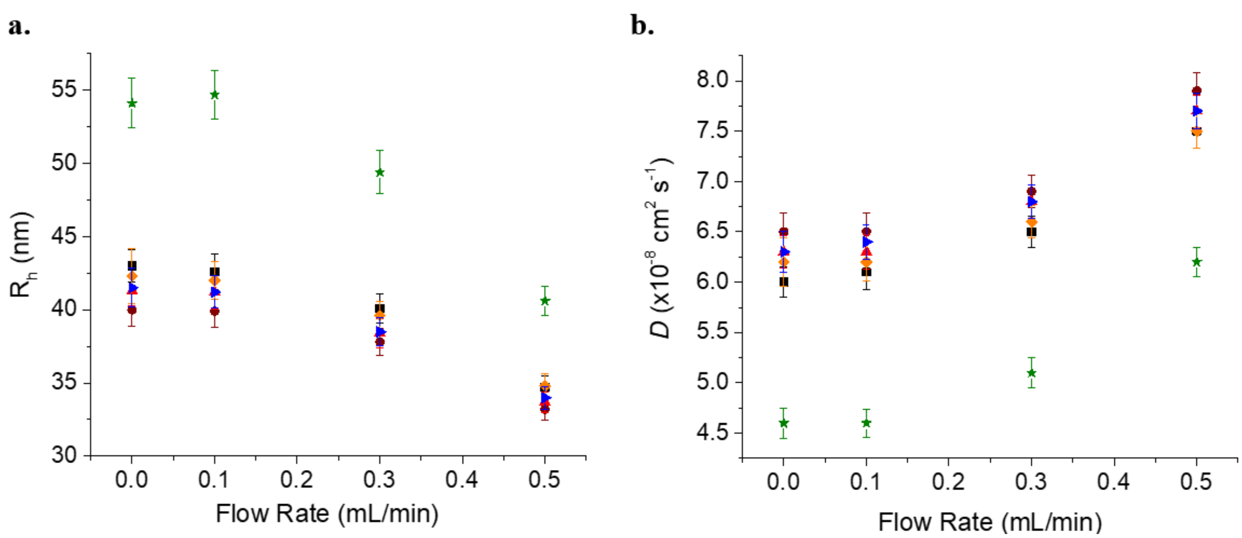


Figure 5.4 Influence of flow rate on (a) $R_h$ and (b) $D$ of BA: MMA: AA colloids in 0.1 mM TBAP and 0.05 % FL-70. Flow rates used in this study match the flow rates used in AF4 (0.5 mL/min) and AqThFFF (0.3 mL/min) experiments. Points correspond to colloids having 0 (black squares), 0.5 (maroon circles), 1 (red triangles), 2 (orange diamonds), 3 (blue right triangles), 1 redox (green stars) % AA in the synthesis monomer feed.

## 5.7 Acknowledgments

This material is based upon work primarily supported by the National Science Foundation (NSF) (CHE-401438, CLP and SKRW).

## 5.8 References


(1) Plavchak, C. L.; Smith, W. C.; Bria, C. R. M.; Williams, S. K. R. New Advances and Applications in Field-Flow Fractionation. *Annual Review of Analytical Chemistry* **2021**, *14*, 257–279. https://doi.org/https://doi.org/10.1146/annurev-anchem-091520- 052742.

(2) Schimpf, M. E.; Caldwell, Karin, D.; Giddings, J. C. *Field Flow Fractionation Handbook*, 1st ed.; John Wiley & Sons, Ltd: New York, NY, 2000.

(3) Smith, W. C.; Geisler, M.; Lederer, A.; Williams, S. K. R. Thermal Field-Flow Fractionation for Characterization of Architecture in Hyperbranched Aromatic-Aliphatic Polyesters with Controlled Branching. *Anal Chem* **2019**, *91* (19), 12344–12351. https://doi.org/10.1021/acs.analchem.9b02664.

(4) Geisler, M.; Plü, L.; Merna, J.; Lederer, A. The Role of Solubility in Thermal Field-Flow Fractionation: A Revisited Theoretical Approach for Tuning the Separation of Chain Walking Polymerized Polyethylene. **2020**. https://doi.org/10.1021/acs.analchem.0c03686.

(5) Liu, G.; Calvin Giddings, J. Separation of Particles in Nonaqueous Suspensions by Thermal-Electrical Field-Flow Fractionation. *Anal Chem* **1991**, *63* (3), 296–299. https://doi.org/10.1021/ac00003a021.

(6) Liu, G.; Calvin Giddings, J. Separation of Particles in Nonaqueous Suspensions by Thermal-Electrical Field-Flow Fractionation. *Anal Chem* **1991**, *63* (3), 296–299. https://doi.org/10.1021/ac00003a021.

(7) Shiundu, P. M.; Williams, P. S.; Giddings, J. C. Magnitude and Direction of Thermal Diffusion of Colloidal Particles Measured by Thermal Field-Flow Fractionation. *J Colloid Interface Sci* **2003**, *266* (2), 366–376. https://doi.org/10.1016/S0021-9797(03)00529-0.

(8) Jeon, S. J.; Schimpf, M. E.; Nyborg, A. Compositional Effects in the Retention of Colloids by Thermal Field-Flow Fractionation. *Anal Chem* **1997**, *69* (17), 3442–3450. https://doi.org/10.1021/ac9613040.

(9) Shiundu, P. M.; Calvin Giddings, J. Influence of Bulk and Surface Composition on the Retention of Colloidal Particles in Thermal Field-Flow Fractionation. *J Chromatogr A* **1995**. https://doi.org/10.1016/0021-9673(95)00572-5.

(10) Smith, W. C.; Morse, J. R.; Bria, C. R. M.; Schaak, R. E.; Williams, S. K. R. Composition-Based Separation of Pt-Fe3O4 Hybrid Nanoparticles by Thermal Field-Flow Fractionation. *ACS Appl Nano Mater* **2018**, *1* (11), 6435–6443. https://doi.org/10.1021/acsanm.8b01643.

(11) Mes, E. P. C.; Kok, W. T.; Tijssen, R. Sub-Micron Particle Analysis by Thermal Field-Flow Fractionation and Multi-Angle Light Scattering Detection. *Chromatographia* **2001**, *53* (11–12), 697–703. https://doi.org/10.1007/BF02493023.

(12) Kim Ratanathanawongs, S.; Shiundu, P. M.; Calvin Giddings, J. Size and Compositional Studies of Core-Shell Latexes Using Flow and Thermal Field-Flow Fractionation. *Colloids Surf A Physicochem Eng Asp* **1995**, *105* (2–3), 243–250. https://doi.org/10.1016/0927-7757(95)03315-7.

(13) Liu, G.; Giddings, J. C. Separation of Particles in Aqueous Suspensions by Thermal Field-Flow Fractionation. Measurement of Thermal Diffusion Coefficients. *Chromatographia* **1992**, *34* (9–10), 483–492. https://doi.org/10.1007/BF02290241.

(14) Pasti, L.; Agnolet, S.; Dondi, F. Thermal Field-Flow Fractionation of Charged Submicrometer Particles in Aqueous Media. *Anal Chem* **2007**, *79* (14), 5284–5296. https://doi.org/10.1021/ac070099t.

(15) Bringuier, E.; Bourdon, A. Colloid Transport in Nonuniform Temperature. *Phys Rev E Stat Phys Plasmas Fluids Relat Interdiscip Topics* **2003**, *67* (1), 6. https://doi.org/10.1103/PhysRevE.67.011404.

(16) Morozov, K. I. *Thermodi!Usion in Magnetic Colloids*; 1999; Vol. 201.

(17) Anderson, J. L. *Colloid Transport by Interfacial Forces*; 1989; Vol. 21. www.annualreviews.org.

(18) Giddings, J. C.; Shinudu, P. M.; Semenov, S. N. Thermophoresis of Metal Particles in a Liquid. *J Colloid Interface Sci* **1995**, *176* (2), 454–458. https://doi.org/10.1006/jcis.1995.9946.

(19) Duhr, S.; Braun, D. Thermophoretic Depletion Follows Boltzmann Distribution. *Phys Rev Lett* **2006**, *96* (16), 1–4. https://doi.org/10.1103/PhysRevLett.96.168301.

(20) Duhr, S.; Braun, D. Why Molecules Move along a Temperature Gradient. *Proceedings of the National Academy of Sciences* **2006**, *103* (52), 19678–19682. https://doi.org/10.1073/pnas.0603873103.

(21) Piazza, R.; Parola, A. Thermophoresis in Colloidal Suspensions. *Journal of Physics Condensed Matter* **2008**, *20* (15). https://doi.org/10.1088/0953-8984/20/15/153102.

(22) Mes, E. P. C.; Tijssen, R.; Kok, W. T. Influence of the Carrier Composition on Thermal Field-Flow Fractionation for the Characterisation of Sub-Micron Polystyrene Latex Particles. *J Chromatogr A* **2001**, *907* (1–2), 201–209. https://doi.org/10.1016/S0021-9673(00)01010-4.

(23) Lang, T.; Eslahian, K. A.; Maskos, M. Ion Effects in Field-Flow Fractionation of Aqueous Colloidal Polystyrene. *Macromol Chem Phys* **2012**, *213* (22), 2353–2361. https://doi.org/10.1002/macp.201200132.

(24) Eslahian, K. A.; Majee, A.; Maskos, M.; Würger, A. Specific Salt Effects on Thermophoresis of Charged Colloids. *Soft Matter* **2014**, *10* (12), 1931–1936. https://doi.org/10.1039/c3sm52779d.

(25) Eslahian, K. A.; Maskos, M. Hofmeister Effect in Thermal Field-Flow Fractionation of Colloidal Aqueous Dispersions. *Colloids Surf A Physicochem Eng Asp* **2012**, *413*, 65–70. https://doi.org/10.1016/j.colsurfa.2012.02.003.

(26) Shiundu, P. M.; Munguti, S. M.; Williams, S. K. R. Practical Implications of Ionic Strength Effects on Particle Retention in Thermal Field-Flow Fractionation. *J Chromatogr A* **2003**, *984* (1), 67–79. https://doi.org/10.1016/S0021-9673(02)01769-7.

(27) Litzén, A.; Wahlund, K. G. Effects of Temperature, Carrier Composition and Sample Load in Asymmetrical Flow Field-Flow Fractionation. *J Chromatogr A* **1991**. https://doi.org/10.1016/S0021-9673(01)88622-2.

(28) Shiundu, P. M.; Liu, G.; Calvin Giddings, J. Separation of Particles in Nonaqueous Suspensions by Thermal Field-Flow Fractionation. *Anal Chem* **1995**, *67* (15), 2705–2713. https://doi.org/10.1021/ac00111a032.

(29) Mes, E. P. C.; Tijssen, R.; Kok, W. T. Influence of the Carrier Composition on Thermal Field-Flow Fractionation for the Characterisation of Sub-Micron Polystyrene Latex Particles. *J Chromatogr A* **2001**. https://doi.org/10.1016/S0021-9673(00)01010-4.

(30) Sitar, S.; Vezoč, V.; Mač, P.; Kogej, K.; Pahovnik, D.; Agar, E. Z. ˇ. Pitfalls in Size Characterization of Soft Particles by Dynamic Light Scattering Online Coupled to Asymmetrical Flow Field-Flow Fractionation. *Anal. Chem* **2017**, *89*, 38. https://doi.org/10.1021/acs.analchem.7b03251.

(31) Kassalainen, G. E.; Williams, S. K. R. Lowering the Molecular Mass Limit of Thermal Field-Flow Fractionation for Polymer Separations. *J Chromatogr A* **2003**. https://doi.org/10.1016/S0021-9673(02)02061-7.

# CHAPTER 6

# CONCLUSIONS AND FUTURE DIRECTIONS

The work contained within this dissertation showcases several developments in both field-flow fractionation and light scattering methodologies for the characterization of biological and polymer colloids. Asymmetrical flow and thermal FFF along with MALS will continue to play a role in nanoparticle characterization and particle enumeration with MALS provides opportunities to be used as a complementary method to other readily used particle counting techniques like NTA.

## 6.1 Conclusions

Over the past decade, advances in the instrumentation and utilization of asymmetrical flow and thermal FFF for particle characterization has continued to push this community towards understanding more dynamic properties of materials beyond performing a separation alone. Modifications in membrane texture and composition to the coupling of instrumentation such as Raman spectrometers to AF4 as seen in Chapter 3 continues to improve separations and address the need for advanced characterization of materials like nanoplastics. Other engineered and naturally occurring nanoparticles that have been characterized through ThFFF have led to a focus on understanding the role of additives in carrier fluid and revisiting the potential advantages of aqueous ThFFF.

Chapter 4 encompassed both advancements in AF4-MALS methodology and assessment of MALS as a particle counting technique for complex, bacterial outer membrane vesicles. While roughly ten publications have utilized MALS as a particle counting technique in conjunction with other methods like NTA, this work pointed out the nuances of analyte-dependent parameters and their influence on overall particle counts. For standard particles like polystyrene latex, the larger refractive index value of 1.58 showed deviations between spherical models. For more complex outer membrane vesicles, estimated RI values and a coated sphere model showed that core RI values can dictate the magnitude of particle counts and signal to noise can lead to erroneous counts. While still in its adolescent stages, MALS has the potential to be a robust particle counting method. In addition to the fundamental work in Chapter 4, preliminary results showcased the advantages of separation and enumeration of vesicles prior to proteomics analysis. The initial separation step led to uncovering potential differences in protein cargo sorting between vesicle sizes. To date, this was first account of utilizing AF4-MALS prior to biochemical analyses for Gram-negative bacterial outer membrane vesicles. Further proteomic and lipidomic analysis could also serve as a good way to better understand vesicle protein to lipid ratios and in turn, giving rise to more representative RI values for MALS particle counting.

The dormancy of aqueous ThFFF has led to several questions relating to why retention is achieved with the use of additives along with the compositional sensitivity of the technique. In Chapter 5, it was determined that AqThFFF is sensitive enough to distinguish between subtle differences in acidic comonomer (< 1 %) compared to previously reported literature (< 9 %). While this sensitivity was observed, the carrier fluid composition continues to dictate the degree of retention and thus particle thermal diffusion. Because of this, compositional sensitivity in ThFFF may be different based on the analyte system and carrier fluid composition. While a mechanism for why additives cause these retention trends and influence sample recovery are still unknown, this work has reopened the field of AqThFFF to characterize aqueous-based suspensions.

## 6.2 Future Directions

As MALS particle counting continues to gain traction, it is of importance truly understand the robustness of this technique for both simple and complex nanoparticles. The use of calibration curves can continue to serve as a way to validate particle counts however the lack of absolute particle count standards (< 1 μm in diameter) ultimately provides a relative, not absolute, particle count. In conjunction with advancing particle count standards, it is paramount to address unknown refractive indices of complex biological particles. While efforts have been made to utilize light scattering data to obtain a refractive index for mammalian cells, there is still need for a robust yet simple method to experimentally determine RI values of biological samples. The use of proteomic and lipidomic data can help infer ratios of these vesicle components yet can be a time and cost-intensive process. The use of MALS particle counting, while a useful tool to have in the light scattering arsenal, still needs a critical eye and true understanding of the light scattering theories that are behind the application.

As the realm of AqThFFF is revisited, the use of additives (e.g. salts and surfactants) within sample and the carrier fluid preparation provides handles on understanding particle retention and insight into particle thermophoresis theories. The use of these additives and their influence on retention has always been of focus, yet little is known how these additives impact sample recovery. There is more work that needs to be done in this area, yet the work highlighted in this dissertation hints at potential opportunities to relate sample recovery and retention to composition. Exploration of different anions and cations of the Hofmeister series of salts could build a better database for understanding what cations and/or anions dictate AqThFFF retention and $D_T$. While particle and polymer thermophoresis are still poorly understood, future work could better uncover whether or not particle thermal diffusion is truly independent on size;

something that is well established with polymer thermophoresis. Other orthogonal methods like capillary electrophoresis or Microscale thermophoresis may serve as a way to compare thermal diffusion values obtained by AqThFFF and better understand these potential additive effects.

APPENDIX A

# APPLICATION OF ASYMMETRICAL FLOW FIELD-FLOW FRACTIONATION FOR THE CHARACTERIZATION OF *MYCOBACTERIUM TUBERCULOSIS* EXTRACELLULAR VESICLES

Christine L. Plavchak[1], Joan M. Ryan[2], Nicole Kruh-Garcia[2], and S. Kim Ratanathanawongs Williams[1]

## A.1 Overview

Tuberculosis is the second-leading infectious killer behind COVID-19 and is caused by *Mycobacterium tuberculosis (Mtb).* Like other eukaryotic cells and Gram-negative bacteria, Gram-positive and mycobacterial species produce extracellular vesicles (EVs) yet the biogenesis of these EVs remains elusive.[1,2] A continuing challenge in this field is defining functional characteristics of EV populations mainly due to the lack of specific markers for different EV subtypes. Separation and enrichment techniques have been employed to gain insight into potential functional differences in subpopulations; however, bias towards or against certain EV subsets make understanding the compositional heterogeneity of EVs across the field challenging.[1,3]

Current mycobacterial EV separation and enrichment methods consist of ultracentrifugation, [4–6] density gradient ultracentrifugation,[7–11] and size exclusion chromatography (SEC).[10,12–14] Ultracentrifugation (UC) and density gradient ultracentrifugation are widely used methods and are relatively inexpensive yet tend to have low separation efficiency (ultracentrifugation), low yield, and can induce vesicle aggregation or potential EV

[1] Laboratory for Advanced Separations Technologies, Department of Chemistry, Colorado School of Mines, Golden, Colorado, 80401, USA
[2] Department of Microbiology, Immunology, and Pathology, Colorado State University, Fort Collins, Colorado, 80523, USA

lysis. Another disadvantage is that many of the published works using these techniques lack details about the experimental conditions (rotors, centrifuge information, etc) and enrichment/separation is often instrument dependent. SEC is considered to be a gentler separation technique that preserves EV integrity while still having high separation efficiency. Despite these advantages, SEC tends to be more expensive with reagent or consumable cost, samples become diluted, and there can be overlap with EV markers and contaminants making fraction collection more challenging.

Recent work performed by collaborators showed across these three different methods, results from SEC show better reproducibility compared to centrifugation-based methods.[15] Density gradient ultracentrifugation and SEC of *Mtb* EVs showed the lowest amount of contaminant proteins compared to UC. While the purity is higher for those methods, traditional UC methods demonstrated a higher vesicle recovery but with low purity. Across all three methods studied by collaborators, SEC methods provide the highest vesicle recovery and highest purity which can be important for further biochemical analyses. One major analytical challenge that hasn't been addressed how to reliably separate free from vesicle-bound *Mtb* proteins.

Asymmetrical flow field flow fractionation (AF4) is a size-based separation technique that has been used to separate extracellular vesicles from mammalian cell lines along with Gram-negative bacteria shown in Chapter 4.[16–20] AF4 is often considered a 'gentle' separation technique because it lacks the packing material or stationary phase that is found within an SEC column. A focusing or concentration step at the beginning of an AF4 experiment can act as a purification step where small contaminants can pass through the semipermeable membrane. Additionally, this focusing step may also help separate free protein from those associated with EVs.

This work aims to further understand the protein heterogeneity of *Mtb* EVs through an initial size-based separation using AF4. Fractionating EVs prior to proteomic analysis provides a clearer outlook on the composition of both free and vesicle-bound proteins. During the AF4 separation, five different fractions associated with the anticipated EV size ranges were collected for offline characterization. TEM analysis of all fractions showed F1 containing predominantly free protein while F2-F5 were mainly EVs. Further biochemical analyses of the collected fractions hint at smaller EVs being more immunogenic, and the use of AF4 provides a highly resolved understanding of protein enrichment in *Mtb* EVs compared to other separation techniques like SEC.

## A.2 Results and Discussion

### A.2.1 Size-based Separation and Analysis of *Mtb* EVs through AF4-MALS

Three biological replicates of *Mtb* EVs were separated via AF4. For offline analysis, five pre-determined fractions were collected and six consecutive AF4 injections were made in to obtain sufficient concentration of EVs. Figure A.1 shows the averaged MALS signals of each biological replicate along with the corresponding fractions that were collected (F1-F5). The similar retention times across the biological replicates show similar populations across different cultivations. Replicate 1 (black trace) has a larger MALS signal intensity which could be related to the quantity of vesicle populations. During the sample preparation stage, replicate 1 came from a 16-liter culture of *Mtb* while replicates 2 and 3 came from 8 liters of culture. The impacts of culture size on protein content or number of vesicles have not been well studied, however the total protein content for all replicates were initially the same (0.93 mg/mL) prior to AF4 separation.

The fractograms in Figure A.1 were signal averaged based on the six consecutive AF4 injections. The reproducibility of those injections can be seen in Figure A.2. Little change in the MALS and UV traces show similar populations across all replicates and larger UV responses between 2 and 11 minutes correspond to a higher concentration of proteins which was later verified through a bicinchoninic acid (BCA) protein assay for total protein content and TEM.

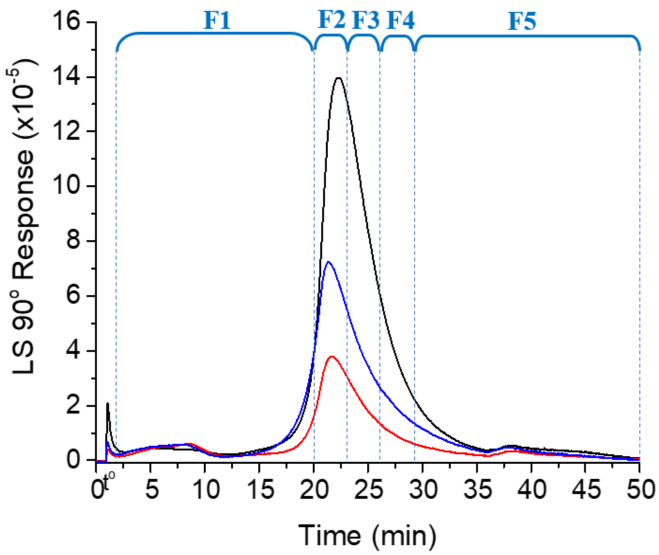


Figure A.1 AF4-MALS fractograms of three different biological replicates of *Mtb* EVs. The black, red, and blue traces correspond to replicate 1, 2, and 3 respectively. Fractions 1-5 (F1-F5) were collected for further analyses.

To correlate vesicle size to offline proteomic analyses, the radius of gyration distributions of each replicate was also determined and then transformed into hydrodynamic radius ($R_h$) assuming a hard sphere ($R_g/R_h = 0.78$). These distributions are consistent across all three replicates (Figure A.3). Due to the low MALS signal in F1, $R_h$ data could not be determined. Additionally, the change in Rh distributions around 32 minutes is mainly a result of the AF4 field turning completely off. The increase in $R_h$ could be due to larger vesicles that were still being retained within the channel, aggregates, or remnants of other adsorbed material left on the membrane surface.[21] The fractions were further analyzed offline via TEM and NTA and similar sizes were determined for F2-F5 across all three techniques.

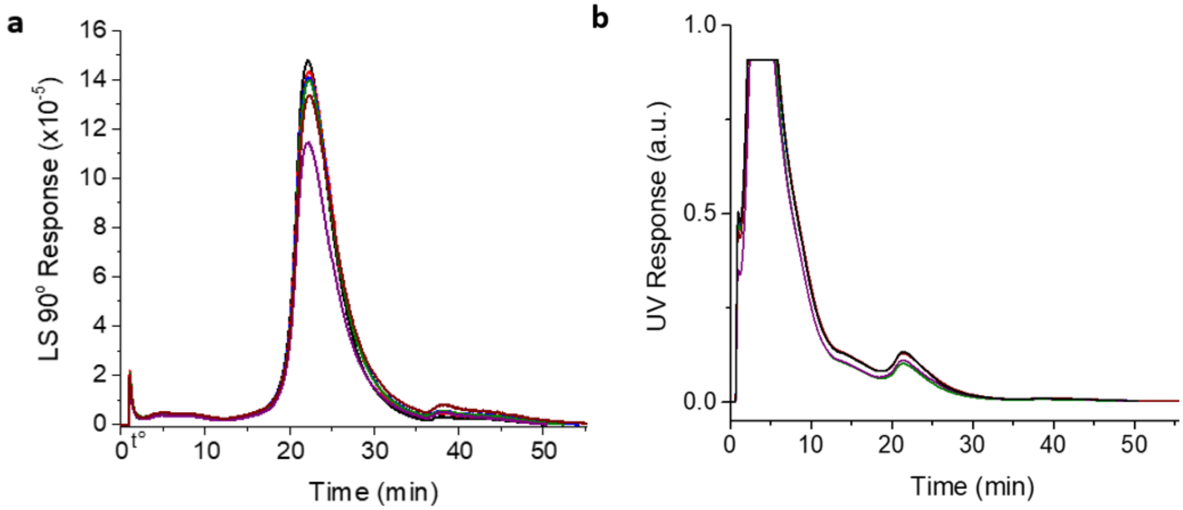


Figure A.2 AF4 (a) MALS and (b) UV fractograms showing six AF4 replicates of Mtb EVs in Sample 1

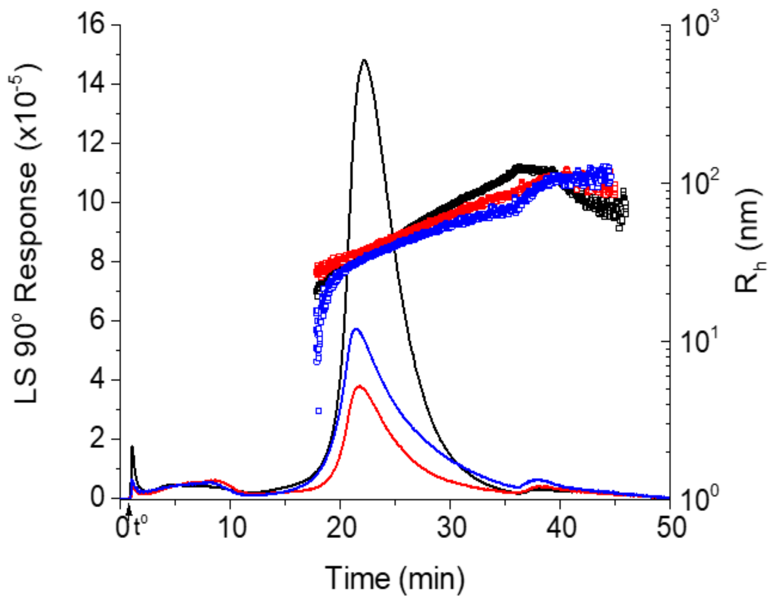


Figure A.3 MALS fractogram of three different biological replicates of *Mtb* EVs and their corresponding $R_h$ distributions

### A.2.2 Post-Fractionation Multi-Technique Analysis on *Mtb* EV Fractions

In addition to the TEM and NTA, collected fractions were further analyzed by SDS-PAGE, silver stain, Western blot, and shotgun proteomics via LC-MS/MS. These analyses were completed by collaborators at Colorado State University, Drs. Nicole Kruh-Garcia and Joan M. Ryan. Across the different fractions, the proteomics and Western blot data show that smaller *Mtb* EVs contain more acylated or glycosylated proteins which are involved in host-protein interactions like toll-like receptor 2 (TLR-2). Additionally, it appeared that the amount of lipoarabinomannan (LAM), a virulence factor of *Mtb*, decreased across the fractions. The acylated or glycosylated proteins along with the increased concentration of LAM for the smaller particles suggest smaller *Mtb* EVs could be more immunogenic than larger EVs. A more detailed report of the SDS-PAGE, Western blot, silver stain, and LC-MS/MS analysis can be found in Chapter 3 of Dr. Ryan's thesis.

## A.3 Conclusion

This work was the first account of utilizing AF4 to separate *Mtb* EVs. While another application of AF4, it showcases AF4's to potential impact in the realm of Gram-positive and mycobacterium characterization. This initial work provided insight to what proteins may or may not be enriched into *Mtb* EVs and provides a new avenue in comparing biases across different separation techniques in the *Mtb* community. Further understanding of the biogenesis and distinction of *Mtb* EV subtypes could push EVs towards becoming a biomarker to diagnose TB via accessible biofluids like blood.

## A.4 Experimental

### A.4.1 Preparation of *Mtb* Extracellular Vesicles

The preparation of the *Mtb* EV samples was conducted in collaboration with Nicole Kruh-Garcia's laboratory at Colorado State University. Specific methodological details are described in Joan M. Ryan's thesis and will be described in a future publication.

### A.4.2 Asymmetrical flow field-flow fractionation and on-line detection with ultraviolet (UV) and multi-angle light scattering-dynamic light scattering (MALS-DLS)

Fractionation of *MTb* EVs was performed using an AF2000 system (Postnova Analytics, Salt Lake City, Utah) coupled to multiple detectors that included UV/Vis (SPD-20A Shimadzu, Japan), and MALS-DLS (DAWN HELEOS II, Wyatt Technology Corporation, Santa Barbara, California). UV data was collected at 280 nm and MALS-DLS data was acquired and analyzed using Astra 7.3.2.21 (Wyatt Technology Corporation, Santa Barbara, California). The MALS detector was normalized using bovine serum albumin (BSA) (Sigma-Aldrich, St. Louis, Missouri). For examining size distributions, MALS $R_g$ values were transformed into $R_h$ values assuming a spherical shape ($R_g/R_h$ = 0.77). The AF4 trapezoidal channel has a nominal thickness of 350 µm consisting of a tip-to-outlet length of 27.5 cm, breadth at channel inlet of 2 cm, and breadth at channel outlet of 0.5 cm. The semi-permeable accumulation wall was a regenerated cellulose membrane with a 10 kDa molecular weight cutoff (Postnova Analytics, Salt Lake City, Utah). A 0.1 µm inline filter (Merck Millipore Ltd, Ireland) was positioned between the HPLC pump and the AF4 channel.

A mixture of 20, 100, 200 and 500 nm Duke polystyrene latex particles (Thermo Fisher Scientific, Waltham, Massachusetts) was used to demonstrate the AF4 separation. The mixture was suspended in 0.02% sodium azide (Sigma-Aldrich, St. Louis, Missouri) and 0.05 % FL-70 surfactant (Thermo Fisher Scientific, Waltham, Massachusetts) in deionized 18.2 MΩ water which was also used as the AF4 carrier fluid. The sample injection volume was 1 mL, the sample injection flow rate was 0.2 mL/min, and the detector flow rate was 0.5 mL/min. The crossflow rate was1.0 mL/min during the 15-minute sample loading and focusing period the sample for 15 minutes. After focusing, the crossflow was held at 1.0 mL/min for an additional 12 minutes, decreased linearly to 0.1 mL/min over 8 minutes, held at 0.1 mL/min for 25 minutes and then turned off.

AF4 separation of all *MTb* EV samples was done in the same manner to that for the latex particles except for the last step where the crossflow rate was held at 0.1 mL/min for 15 minutes and then turned off. The carrier fluid used for EV separation was 1x phosphate buffered saline (PBS) which was diluted from 10x PBS (molecular biology grade, Mediatech, Inc., Manassas, Virginia) using 18.2 MΩ water. Five fractions (F1-F5) were collected for each sample and stored at 4 °C until needed. To ensure enough sample was present for offline analyses, six AF4 injections were made to obtain a higher concentration of EVs in each fraction.

### A.4.3 AF4 Fraction Analysis of *Mtb* EVs

After fractionating *MTb* EVs, collected fractions were then concentrated and assessed by nanoparticle tracking analysis (NTA) for concentration and sizes distribution and transmission electron microscopy for size confirmation. Sodium dodecyl sulfate polyacrylamide gel electrophoresis (SDS-PAGE) along with silver stain, Western blot, and shotgun proteomics via liquid chromatography tandem mass spectrometry (LC-MS/MS) were used for quantitative and qualitative protein analyses. Samples were prepared for LC-MS/MS by performing a trypsin digest and then identifying proteins through several databases. Similar to section A.4.1, experimental details are provided in Joan M. Ryan’s thesis and were completed at Colorado State University.

### A.5 References


(1) Mehaffy, C.; Ryan, J. M.; Kruh-garcia, N. A.; Dobos, K. M. Extracellular Vesicles in Mycobacteria and Tuberculosis. *Front Cell Infect Microbiol* **2022**, *12* (May), 1–12. https://doi.org/10.3389/fcimb.2022.912831.

(2) Chiplunkar, S. S.; Silva, C. A.; Bermudez, L. E.; Danelishvili, L. Characterization of Membrane Vesicles Released by Mycobacterium Avium in Response to Environment Mimicking the Macrophage Phagosome. *Future Microbiol* **2019**, *14*, 293–313.

(3) Liangsupree, T.; Multia, E.; Riekkola, M. L. Modern Isolation and Separation Techniques for Extracellular Vesicles. *J Chromatogr A* **2021**, *1636*, 461771–461788. https://doi.org/10.1016/j.chroma.2020.461773.

(4) Marsollier, L.; Brodin, P.; Jackson, M.; Korduláková, J.; Tafelmeyer, P.; Carbonnelle, E.; Aubry, J.; Milon, G.; Legras, P.; Saint André, J. P.; Leroy, C.; Cottin, J.; Guillou, M. L. J.; Reysset, G.; Cole, S. T. Impact of Mycobacterium Ulcerans Biofilm on Transmissibility to Ecological Niches and Buruli Ulcer Pathogenesis. *PLoS Pathog* **2007**, *3* (5), 0582–0594. https://doi.org/10.1371/journal.ppat.0030062.

(5) Ziegenbalg, A.; Prados-Rosales, R.; Jenny-Avital, E. R.; Kim, R. S.; Casadevall, A.; Achkar, J. M. Immunogenicity of Mycobacterial Vesicles in Humans: Identification of a New Tuberculosis Antibody Biomarker. *Tuberculosis* **2013**, *93*, 448–455. https://doi.org/10.1016/j.tube.2013.03.001.

(6) Kumar, S.; Mittal, E.; Deore, S.; Kumar, A.; Rahman, A.; Krishnasastry, M. V. Mycobacterial TlyA Gene Product Is Localized to the Cell-Wall without Signal Sequence. *Front Cell Infect Microbiol* **2015**, *5*. https://doi.org/10.3389/fcimb.2015.00060.

(7) Prados-Rosales, R.; Baena, A.; Martinez, L. R.; Luque-Garcia, J.; Kalscheuer, R.; Veeraraghavan, U.; Camara, C.; Nosanchuk, J. D.; Besra, G. S.; Chen, B.; Jimenez, J.; Glatman-Freedman, A.; Jacobs, W. R.; Porcelli, S. A.; Casadevall, A. Mycobacteria Release Active Membrane Vesicles That Modulate Immune Responses in a TLR2-Dependent Manner in Mice. *Journal of Clinical Investigation* **2011**, *121* (4), 1471–1483. https://doi.org/10.1172/JCI44261.

(8) Prados-Rosales, R.; Brown, L.; Casadevall, A.; Montalvo-Quirós, S.; Luque-Garcia, J. L. Isolation and Identification of Membrane Vesicle-Associated Proteins in Gram-Positive Bacteria and Mycobacteria. *MethodsX* **2014**, *1*, 124–129. https://doi.org/10.1016/j.mex.2014.08.001.

(9) Lee, J.; Kim, S. H.; Choi, D. S.; Lee, J. S.; Kim, D. K.; Go, G.; Park, S. M.; Kim, S. H.; Shin, J. H.; Chang, C. L.; Gho, Y. S. Proteomic Analysis of Extracellular Vesicles Derived from Mycobacterium Tuberculosis. *Proteomics* **2015**, *15*, 3331–3337. https://doi.org/10.1002/pmic.201500037.

(10) Athman, J. J.; Wang, Y.; McDonald, D. J.; Boom, W. H.; Harding, C. V.; Wearsch, P. A. Bacterial Membrane Vesicles Mediate the Release of Mycobacterium Tuberculosis Lipoglycans and Lipoproteins from Infected Macrophages. *The Journal of Immunology* **2015**, *195* (3), 1044–1053. https://doi.org/10.4049/jimmunol.1402894.

(11) Dauros Singorenko, P.; Chang, V.; Whitcombe, A.; Simonov, D.; Hong, J.; Phillips, A.; Swift, S.; Blenkiron, C. Isolation of Membrane Vesicles from Prokaryotes: A Technical and Biological Comparison Reveals Heterogeneity. *J Extracell Vesicles* **2017**, *6*, 1324731–1324746. https://doi.org/10.1080/20013078.2017.1324731.

(12) Athman, J. J.; Sande, O. J.; Groft, S. G.; Reba, S. M.; Nagy, N.; Wearsch, P. A.; Richardson, E. T.; Rojas, R.; Boom, W. H.; Shukla, S.; Harding, C. V. Mycobacterium Tuberculosis Membrane Vesicles Inhibit T Cell Activation. *The Journal of Immunology* **2017**, *198* (5), 2028–2037. https://doi.org/10.4049/jimmunol.1601199.

(13) Jurkoshek, K. S.; Wang, Y.; Athman, J. J.; Barton, M. R.; Wearsch, P. A. Interspecies Communication between Pathogens and Immune Cells via Bacterial Membrane Vesicles. *Front Cell Dev Biol* **2016**, *4*. https://doi.org/10.3389/fcell.2016.00125.

(14) Lucas, M.; Ryan, J. M.; Watkins, J.; Early, K.; Kruh-Garcia, N. A.; Mehaffy, C.; Dobos, K. M. Extraction and Separation of Mycobacterial Proteins. In *Mycobacteria Protocols*; Parish, T., Kumar, A., Eds.; 2021.

(15) Ryan, J. M. ENRICHMENT AND SEPARATION OF MYCOBACTERIUM TUBERCULOSIS EXTRACELLULAR VESICLES WITH A SIDE OF BIOSAFETY AND BIOSECURITY, Colorado State University, Fort Collins, 2022.

(16) Zhang, H.; Lyden, D. Asymmetric-Flow Field-Flow Fractionation Technology for Exomere and Small Extracellular Vesicle Separation and Characterization. *Nat Protoc* **2019**, *14* (4), 1027–1053. https://doi.org/10.1038/s41596-019-0126-x.

(17) Zhang, H.; Freitas, D.; Kim, H. S.; Fabijanic, K.; Li, Z.; Chen, H.; Mark, M. T.; Molina, H.; Martin, A. B.; Bojmar, L.; Fang, J.; Rampersaud, S.; Hoshino, A.; Matei, I.; Kenific, C. M.; Nakajima, M.; Mutvei, A. P.; Sansone, P.; Buehring, W.; Wang, H.; Jimenez, J. P.; Cohen-Gould, L.; Paknejad, N.; Brendel, M.; Manova-Todorova, K.; Magalhães, A.; Ferreira, J. A.; Osório, H.; Silva, A. M.; Massey, A.; Cubillos-Ruiz, J. R.; Galletti, G.; Giannakakou, P.; Cuervo, A. M.; Blenis, J.; Schwartz, R.; Brady, M. S.; Peinado, H.; Bromberg, J.; Matsui, H.; Reis, C. A.; Lyden, D. Identification of Distinct Nanoparticles and Subsets of Extracellular Vesicles by Asymmetric Flow Field-Flow Fractionation. *Nat Cell Biol* **2018**, *20* (3), 332–343. https://doi.org/10.1038/s41556-018-0040-4.

(18) Sitar, S.; Kejž, A.; Pahovnik, D.; Kogej, K.; Tušek-Znidarič, M.; Lenassi, M.; Zagar, E. Size Characterization and Quantification of Exosomes by Asymmetrical-Flow Field-Flow Fractionation. *Anal Chem* **2015**, *87*, 9225–9233. https://doi.org/10.1021/acs.analchem.5b01636.

(19) Kang, D.; Oh, S.; Ahn, S.-M.; Lee, B.-H.; Moon, M. H. Proteomic Analysis of Exosomes from Human Neural Stem Cells by Flow Field-Flow Fractionation and Nanoflow Liquid Chromatography-Tandem Mass Spectrometry. https://doi.org/10.1021/pr800225z.

(20) Yang, J. S.; Lee, J. C.; Byeon, S. K.; Ho Rha, K.; Moon, M. H. Size Dependent Lipidomic Analysis of Urinary Exosomes from Patients with Prostate Cancer by Flow Field-Flow Fractionation and Nanoflow Liquid Chromatography-Tandem Mass Spectrometry. **2017**. https://doi.org/10.1021/acs.analchem.6b04634.

(21) Gregory, C.; Marcondes, M. C. G.; Hall, B. M.; Estrada-garcía, I. Extracellular Vesicles Released from Mycobacterium Tuberculosis-Infected Neutrophils Promote Macrophage Autophagy and Decrease Intracellular Mycobacterial Survival. **2018**, *9* (February), 1–12. https://doi.org/10.3389/fimmu.2018.00272.

APPENDIX B

COPYRIGHT PERMISSIONS

## B.1 Copyright Permissions for Chapter 2

**Effects of temperature, carrier composition and sample load in asymmetrical flow field-flow fractionation**

**Author:** Anne Litzén,Karl-Gustav Wahlund
**Publication:** Journal of Chromatography A
**Publisher:** Elsevier
**Date:** 12 July 1991



**Order Completed**

Thank you for your order.

This Agreement between Colorado School of Mines -- Christine Plavchak ("You") and Elsevier ("Elsevier") consists of your license details and the terms and conditions provided by Elsevier and Copyright Clearance Center.

Your confirmation email will contain your order number for future reference.

| | |
|---|---|
| **License Number** | 5523171216148 |
| **License date** | Apr 06, 2023 |

Printable Details

**Licensed Content**

| | |
|---|---|
| **Licensed Content Publisher** | Elsevier |
| **Licensed Content Publication** | Journal of Chromatography A |
| **Licensed Content Title** | Effects of temperature, carrier composition and sample load in asymmetrical flow field-flow fractionation |
| **Licensed Content Author** | Anne Litzén,Karl-Gustav Wahlund |
| **Licensed Content Date** | Jul 12, 1991 |
| **Licensed Content Volume** | 548 |
| **Licensed Content Issue** | n/a |
| **Licensed Content Pages** | 14 |

**Order Details**

| | |
|---|---|
| **Type of Use** | reuse in a thesis/dissertation |
| **Portion** | figures/tables/illustrations |
| **Number of figures/tables/illustrations** | 2 |
| **Format** | print |
| **Are you the author of this Elsevier article?** | No |
| **Will you be translating?** | No |

**About Your Work**

| | |
|---|---|
| **Title** | ASSESSING FIELD-FLOW FRACTIONTION AND LIGHT SCATTERING FOR THE CHARACTERIZATION OF EXTRACELLULAR VESICLES AND POLYMER COLLOIDS |
| **Institution name** | Colorado School of Mines |
| **Expected presentation date** | Apr 2023 |

**Additional Data**

| | |
|---|---|
| **Portions** | Fig. 1 and 2 |

**Requestor Location**

| | |
|---|---|
| **Requestor Location** | Colorado School of Mines<br>1500 Illinois Street<br><br>Golden, CO 80401<br>United States |

**Tax Details**

| | |
|---|---|
| **Publisher Tax ID** | 98-0397604 |

## B.2 Copyright Permissions for Chapter 3

**CCC | Marketplace**



| | | | |
|---|---|---|---|
| **Order Date** | 07-Mar-2023 | **Type of Use** | Republish in a thesis/dissertation |
| **Order License ID** | 1331490-1 | **Publisher** | Annual Reviews |
| **ISSN** | 1936-1335 | **Portion** | Chapter/article |

### LICENSED CONTENT

| | | | |
|---|---|---|---|
| **Publication Title** | Annual review of analytical chemistry | **Rightsholder** | Annual Reviews, Inc. |
| **Date** | 01/01/2008 | **Publication Type** | e-Journal |
| **Language** | English | **URL** | http://arjournals.annualreviews.org/loi/a... |
| **Country** | United States of America | | |

### REQUEST DETAILS

| | | | |
|---|---|---|---|
| **Portion Type** | Chapter/article | **Rights Requested** | Main product |
| **Page Range(s)** | 257-279 | **Distribution** | Worldwide |
| **Total Number of Pages** | 22 | **Translation** | Original language of publication |
| **Format (select all that apply)** | Electronic | **Copies for the Disabled?** | No |
| **Who Will Republish the Content?** | Academic institution | **Minor Editing Privileges?** | Yes |
| **Duration of Use** | Life of current edition | **Incidental Promotional Use?** | No |
| **Lifetime Unit Quantity** | Up to 499 | **Currency** | USD |

### NEW WORK DETAILS

| | | | |
|---|---|---|---|
| **Title** | Assessing Field-Flow Fractionation and Light Scattering for the Characterization of Extracellular Vesicles and Polymer Colloids | **Institution Name** | Colorado School of Mines |
| | | **Expected Presentation Date** | 2023-04-25 |
| **Instructor Name** | Christine L. Plavchak | | |

### ADDITIONAL DETAILS

| | | | |
|---|---|---|---|
| **Order Reference Number** | N/A | **The Requesting Person/Organization to Appear on the License** | Christine L. Plavchak |

### REQUESTED CONTENT DETAILS

| | | | |
|---|---|---|---|
| **Title, Description or Numeric Reference of the Portion(s)** | New Advances and Applications in Field-Flow Fractionation | **Title of the Article/Chapter the Portion Is From** | n/a |
| **Editor of Portion(s)** | Laura Niven | **Author of Portion(s)** | Christine Plavchak, William Smith, Carmen Bria, and S. Kim Ratanathanawongs |

[External] Re: Copyright and Co-Author Permissions for "New Advances and Applications in Field-Flow Frac...

William C Smith <williamconnersmith@gmail.cc
To Christine Plavchak
Cc crmbria@gmail.com; Kim Williams

Reply Reply All Forward

Tue 3/7/2023 7:16 PM

Follow up. Start by Tuesday, March 7, 2023. Due by Tuesday, March 7, 2023.
You replied to this message on 3/7/2023 7:23 PM.
If there are problems with how this message is displayed, click here to view it in a web browser.



Hi Christine!

Hope everything is going well!

I, *William C. Smith*, authorize Christine L. Plavchak to use any part or all of the manuscript entitled "New Advances and Applications in Field-Flow Fractionation" (https://doi.org/10.1146/annurev-anchem-091520-052742) in her thesis.

All the best,

Billy

[External] Re: Copyright and Co-Author Permissions for "New Advances and Applications in Field-Flow Frac...

Carmen Bria <crmbria@gmail.com>
To Christine Plavchak

Reply Reply All Forward

Tue 3/7/2023 5:14 PM

If there are problems with how this message is displayed, click here to view it in a web browser.

Start your reply all with: Received, thank you. Thank you! Got it, thanks! Feedback



Boom:

I, *Carmen Bria*, authorize Christine L. Plavchak to use any part or all of the manuscript entitled "New Advances and Applications in Field-Flow Fractionation" (https://doi.org/10.1146/annurev-anchem-091520-052742) in her thesis.

RE: Copyright and Co-Author Permissions for "New Advances and Applications in Field-Flow Fractionation"

Kim Williams
To Christine Plavchak

Reply Reply All Forward

Tue 3/7/2023 5:56 PM

Start your reply all with: Thank you! Great, thank you so much! Received, thank you. Feedback

Hi Christine,

I, Kim Williams, authorize Christine L. Plavchak to use any part or all of the manuscript entitled "New Advances and Applications in Field-Flow Fractionation" (https://doi.org/10.1146/annurev-anchem-091520-052742) in her thesis.

Kim